Master's thesis

NTNU
Norwegian University of Science and Technology
Faculty of Information Technology and Electrical Engineering
Department of Energy and Process Engineering

Simon Bjuri

Computational Fluid Dynamics of Airflows inside buildings: RANS-LES of the cavity flow benchmark

Master's thesis in Energi og miljø
Supervisor: Laurent Georges
Co-supervisor: Elyas Larkermani
June 2023

NTNU
Norwegian University of Science and Technology

Simon Bjuri

Computational Fluid Dynamics of Airflows inside buildings: RANS-LES of the cavity flow benchmark

Master's thesis in Energi og miljø
Supervisor: Laurent Georges
Co-supervisor: Elyas Larkermani
June 2023

Norwegian University of Science and Technology
Faculty of Information Technology and Electrical Engineering
Department of Energy and Process Engineering

NTNU
Norwegian University of
Science and Technology

Abstract

This thesis investigates the performances of turbulence modelling approaches using CFD for the cavity flow of a fully turbulent and transitional benchmark. Modelling such flows are critical for determining the performance of HVAC systems. Various RANS, DES and LES approaches were investigated and compared with experimental data and studies on the same benchmarks. This thesis is a continuation of Bjerkeli's master thesis [1], in which he investigated several RANS models on different cavity benchmarks. The conclusion was that no universal RANS model existed, which could perform well for all the benchmarks. Several studies have used LES on the same benchmarks as is investigated in this study [2, 3, 4]. These studies conclude that LES outperforms RANS for all the benchmarks. Using hybrid RANS-LES approaches on these benchmarks is poorly documented in the literature. The big advantage of using RANS-LES approaches is the possibility of reducing the computational effort while preserving the excellent accuracy of LES. The scope of this study was to conduct a further investigation of RANS modelling approaches on the given benchmarks, to find the upper limit achievable for RANS modelling of cavity flows. In addition, the DES and LES framework will be further investigated for cavity flow modelling. The main question this thesis aims to answer is, whether DES can produce results as accurate as LES for both the fully turbulent and transitional regimes of cavity flow.

The findings from this study were that the best RANS models to model all of the benchmarks were the $k-\omega$ models and the Spalart-Allmaras model. For the $k-\epsilon$ models, utilizing the standard wall function gave better results. However, the $k-\omega$ and the Spalart-Allmaras models produced superior results for the transitional case. The Spalart-Allmaras model gave a much better agreement with the experimental data when utilizing the vorticity/strain-based production term for the transitional case with a Reynolds number of 1000; this was not the case for the other benchmarks. Using the low-Re corrector option it was possible to obtain even better performance for the SST $k-\omega$ model and BSL $k-\omega$ model. Hence, the RANS model with the best results was the SST $k-\omega$ model with the low-Re corrector option enabled. Furthermore, URANS simulations did not provide any real benefits. For the LES approach adding synthetic turbulence at the inlet was crucial for good results. For the fully turbulent case, a turbulence intensity of 50% at the CFD inlet was found to be optimal and produced similar inlet conditions to those present in a DNS of a rectangular channel with a similar Reynolds number [5]. LES also performed well for the transitional case, with the performance of the case having a Reynolds number of 2500 could be further enhanced by correcting the synthetic turbulence at the CFD inlet. The main challenge for the DES approach was that the simulations often diverged when using synthetic turbulence at the inlet. Therefore it was not possible to recreate the good results of LES by utilizing DES. Consequently, DES could not reproduce as accurate results as LES for both the fully turbulent and transitional regimes of cavity flow.

Norsk sammendrag

Denne master oppgaven undersøker ytelsen til turbulensmodellerings metoder ved å bruke CFD på strømning i et tomt rom ved et tilfelle der man har full turbulent strømning og et annet tilfelle der man har transisjonell strømning. Modellering av slike strømninger er avgjørende for å bestemme ytelsen til HVAC systemer. Forskjellige RANS, DES og LES tilnærminger ble undersøkt og sammenlignet med eksperimetnelle data og studier gjort på de samme strømningskonfigurasjonene. Denne avhandlingen er en fortsetteles av Bjekelis masteroppgave [1], der han undersøkte RANS modeller på flere slike strømningskonfigurasjoner. Konklusjonen var at det ikke fantes noe universiell RANS modell som kunne modellere de forskjellige strømningssituasjonene knyttet til turbulens. Flere studier har brukt LES på de samme referanse konfigurasjonene som blir undersøkt i dette studiet [2, 3, 4]. Konklusjonen fra disse raportene er at LES gir bedre resultater enn RANS. Bruken av hybrid RANS-LES metoder på disse referanse konfigurasjonene er dårlig dokumentert i litteraturen. Den store fordelen med å bruke RANS-LES tilnærminger er muligheten til å redusere beregningsmengden, samtidig som man opprettholder den gode nøyaktigheten til LES. Formålet med denne master oppgaven var å gjennomføre ytterlige RANS simuleringer på konfigurasjonene for å finne den øvre grensen som kan oppnås for RANS av slike strømninger. I tillegg vil DES og LES bli ytterligere undersøkt. Hovedspørsmålet som denne master oppgaven tar sikte på å besvare, er om DES kan produsere resultater like nøyaktige som LES for både full turbulente strømninger og transisjonelle strømninger i slike rom.

Resultatet fra denne studien viste at de beste RANS modellene for å modelere alle tilfellene var $k-\omega$ modellene og Spalart-Allmaras modellen. For $k-\epsilon$ modellene ble det vist at ved å bruke standard veggfunksjon fikk man bedre resultater. Imidlertid produserte disse modellene dårligere resultater sammenlignet med $k-\omega$ modellene og Spalart-Allmaras modellen for tilfellet med transisjonell strømning. Spallart-Allmaras modellen ga en mye bedre overensstemmelse med eksperimentelle data ved brukt av vorticity/strain-basert produksjon for den transisjonelle strømningen med et Reynoldsnummer på 1000. Ved bruk av low-Re korrektorer var det mulig å oppnå en bedre ytelse for SST $k-\omega$ og BSL $k-\omega$ modellen. RANS modellen som ga de beste resultatene var SST $k-\omega$ modellen med bruk av low-Re korrektoren. Det ble også kjørt URANS simuleringer, men disse ga ingen forbedring. For LES var det avgjørende å inkludere syntetisk turbulens ved innløpet av CFD domenet for å få gode resultater. For tilfellet med full turbulens strømning ga en turbulens intensitet på 50% de beste resultatene, og reproduserte lignende inngangsforhold som i en DNS av en rektangulær kanal med tilsvarende Reynoldsnummer [5]. LES ga også gode resultater for tilfellet med transisjonell strømning, men for tilfellet med et Reynoldsnummer på 2500 kunne resultatene forbedres ytterliger ved å optimalisere den syntetiske turbulensen som blir brukt ved innløpet av CFD domenet. Den største utfordringen ved DES var at simuleringene ofte divergerte ved bruk av syntetisk turbulens ved innløpet. Derfor var det ikke mulig å gjenskape de gode resultatene fra LES ved å bruke DES. Dermed, kunne DES ikke gjenskape like nøyaktige resultater som LES for det fulle turbulente og transisjonelle tilfellet.

Preface

I would like to express my gratitude towards my supervisor Prof. Laurent Georges and co-supervisor, Elyas Elyas Larkermani, for their invaluable expertise and guidance throughout my master thesis. I would also like to express my heartfelt appreciation to my friends, family, and fellow students for their unwavering support and motivation. The successful completion of this thesis would not have been possible without the aid of the Idun and Fram cluster.

This master thesis is an extension of the specialization project written by the same author in the fall 2022. The focus of that project was mainly on RANS modelling and a comprehensive literature review on RANS and LES of cavity flows. While some sections from the theory and literature review have been repurposed, they have been modified and expanded to align with the scope of this thesis better.

Table of Contents

List of Figures

List of Tables

1 Introduction

According to a report from the U.S Environmental Protection Agency (EPA) from 1989, the average American spends 90% of their time indoors [6]. This emphasizes the importance of heating, ventilation, and air conditioning (HVAC) systems in maintaining human health and wellness. HVAC systems play a vital role in improving indoor air quality and reducing indoor air pollutants, leading to increased productivity and reduced exposure to viruses, chemicals, and other diseases. Particularly during the Covid-19 pandemic, the demand for good ventilation increased. This is because good ventilation is used to lower the concentration of the virus in the air, and also decrease surface contamination by removing the virus particles before they can land on surfaces [7]. A good HVAC system is also essential in operating rooms to maintain a safe microenvironment and lower mortality rates. NTNU has dedicated significant resources to its operation room laboratory, where numerous projects are underway [8]. HVAC systems also consume a significant amount of energy. In an analysis by Pérez-Lombard et al. it was concluded that the energy consumption by HVAC systems contributed to 10-20% of developed countries total energy consumption [9]. HVAC systems must become more efficient to achieve the EU's goal of becoming climate-neutral by 2050.

The physics of HVAC systems within a building and room are complex due to the turbulent flow induced by the air. Turbulent structures dominate the flow field, resulting in chaotic behaviour with more fluctuations of flow quantities. Temperature differences within a room can also significantly impact the flow field, for example, floor heating might have a big effect on the air inside the room. The combination of these two effects makes it hard to investigate HVAC systems properly without large errors. There are two ways to investigate HVAC systems, either by conducting experiments or by making a model. It can be expensive to investigate different HVAC configurations by conducting different experiments, as there are a limited number of such laboratories. it is also not always straightforward to get every flow parameter correctly and minimize the error from such experiments. Additionally, it can be difficult to change small parameters between every experiment. Because of these reasons modelling these systems can be preferred. However, models must be validated with experiments. The most common models used for building HVAC systems are single-zone or multi-zone models, with the latter being more accurate. Here the building is split into multiple zones, often one zone per room, and the mass flow between each zone is calculated. However, these models only calculate the airflow pattern between these zones and do not calculate the airflow patterns within these zones [10]. Computational Fluid Mechanics (CFD) methods are used to calculate cavity airflow within zones.

CFD solves for the velocity, pressure, and temperature field numerically. Modelling turbulence using CFD for flows within a room is challenging due to the significant impact even the smallest eddies can have on the entire flow field. There are three main methods used for turbulence in CFD. Firstly the smallest eddies can be resolved directly by creating a numerical mesh that is refined enough to capture the smallest eddies, which is done in a Direct Numerical Simulation (DNS). However, this is very computationally expensive and is not possible for every flow configuration. Another approach is to have a refined enough mesh for the biggest eddies while modelling the smaller eddies not captured by the mesh. This approach is done in a Large Eddy Simulation (LES), and is less accurate than a DNS, but also less computationally expensive. The final approach is to model the turbulence using a modified version of the Navier-Stokes equation to solve for the averaged velocity and pressure field. This approach is called Reynolds Averaged Navier-Stokes (RANS) modelling, and has less accuracy than LES but is not as computationally expensive. Many different RANS models exist, which are used for different flow configurations. There are also hybrid RANS-LES models which use the RANS framework near walls and LES in the far-wall region. The Detached Eddy Simulation (DES) is an example of such an approach. Hence, many different options exist when modelling turbulence.

The conclusion drawn from Bjerkeli's master thesis [1], which forms the basis of this thesis, is that there is no universal RANS model capable of producing accurate results for both transitional and fully turbulent flow inside a cavity. However, LES approaches have shown promise in achieving good results for both flow regimes. Taghinia et al. [2], along with Zasimova et al. [3], were able to obtain good results using LES and hybrid LES-RANS approaches on a fully turbulent flow case. Similarly, Van Hooff et al. [4] were able to simulate a transitional flow case using LES

successfully with high accuracy. While LES approach can accurately simulate cavity flows for both flow regimes, they require significant computational effort and simulation time.

The scope of this thesis is to investigate RANS modelling of both fully turbulent and transitional flow configurations. The aim is to determine the limits of what can be achieved with RANS modelling for both flow regimes and compare these results with those obtained in Bjerklie's master thesis [1] and simulations conducted by other groups on the same flow configurations. The DES framework will then be implemented on both the fully turbulent flow benchmark and the transitional flow configuration. The main objective of this thesis is to answer the crucial question of whether DES can produce results as accurate as LES for both the fully turbulent and transitional regimes of cavity flow. Answering this question is of great significance, as if DES can provide the same accuracy as LES, it can then be used in all future cavity flow simulations where accuracy is important, thus reducing the computational effort required while maintaining the same level of accuracy. This could lead to DES becoming the new standard for modelling industrial HVAC systems and airflow inside buildings as computational power continues to improve.

2 Theory

The text and content from this section are taken from the specialization project of Bjuri [11], and are slightly modified so the content fits better with this study.

2.1 Governing equations

The airflow distribution in an enclosed room is governed by the continuity equation (1) and the Navier-Stokes equations (2), (3), (4). The equations are here written in the conservative partial derivative form taken from Malalasekera and Versteeg [12]:

$$\frac{\partial \rho}{\partial t} + \nabla \cdot (\rho \mathbf{u}) = 0 \tag{1}$$

$$\frac{\partial (\rho u)}{\partial t} + \nabla \cdot (\rho u \mathbf{u}) = -\frac{\partial p}{\partial x} + \nabla \cdot (\mu \nabla u) + S_{M_x} \tag{2}$$

$$\frac{\partial (\rho v)}{\partial t} + \nabla \cdot (\rho v \mathbf{u}) = -\frac{\partial p}{\partial y} + \nabla \cdot (\mu \nabla v) + S_{M_y} \tag{3}$$

$$\frac{\partial (\rho w)}{\partial t} + \nabla \cdot (\rho w \mathbf{u}) = -\frac{\partial p}{\partial z} + \nabla \cdot (\mu \nabla w) + S_{M_z} \tag{4}$$

In these equations, the velocity components in the x, y, and z directions are represented by u, v, and w respectively. $\mathbf{u}$ is the velocity vector, ρ is the density of the fluid, p is the pressure, μ is the dynamic viscosity of the fluid, S_M is a momentum source term and t is the time.

Furthermore, a fluid is incompressible when the non-dimensional Mach number described in equation (5) has a value under 0.3 [13]. This simplifies the continuity equation to equation (6) and the momentum equations to equation (7).

$$Ma = \frac{U}{\sqrt{\gamma R T}} \tag{5}$$

$$\nabla \cdot \mathbf{u} = 0 \tag{6}$$

$$\frac{\partial \mathbf{u}}{\partial t} + (\mathbf{u} \cdot \nabla)\mathbf{u} = -\frac{1}{\rho}\nabla p + \nu \nabla^2 u + S_M \tag{7}$$

Here γ is the ratio of specific heat, R is the ideal gas constant, T is the static temperature, U is the velocity magnitude and ν is the kinematic viscosity. These equations are now written in a more compact form using vector notation.

In nature, certain flow phenomena are categorized as steady flow, meaning that the flow characteristics remain constant over time. An example of this is laminar flow over a flat plate. In steady flow, all time derivatives in the governing equations (1-4) are zero. The opposite of steady flow is unsteady flow, where flow quantities change with time, and more chaotic behaviour is observed.

2.2 Cavity flow

One can approximate the flow of a mixing ventilation system as a cavity flow, as illustrated in figure 1. For this project, the flow configuration will resemble figure 1, with a velocity inlet at

the upper left corner and a pressure outlet at the lower right corner. A large recirculating vortex is formed in the cavity, responsible for mixing the incoming air with the air in the cavity. The efficiency of the ventilation system is mainly determined by this vortex. At the top wall by the inlet, there is a wall jet region where the jet follows the top wall until the jet detachment point. At this point, the jet detaches from the wall, and some of the jets flow through the outlet, while other parts of the jet flow through the recirculating vortex. Secondary flow phenomena may occur at the upper right and lower left corner, creating vortices in this area.

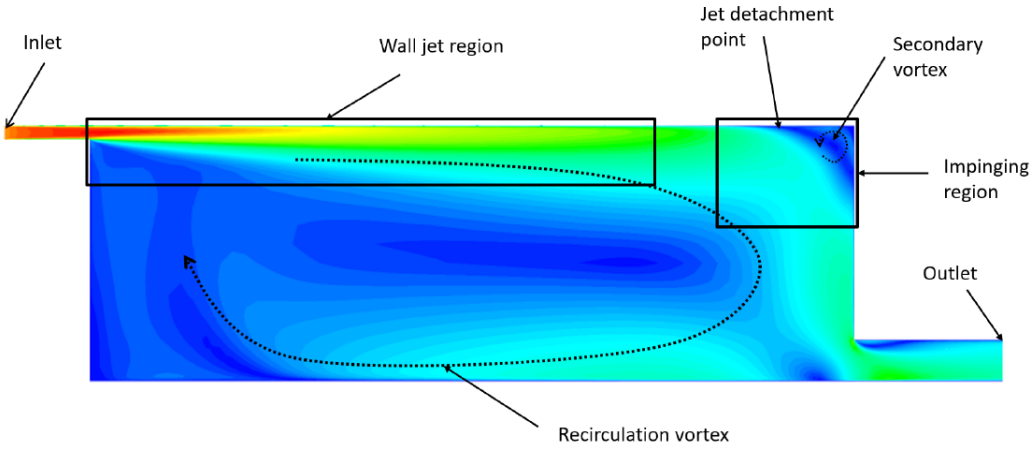

Figure 1: The usual flow features of a cavity flow figure is taken from Bjerkeli[1].

2.3 Turbulence

The characteristic flow regime is determined by the non-dimensional Reynolds number, which is given in equation (8). Here L is a given length scale and U is a velocity scale, which depends on the flow configuration.

$$Re = \frac{\rho U L}{\mu} = \frac{UL}{\nu} \tag{8}$$

If the Reynolds number is low the flow is laminar and if it has a high value the flow is turbulent. Turbulent flow is characterized by chaotic behaviour with more mixing than the laminar case. The critical Reynolds number is the number where the flow transitions from laminar to turbulent. However, the switch from laminar to turbulent does not happen spontaneously, but rather gradually. This means that between the laminar and turbulent flow regimes, there exists a transitional flow regime, where the flow is neither laminar nor turbulent. Figure 2 from [14] shows the different flow regimes when the flow is passing through a grid.

At what Reynolds number this transition occurs depends on the geometry of the experimental configuration. For internal pipe flow the critical Reynolds number is around 2300, while for external flow over a flat plate, the critical Reynolds number is around 500 000 [15], these numbers are found through experiments.

The critical Reynolds number is not always well documented. This is the case for the cavity flow where fewer experiments have been conducted. For this flow configuration, the velocity used for calculating the Reynolds number (8) is the inlet bulk velocity entering the cavity, while the length scale used is the height of the inlet duct. Nielsen showed in an experiment on flow in a cavity that a Reynolds number of 5000 gave a fully turbulent flow [16]. In Nielsen's PhD thesis [17], he observed that unsteady flow conditions were present for cavity flow between the Reynolds numbers of 2000 and 10000. From experiments done by Van Hooff et al. [18], on a cavity flow with different geometry, it was observed that the flow was transitional in the Reynolds number range 300-2500, and above a Reynolds number of 2500 the flow was more or less fully turbulent.

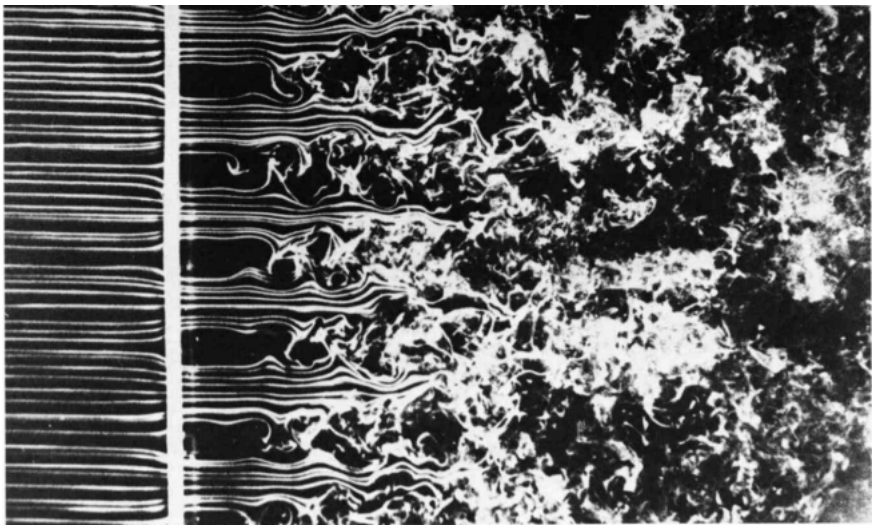

Figure 2: Laminar flow from the left passing through a grid generating turbulence, taken from [14]

Turbulent flow presents a challenge to model accurately, because of the large differences between the length scales present in the flow. These differences range from the largest recirculation vortices to the smallest eddies of the Kolmogorov scale η, which interact with one another. The difficult part is that these scales interact with each other. So in order to resolve the entire flow field, the grid size needs to be so small that the smallest eddies are captured by the mesh. This is exactly what is done in a DNS, which makes the simulation very accurate. However, a DNS requires many cells in order to resolve the smallest eddies, which means that it is extremely computationally expensive. The computational effort required by DNS scales approximately with the cube of the Reynolds number [19]. As a result, DNS is mostly used in research, where high-performance computing (HPC) is more accessible and is mostly used for "simple" flow configurations.

To use less computational power, turbulence approaches such as LES and RANS are better suited, although these methods offer lower accuracy. In LES, the effect of the smallest eddies is modelled while the other eddies are directly resolved, this gives less accuracy but also requires less computational power compared to DNS. While RANS solves for the average velocity field, which gives even less accuracy but also requires less computational power than LES. Currently, RANS URANS and DES are the most popular modelling approaches for complex industry problems [19]. However, as computational power continues to improve, LES is expected to become a more common turbulence approach in the future.

2.4 RANS modeling

In RANS modeling the main goal is to solve the RANS equations. Solving these equations gives the average velocity and pressure field. These equations are derived from the Navier-Stokes equations (2-4) by utilizing the Reynolds decomposition technique. This technique involves breaking down the velocity and pressure components into their mean and fluctuating quantities, as shown in equation (9).

$$u(x,t) = \overline{u}(x) + u'(x,t) \tag{9}$$

The mean velocity is denoted by $\overline{u}$ and the fluctuating velocity is represented by u'. Similarly can be done for the pressure.

By substituting the Reynolds decomposed quantities into the Navier-Stokes equations (1-4), and the equations also are Reynolds averaged in time, then the RANS equations (10) can be derived. The RANS equations and the remaining equations in this section are written in Einstein notation [20].

$$\frac{\partial \overline{u_i}}{\partial t} + \overline{u_i}\frac{\partial \overline{u_i}}{\partial x_j} = -\frac{1}{\rho}\frac{\partial \overline{p}}{\partial x_i} + \frac{\partial}{\partial x_j}(\nu\frac{\partial \overline{u_i}}{\partial x_j} - \overline{u_i' u_j'}) \tag{10}$$

In the RANS equations, the averaged quantities are being solved, but the term $\overline{u_i' u_j'}$ is unknown and is called the Reynolds stress term. In 1877, Boussinesq approximated this term by the mean velocity gradient and an eddy viscosity ν_t term see equation (11).

$$\overline{u_i' u_j'} = -2\nu_t S_{ij} + \frac{2}{3}k\delta_{ij} \tag{11}$$

Here k is the turbulent kinetic energy, δ_{ij} is the Kroenker function as described in (12) and S_{ij} is the rate of strain tensor described in equation (13).

$$\delta_{ij} = \begin{cases} 0 & \text{if i} \neq \text{j} \\ 1 & \text{if i=j} \end{cases} \tag{12}$$

$$S_{ij} = \frac{1}{2}(\frac{\partial \overline{u_i}}{\partial x_j} + \frac{\partial \overline{u_j}}{\partial x_i}) \tag{13}$$

To use the RANS approach to model turbulence, it is only necessary to calculate the turbulent viscosity ν_t. The different RANS turbulence models have different ways to calculate the turbulent viscosity.

2.4.1 Spalart-Allmaras model

The Spalart-Allmaras method was proposed in 1992 to model the flow where a negative pressure gradient was present, for example, the flow over an airfoil. Thus this model works well for predicting wall-bounded flows, but does not work well for free shear flows [21]. The Spalart-Allmaras method solves one additional transport equation (14) for the Spalart-Allmaras variable $\tilde{\nu}$ which is given in (15).

$$\frac{\partial}{\partial t}(\rho\tilde{\nu}) + \frac{\partial}{\partial x_i}(\rho\tilde{\nu}\overline{u}_i) = G_\nu + \frac{1}{\sigma_{\tilde{\nu}}}\left(\frac{\partial}{\partial x_j}\big((\mu + \rho\tilde{\nu})\frac{\partial \tilde{\nu}}{\partial x_j}\big) + C_{b2}\rho(\frac{\tilde{\nu}}{\partial x_j})^2)\right) - Y_\nu + S_{\tilde{\nu}} \tag{14}$$

$$\nu_t = \tilde{\nu} f_{v1} \quad , \quad f_{v1} = \frac{\chi^3}{\chi^3 + c_{v1}^3} \quad , \quad \chi = \frac{\tilde{\nu}}{\nu} \tag{15}$$

G_ν, $\sigma_{\tilde{\nu}}$, C_{b2}, Y_ν, $S_{\tilde{\nu}}$ and $c_{\nu 1}$ are all empirical constants. These constants are given in [22]. The Spalart Allmaras model also has two options in Ansys Fluent, Vorticity-Based Production or Strain/Vorticity-Based-Production, the difference being how the production term is modelled, for details read the Fluent theory guide [21]. The Strain/Vorticity-Based production term is better suited for predicting flow behaviour inside vortices.

2.4.2 K-ϵ models

The family of k-ϵ turbulence models are one of the most popular models in industry flow and heat transfer flow applications [21]. In the model two additional transport equations for the turbulent kinetic energy k and the dissipation rate ϵ are being solved. These quantities are then used to calculate the turbulent viscosity μ_T shown in equation (18). Equations (16) and (17) show the transport equation for k and ϵ for the standard k-ϵ model.

$$\frac{\partial}{\partial t}(\rho k) + \frac{\partial}{\partial x_i}(\rho k \overline{u}_i) = \frac{\partial}{\partial x_j}\left(\left(\mu + \frac{\mu_t}{\sigma_k}\right)\frac{\partial k}{\partial x_j}\right) + G_k + G_b - \rho\epsilon - Y_M + S_k \tag{16}$$

$$\frac{\partial}{\partial t}(\rho \epsilon) + \frac{\partial}{\partial x_i}(\rho \epsilon \overline{u}_i) = \frac{\partial}{\partial x_j}\left(\left(\mu + \frac{\mu_t}{\sigma_\epsilon}\right)\frac{\partial \epsilon}{\partial x_j}\right) + C_{1\epsilon}\frac{\epsilon}{k}(G_k + C_{3\epsilon}G_b) - C_{2\epsilon}\rho\frac{\epsilon^2}{K} + s_\epsilon \tag{17}$$

$$\mu_T = \rho C_\mu \frac{k^2}{\epsilon} \tag{18}$$

G_k, G_b, Y_M, $C_{1\epsilon}$, $C_{2\epsilon}$, $C_{3\epsilon}$ and s_ϵ are here empirical constants. The values for all the constants in the transport equations can be found in the Fluent theory guide [21]. The k-ϵ model assumes fully turbulent flow and is strictly speaking only valid for these flows. Hence the model predicts free-shear flow well, but struggles with wall-bounded flows. There are 3 main k-ϵ models: standard, RNG and realizable $k-\epsilon$ model. The main difference between the standard, RNG and realizable $k-\epsilon$, is that they use different transport equations for ϵ. Both the RNG and realizable give an improvement for flows with strong streamline curvature, vortices and rotations [21].

2.4.3 K-ω models

Because of the weaknesses of the prediction of wall-bounded flow by the k-ϵ models, the family of k-ω models was implemented. These models improve the effect of negative pressure gradients at the walls, but give a worse prediction at the free stream. The model calculates the turbulent viscosity μ_T as shown in equation (21) through 2 additional transport equations for k and the specific turbulence dissipation rate ω. These transport equations (19) and (20) are here given for the standard k-ω model.

$$\frac{\partial}{\partial t}(\rho k) + \frac{\partial}{\partial x_i}(\rho k \overline{u}_i) = \frac{\partial}{\partial x_j}\left(\Gamma_k \frac{\partial k}{\partial x_j}\right) + G_k - Y_k + S_k \tag{19}$$

$$\frac{\partial}{\partial t}(\rho \omega) + \frac{\partial}{\partial x_i}(\rho \omega \overline{u_i}) = \frac{\partial}{\partial x_j}\left(\Gamma_\omega \frac{\partial \omega}{\partial x_j}\right) + G_\omega - Y_\omega + S_\omega \tag{20}$$

$$\mu_t = \alpha^* \frac{\rho k}{\omega} \tag{21}$$

Γ_k, G_k, Y_k, S_k, Γ_ω, G_ω, Y_ω, S_ω and α^* are empirical constants. The constants can be found in the theory guide of Fluent [21]. Furthermore, to improve the k-ω model's prediction of the free-shear flow, Menter [23] made the improved k-ω Shear-Stress Transport (SST) model. This method blends the standard k-ω method at the near-wall region and the standard k-ϵ method at the far field through a blending function. By doing this, one gets the strength of both models while eliminating the weakness of both models. This method is commonly used today in industrial simulations [21]. The transport equations for k and ω are the same as the ones from equations (19) and (20), but the constants change slightly. The turbulent viscosity is now defined as (22).

$$\mu_t = \frac{\rho k}{\omega} \frac{1}{max\left(\frac{1}{\alpha^*}, \frac{SF_2}{a_1 \omega}\right)} \tag{22}$$

α^*, S, F_2 and a_1 are empirical constant defined in [23]. In addition, there are two more k-ω turbulence models in Ansys Fluent: BSL model and GEKO model. The BSL method is almost identical to the SST method, only the turbulent viscosity is defined the same way as for standard k-ω (21), and one constant (σ_{k1}) is different [24]. The GEKO method was implemented by Ansys Fluent to provide the users more flexibility in the tuning of the parameters. Doing this the user can use this method for many different flow applications by just tuning the parameters [25].

2.4.4 Unsteadiness of RANS

The RANS models discussed earlier can sometimes exhibit oscillating behaviour, which is characterized by fluctuating residuals and flow quantities that may differ between iterations. This is because these models struggle to find a steady-state solution for the flow configuration, which is often the case for cavity flow. The models may oscillate between different steady-state solutions, such as having three recirculation vortices and two within the cavity. Figure 3 illustrates how a residual plot may appear when this behaviour occurs. In such situations, a statistical averaging approach is necessary to gather flow quantities. The flow quantities must be averaged over a sufficient number of iterations to capture the entire oscillating behaviour.

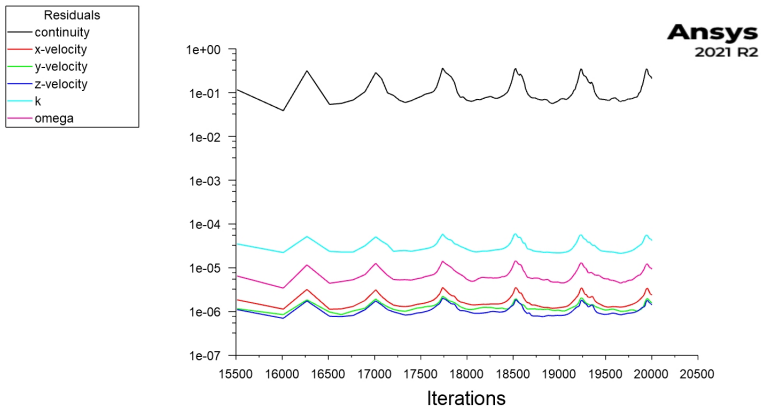

Figure 3: Oscillating residuals due to RANS modeling

2.4.5 RANS correctors and other options

Fluent has a variety of correctors and other options available that can improve the accuracy of RANS simulations for specific geometries and flow configurations. This section describes several of these options and correctors.

In all the two-equations models there is an option to activate a production limiter. This limiter restricts the production term of the turbulent kinetic energy as can be seen in equation (23). This limiter prevents an unphysical increase of the turbulent kinetic energy in stagnant regions.

$$G_k = min(G_k, 10\beta^* k\omega) \tag{23}$$

β^* is a constant given in [21].

For the $k-\omega$ models, there is an option in fluent called Low-Re corrector. This option is meant for low Reynolds number flows and dampens the turbulent viscosity by a coefficient α^* given in equation (24).

$$\alpha^* = \alpha^*_\infty(\frac{\alpha^*_0 + Re_t/R_k}{1 + Re_t/R_k}) \tag{24}$$

α^*_∞, α^*_0 and R_k are empirical constant, while $Re_t = \frac{\rho k}{\mu\omega}$.

When using the $k-\omega$ models and the Spalart-Allmaras model in Fluent, there is an option to apply corner flow correction. This correction improves the accuracy of predictions for secondary flow phenomena like corner flows. By utilizing this correction, flow separation can be predicted more accurately, as the flow from the corner keeps the flow attached for a longer period. For more information on this correction, it is recommended to refer to the Fluent theory guide [21].

2.4.6 URANS

In RANS modelling, the average velocity field's steady-state solution is obtained. However, as turbulence is an unsteady phenomenon where all flow quantities vary with time, URANS methods have become a popular alternative to RANS modelling. Instead of the RANS equations (10), the Unsteady Reynolds-Averaged Navier-Stokes (URANS) equations are solved in URANS simulations. These equations are similar to the RANS equations, with the only difference being the extra time derivative terms in the URANS equations. Consequently, the results obtained from a URANS simulation show how the averaged velocity field changes with time. The RANS models described in sections (2.4.1-2.4.3) can also be applied in URANS simulations.

As URANS provides time-varying quantities, a statistical averaging approach is implemented to obtain averaged variables. To obtain good steady-state results from an unsteady simulation, it is crucial to determine when the averaging should start and how long the averaging process should last. The averaging should start when the system is in the "statistical steady-state," meaning that the global variables describing the system oscillate between two values. These global variables could, for example, be the residuals or the total turbulent kinetic energy of the system. The variables are then averaged over a specific period. For cavity flow, the Flow Through Time (FTT), also known as t^*, is commonly used as an indication of how long the averaging approach should last. FTT is the time taken for the air to do one circulation around the cavity. The report of Van Hooff et al. [4] recommends averaging over $20 \cdot t^*$, where t^* is defined in equation (25).

$$t^* = \frac{P}{U_{average}} \tag{25}$$

$U_{average}$ is the average velocity of the circulating jet, and P is the perimeter of the enclosed room.

2.5 LES

The LES method solves the filtered Navier-Stokes equations (28), and uses a Subgrid-Scale model for the eddies that the mesh is not able to resolve. In turbulent flows, eddies undergo a breakdown process into smaller ones until they are finally dissipated into heat through molecular viscosity. This process is measured by the dissipation rate ϵ, which is defined as (26).

$$\epsilon = \nu \frac{\partial \overline{u_i}}{\partial x_j} \frac{\partial \overline{u_i}}{\partial x_j} \tag{26}$$

From equation (26) it is observed that the dissipation increases with the velocity gradient of the flow. Smaller eddies have a higher velocity gradient than larger ones. However, the velocity gradient of the smallest eddies captured by the mesh is not high enough for them to dissipate. To address this, an artificial viscosity ν_{sgs} is implemented in the LES approach to ensure that the smallest eddies dissipate. This additional viscosity increases the dissipation rate to (27), and modifies the Navier-Stokes equation to (28). The calculation of ν_{sgs} and τ_{sgs} depends on the Subgrid-Scale Model (SGS) being used. There are several SGS models, such as the Smagorinsky-Lilly, Dynamic Smagorinsky-Lilly, and Wall-Adapting Local Eddy-viscosity (WALE) [21].

$$\epsilon = (\nu + \nu_{sgs}) \frac{\partial \overline{u_i}}{\partial x_j} \frac{\partial \overline{u_i}}{\partial x_j} \tag{27}$$

$$\frac{\partial (\rho \overline{u_i})}{\partial t} + \frac{\partial}{\partial x_j}(\rho \overline{u_i u_j}) = -\frac{\partial \overline{p}}{\partial x_i} + \frac{\partial}{\partial x_i}(\tau_{ij} + \tau_{sgs}) \tag{28}$$

Here $\overline{u}$ is the filtered velocity components and $\overline{p}$ is the filtered pressure.

For the Smagorinsky-Lilly model, the Subgrid-Scale viscosity is given by equation (29).

$$\nu_{sgs} = (L_s)^2\sqrt{2S_{ij}S_{ij}} \quad \text{and} \quad L_s = min(\kappa d, C_s\Delta) \tag{29}$$

$\kappa = 0.41$ is the Von Kármán constant, d is the distance to the wall, Δ is the local grid scale and C_s is the Smagorinsky constant. In Fluent the local grid scale is computed using $\Delta = V^{1/3}$, where V is the volume of the cell [21]. Lilly derived the value $C_s = 0.173$ for homogenous isentropic turbulence, meaning that effects from walls were neglected. Using this constant value overpredicts the subgrid stresses in shear regions and regions near walls. However, dampening functions exist that modify the eddy viscosity in these areas. Nevertheless, there does not exist a universal value for the Smagorinsky constant, which can be used with good accuracy for all turbulent flow configurations. To deal with this issue the dynamic Smagorinsky-Lilly model was derived. The idea of this approach is to use an additional test filter, which is used to gather the value of the Smagorinsky constant, for more details read through [26]. The result of this is that the Smagorinsky constant changes based on what flow physics is present.

LES as mentioned is expensive, and the expensiveness of the LES scales with the Reynolds number. Because of this another popular approach is Wall-Modeled LES (WMLES), which uses a wall model close to the wall. This replaces the need to resolve the near-wall region. This model predicts the behaviour of the turbulence near the wall based on its properties in the outer flow region, where it can be resolved with a coarser grid. Because the inner part of the boundary layer is responsible for the proportionality between the Reynolds number and the computational expensiveness of the RANS, the WMLES can be applied to an increasing Reynolds number without the simulation being more expensive [21]. The subgrid turbulent viscosity used in the WMLES for Fluent is given in equation (30).

$$\nu_{sgs} = min\left((\kappa d_w)^2, (C_{Smag}\Delta)^2\right) \cdot S_{ij} \cdot \left(1 - exp\left(-\left(\frac{y^+}{25}\right)^3\right)\right) \tag{30}$$

$\kappa = 0.4187$ and $C_{Smag} = 0.2$ are constants, d_w is the distance to the wall and Δ is the modified grid scale given in [21].

Another wall-modelled LES approach is the WMLES $S - \Omega$ model which is available in Fluent. This model replaces the S_{ij} term in equation (30) with the term $abs(S_{ij} - \Omega)$, where Ω is the vorticity magnitude. The benefit of this model is more realistic subgrid turbulent viscosities in the shear layers and the computation of transitional effects [21].

To ensure a successful LES approach, it is crucial that the mesh is adequately refined, allowing SGS modelling only to be utilized for the smallest eddies. According to Pope's recommendation in [27], it is best to refine the mesh in a way that enables 80% of the turbulent kinetic energy to be resolved through the mesh while the remaining 20% is modelled via the SGS model. This means that the turbulent kinetic energy from the smallest eddies is modelled through the SGS, while the turbulent kinetic energy from the largest eddies are resolved from the mesh. This is shown in figure 4.

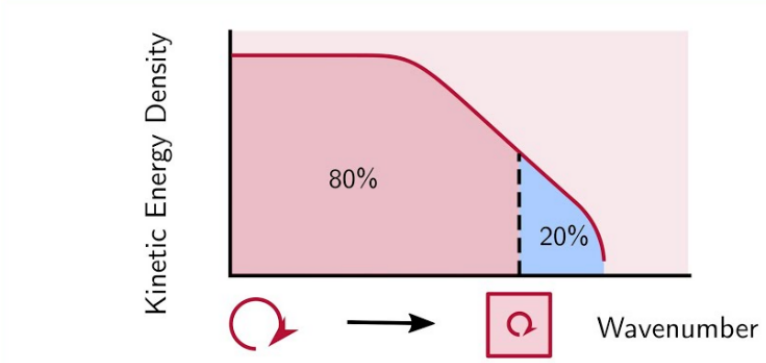

Figure 4: The turbulent kinetic energy cascade, as wave number increases the eddies get smaller. Here 80% of the turbulent kinetic energy is resolved by the mesh.

In order to assess if a mesh is suitable for LES, one can use the integral length scale (l_0) as a metric. The integral length scale is a measure of the length of an eddy at the average turbulent kinetic energy. This quantity can be calculated before performing the LES, from a RANS solution using either equation (31) or (32).

$$l_0 = \frac{k^{3/2}}{\epsilon} \tag{31}$$

$$l_0 = \frac{k^{1/2}}{C_\mu \omega} \tag{32}$$

Here C_μ is an empirical constant and has the value 0.09.

For the recommendation that the mesh resolves 80% of the turbulent kinetic energy, it is further recommended that 5 cells are used across the integral length scale. This is equivalent to that, the function defined in equation (33) is larger than 5. If this is satisfied, the local cell size is small enough for the usage of LES otherwise, the local cell should be further refined. For a DES it is only important that the far-field region is refined enough for LES, while the wall region does not have to be as refined.

$$f = \frac{l_0}{\Delta} \quad , \quad \Delta = \text{Cell volume}^{1/3} \tag{33}$$

To determine the time-dependent variables, LES and DES require a statistical averaging approach similar to the one outlined in section 2.4.6.

2.5.1 DES

In Fluent there exist three different DES models: DES Spalart-Allmaras, DES realizable $k-\epsilon$ and DES SST $k-\omega$. These models differ based on the RANS model used in the RANS region and the criteria for transitioning between RANS and LES.

The DES Spalart-Allmaras is the original DES model proposed by Shur [28]. This model replaces the length scale d that is used for the Spalart-Allmaras model with the modified length scale $\tilde{d}$, which is defined in equation (34). It utilizes the Spalart-Allmaras model in the RANS region.

$$\tilde{d} = min(d, C_{des}\Delta_{max}) \tag{34}$$

C_{DES} is an empirical constant equal to 0.65 and Δ_{max} is the maximum edge length for hexahedral cells.

This means that LES is used when $C_{des}\Delta_{max} < \tilde{d}$ and RANS is used otherwise. Meaning that RANS is used in the near-wall region, while LES is used in the far-wall region. Furthermore, this has the consequence of the transition between RANS and LES only being dependent on the refinement of the mesh. In other words, it is possible to know the region where LES and RANS are activated before running the simulation.

Another DES model is the DES realizable $k-\epsilon$ as described in Fluent theory guide [21]. This model uses the same terms as the realizable $k-\epsilon$, except for the dissipation which is modified as shown in equation (35). This model utilizes the realizable $k-\epsilon$ model in the RANS region.

$$G_k = \frac{\rho k^{\frac{3}{2}}}{l_{des}} \tag{35}$$

Where

$$l_{des} = min(l_{rke}, l_{les}) \quad , \quad l_{rke} = \frac{k^{\frac{3}{2}}}{\epsilon} \quad \text{and} \quad l_{les} = C_{des}\Delta_{max} \tag{36}$$

This results in, the transition relying on both mesh refinement and turbulent quantities, making it hard to determine the exact point where the transition from RANS to LES occurs before running a simulation.

The last DES model available in Fluent is the DES SST $k-\omega$ model proposed by Menter [29]. This model changes the dissipation term of the turbulent kinetic energy transport equation to equation (37). This model uses the SST $k-\omega$ model in the RANS region.

$$Y_k = \rho\beta^* k\omega F_{DES} \tag{37}$$

Where F_{DES} is given as

$$F_{DES} = max(\frac{L_t}{C_{des}\Delta_{max}}, 1) \quad \text{and} \quad L_t = \frac{\sqrt{k}}{\beta^*\omega} \tag{38}$$

This means that LES is activated when $C_{des}\Delta_{max} < l_t$, otherwise RANS is utilized. β^* is here an empirical constant given in [29]. The transition depends on both the mesh refinement and also the turbulent quantities. This results in not knowing where the transition happens prior to the simulation.

For all of the DES models described above there is the possibility to use the delayed option in Fluent. This option delays the transition in order to keep the entire boundary layer inside of the RANS region.

Grey areas are present at the transition between RANS and LES, which can lead to a depletion of turbulent structures in the LES region. This can happen because of the RANS region dampening the turbulent structures in the flow, which is needed for the LES region. The result from this can be that the simulation underpredicts the number of turbulent structures apparent in the flow. This effect is often referred to as Modeled Stress Depletion (MSD). For wall-bounded flow, this can lead to earlier separation a so-called Grid Induced Separation (GIS), due to the flow being less turbulent. Also for flow with a shear layer, this effect can lead to less turbulent mixing in the shear layer, which in turn leads to less diffusion of the velocity and a sharper velocity profile [30].

2.6 Boundary conditons

In order to obtain accurate results from a CFD simulation, it is crucial to carefully consider the boundary conditions. This section will specifically address two types of boundary conditions- wall and free-flow boundary conditions.

2.6.1 Wall boundary condition

Before discussing how the wall boundary conditions are modelled in CFD, a further investigation of how the flow acts near the wall will be held. Flow near a wall will create a boundary layer, where the flow varies from having the free stream's velocity to zero at the wall due to the no-slip condition. This region plays a crucial role in both the generation and dissipation of turbulence. All boundary layers will have the same self-similar profile, which has been found through experiments. This profile is called the "Law of The Wall", which is a non-dimensional velocity profile, which is identical for all boundary layers. This profile uses non-dimensional quantities, namely u^+ and y^+, as defined in equations (39) and (40).

$$u^+ = \frac{u}{u_\tau} \tag{39}$$

$$y^+ = y\frac{u_\tau}{\nu} \tag{40}$$

$$u_\tau = \sqrt{\frac{\tau_{wall}}{\rho}} \tag{41}$$

u_τ is the so-called friction velocity and τ_{wall} is the wall shear stress. When calculating y^+ (40), the friction velocity used is defined in equation (41).

In the literature y^* can also be used for the non-dimensional y value near the boundary layer. It uses the friction velocity which is defined in equation (42). Inserting equation(42) into equation (40), the following equation for y^* is obtained (43).

$$u_\tau = \sqrt{C_\mu^{1/2} k_p} \tag{42}$$

$$y^* = \frac{\rho y \left(\sqrt{C_\mu^{1/2} k_p}\right)}{\mu} \tag{43}$$

C_μ is an empirical constant and k_p is the turbulent kinetic energy.

The Law of The Wall is divided into three main regions. The region closest to the wall when $y^+ < 5$ is called the viscous sub-layer, in this region the non-dimensional velocity follows a linear profile as the flow acts laminar. The region furthest away from the wall $30 < y^+ < 300$ is called the log-law sub-layer, in this region the non-dimensional velocity follows a logarithmic function. The region between these regions is called the buffer sub-layer, in this region the non-dimensional velocity profile transitions from the viscous sub-layer to the log-law sub-layer. The Law of The Wall can be seen in figure 5.

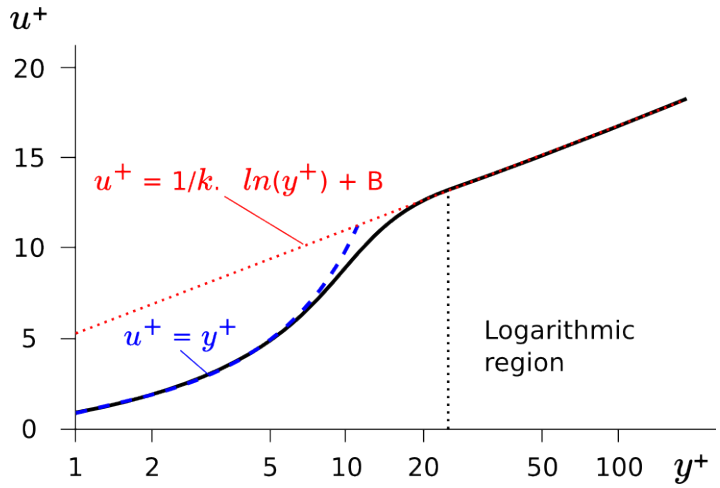

Figure 5: Law of The Wall

There are two modelling approaches for modelling the near-wall region. Either the mesh can resolve the entire Law of The Wall or wall functions can be utilized. Resolving the entire region of the Law of The Wall is quite computationally expensive and can lead to high aspect ratios, especially for high Reynolds number flows. Hence wall functions are often used in these cases. Wall function should be used when the y^+ is large enough to be inside of the logarithmic region. The flow variables in a CFD simulation vary linearly between two nodes. However, the flow quantities do not vary linearly in experiments between those two nodes. This results in the CFD simulation under predicting the viscous stresses near the wall, which is defined in equation (44).

$$\tau = \mu \frac{\partial u}{\partial y} \tag{44}$$

To correct for this under prediction the wall function modifies the viscosity, such that the low viscous stresses at the walls are corrected. The modified shear stresses at the wall for the CFD velocity profile are given in equation (45), and the modified viscosity is given by equation (46).

$$\tau_{wall} = -\rho \nu_{wall} \frac{U}{y} \tag{45}$$

$$\nu_{wall} = \nu \left(\frac{y^+}{f(y^+)} \right) \tag{46}$$

Here $f(y^+)$ is the self-similar velocity profile near the wall, which is given by the Law of The Wall.

In Ansys Fluent, there are two main types of wall functions, the standard wall function and the enhanced wall function. The standard wall function approximates the Law of The Wall by shifting between the linear model in the viscous sub-layer and the logarithmic model in the logarithmic region. You can find the equation for this in (47).

$$f(y^+) = \begin{cases} y^+ & y^+ < 11.25 \\ \frac{1}{\kappa} log(E y^+) & y^+ > 11.25 \end{cases} \tag{47}$$

κ is the Von-Kármán constant and E is an empirical constant.

In Ansys Fluent there is the standard wall function described above, but there is also the scalable and non-equilibrium wall function. The non-equilibrium wall function is better suited for complex flows involving separation, reattachment and impingement. Scalable wall function limits the y^* value to $y^* = 11.225$ to avoid the deterioration of standard wall functions under grid refinement below $y^* < 11$ [21].

The enhanced wall function uses a continuous function, which blends the logarithmic region, buffer layer and viscous sublayer. The function is given in equation (48).

$$f(y^+) = e^{\Gamma} u^+_{lam} + e^{\frac{1}{\Gamma}} u^+_{turb} \quad , \quad \Gamma = \frac{-0.01(y^+)^4}{1 + 5y^+} \tag{48}$$

Here u^+_{lam} is the non-dimensional velocity profile in the viscous sub-layer and u^+_{turb} is the profile in the logarithmic region following the law of the wall. In Fluent there also exist an option called the pressure gradient effect for the enhanced wall treatment. This option changes u^+_{turb} such that it is dependent on the pressure gradient.

When comparing the self-similar velocity profiles shown in figure 6 and the modified viscosities depicted in figure 7, it becomes clear that the enhanced wall function produces fewer errors in the buffer layer than the standard wall function. Therefore, it is recommended to use the enhanced wall function in the buffer layer.

The $k - \omega$ models and Spallart-Allmaras model use the enhanced wall function as a default option in Fluent [21].

It is recommended to use the following wall functions for the given y^+ values [21].

When $y^+ < 6$ and RANS is being used Guerreiro recommends resolving the boundary region, otherwise, he recommends using wall functions [31]. For LES it is recommended to have $y^+ < 1$ in order to resolve the boundary region [32].

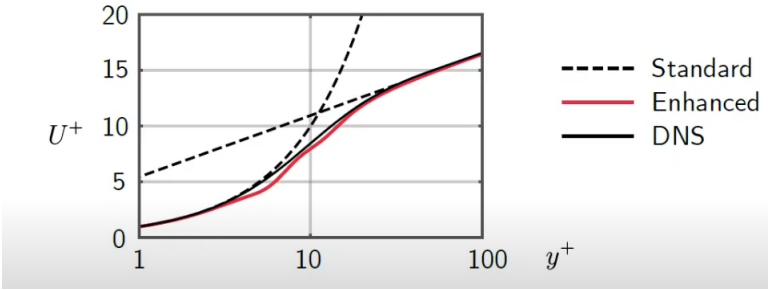

Figure 6: Comparisons of the wall functions velocity profiles

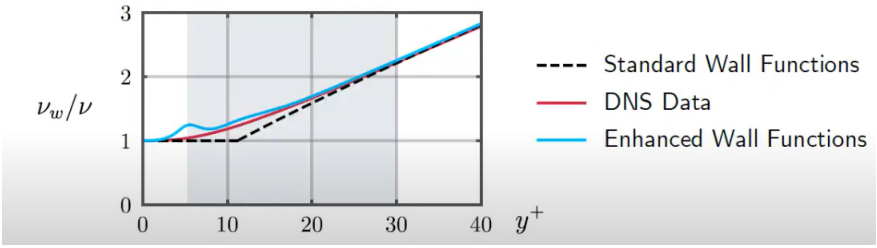

Figure 7: Comparisons of the modified viscosities

Table 1: Recommended y^+ values for the different wall treatments from Fluent theory guide [21].

	Range of Y-plus
Standard Wall Functions	$30 < Y^+ < 300$
Non-equilibrium Wall Functions	$30 < Y^+ < 300$
Scalable Wall Functions	$Y^+ > 11.225$
Enhanced Wall Treatment	$Y^+ < 5$

2.6.2 Free-stream boundary condition

Typically, the velocity is specified at the inlet, while the outlet is designated as a pressure outlet where the pressure is specified and the velocity has zero gradient. To calculate turbulent quantities, Versteeg [12] suggests utilizing equations (49), (50), and (51).

$$k = \frac{3}{2}(U_{ref}T_i)^2 \tag{49}$$

$$\epsilon = C_\mu^{3/4}\frac{k^{3/2}}{l} \tag{50}$$

$$\omega = C_\mu^{3/4}\frac{k^{1/2}}{l} \tag{51}$$

T_i is the turbulent intensity and l is the hydraulic diameter. For the Spalart-Allmaras model, Rumsey [33] suggests using $\nu_{farfield} = 3\nu_\infty$ to $\nu_{farfield} = 5\nu_\infty$. Here ν_∞ is the free-stream kinematic viscosity.

When using DES and LES, it is possible to include synthetic turbulence at the inlet to introduce fluctuating velocity components. Adding a boundary condition for the fluctuating velocity at the inlet is crucial for inlets where the flow is very turbulent. The reason why this is critical is that it predicts the correct amount of mixing in the flow. Additionally, this method can be used to simulate non-ideal perturbations during experiments. In Fluent, there are 3 different ways to

add this fluctuating velocity at the inlet. It is possible to use the Spectral synthesizer method proposed by Kraichmanc [34] and modified by Smirnov et al. [35]. In this method, fluctuating velocity components are computed by synthesizing a divergence-free velocity-vector field from the summation of Fourier harmonics. Another method is to use the Synthetic Turbulence Generator proposed by Shur et al. [36]. This method uses the RANS solution to calculate the fluctuating velocity component based on Fourier modes. Lastly, the vortex method can be applied as described in [21]. In this method a number of vortices normal to the streamline create the perturbations of the velocity, this means that the user needs to choose the number of vortices. Gerasimov suggests setting the number of vortices to N/4, where N is the number of nodes at the inlet [37].

2.7 Discretization schemes

The main concept of CFD is to discretize the continuous physics in spatial coordinates and for unsteady cases in time. The partial derivatives in the governing equations described in section 2.1 are discretized. Various spatial discretization schemes are widely used in CFD, some of which are discussed below.

- First Order upwind scheme
  - Gives good stability, but it is also very diffusive. So it is often not used in practice.
- Second Order upwind scheme
  - Gives good stability, and it is also not as diffusive as the first-order upwind scheme. It is, therefore often used for the convective terms of the Navier-Stokes equation and other turbulence transport equation terms in RANS. It is, however too dissipative for the convective term of LES.
- Central differencing
  - Can get problem with the stability using this scheme. However, it is second-order accurate and is often used for the diffusive terms of the Navier-Stokes equation and the pressure term. It is also used for the convective term in LES.

Two commonly used methods for discretizing time derivatives are explicit and implicit discretization. When using explicit discretization, new values are calculated based on old values. However, this approach can result in numerical instability issues, particularly if the physical distance covered during a time step exceeds the cell size. The Courant-Friedrichs–Lewy (CFL) number, defined in equation (52), describes the ratio between the distance covered after a timestep with the grid size. For instance, the simulation becomes unstable if the CFL number exceeds 1 when using the upwind scheme. Therefore, the timestep must be adjusted to ensure the Courant number is below 1 for the entire domain, allowing the upwind scheme to be used safely.

$$CFL = \frac{u\Delta t}{\Delta x} \tag{52}$$

For the implicit time discretization, the new values are calculated as a function of the neighbouring new values. Hence the implicit discretization leads to a system of equations that needs to be solved for each iteration. However, the implicit method is unconditionally stable, so using this scheme will never lead to instability, but it may lead to oscillating results if the timestep is too large.

2.8 Pressure-velocity coupling

For the incompressible Navier-Stokes equations, there are four equations (1-4) including the continuity equation for the velocity components. However, there is no direct equation for the pressure. This results in the pressure needing to be coupled with the velocity when solving the Navier-Stokes

equations. This can be implemented in many methods, such as the Semi Implicit Method for Pressure Linked Equations (SIMPLE)-, Pressure Implicit with Splitting of Operators (PISO)- and the PIMPLE algorithm. The SIMPLE algorithm was originally made for steady flows, and the PISO algorithm was made for transient flow problems. However, these algorithms have been modified to be applied to many flow configurations. The PIMPLE algorithm is mainly used for transient flows. It combines the PISO and SIMPLE algorithms, executing the SIMPLE algorithm for each time step until convergence is achieved. However, the PIMPLE algorithm is not available in Fluent. In addition, the SIMPLEC and SIMPLER algorithms exist, similar to the SIMPLE algorithm.

In most of the simulations in this report, the SIMPLE algorithm is used except for the URANS simulations. This algorithm is recommended for steady simulations [38]. It is shown in the article from Montazeri [39], that the SIMPLE algorithm can be advantageous for LES simulations as this gives better stability which means that the time step can be increased.

Below is the SIMPLE algorithm proposed by Patankar and Spalding [40]:

1. Guess the intermediate pressure field p^*.
2. Solve the momentum equations to obtain the intermediate velocities u^*, v^* and w^*, based on p^*.
3. Use these intermediate velocities to solve the new pressure corrector p'.
4. Use the pressure corrector p' to calculate the velocities correctors u', v' and w'.
5. Correct the velocities and pressure.

   $$u_i = u_i^* + u_i' \quad , \quad p = p^* + p'$$

   Now the velocities satisfy the continuity (1), but not the momentum equations. (2-4).
6. Solve for the other quantities.
7. Check for convergence. If converged, exit. If not, go back to step 2.

3 Literature review

The literature review of this thesis is taken from the specialization project of Bjuri [11], with slight modifications to fit the scope of this thesis better.

3.1 Fully turbulent flow benchmark

3.1.1 Experimental setup

Figure 8 illustrates the geometry of the fully turbulent benchmark, also referred to as "IEA Annex 20". The opening with height h represents the inlet, while the opening with height t represents the outlet. Nielsen conducted the experiments, as documented in [16].

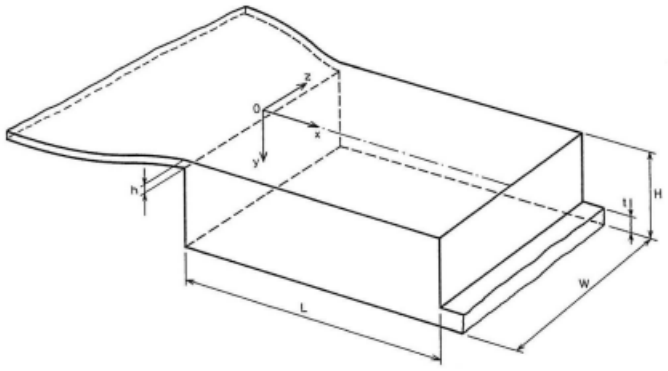

Figure 8: The geometry of the fully turbulent benchmark, figure taken from Nielsen [16]

The specifications for the geometry are as follows: H=3.0, L=9.0, h=0.168, and t=0.48 meters. The supply opening is relatively large compared to practical openings. The Reynolds number is 5000, based on the height of the inlet and the inlet velocity, which is 0.455 m/s. At this velocity, Nielsen [16] observed that the flow was fully turbulent. The kinematic viscosity was $\nu = 15.3 \cdot 10^{-6} m^2/s$, and the inlet temperature was measured to be 20°C. The turbulence intensity was measured at 4%. Using equations (49) and (50), with l=h/10, the inlet turbulent kinetic energy was $4.97 \cdot 10^{-4} m^2/s^2$, and the inlet dissipation rate was $6.59 \cdot 10^{-4} m^2/s^3$.

Measurements were taken at x=H, x=2H, y=h/2, and y=H-h/2, as shown in figure 9. The measurements included mean and Root Mean Square (RMS) values of the u-velocities, as well as the turbulence intensity u_{RMS}/u_0 at the inlet of the cavity. Laser-doppler anemometry was used for these measurements as it is suitable for velocity measurements of recirculating flow [16]. The measurements are available in the report by Nielsen [16].

Figure 9: The four different measurement lines for the experiments, figure taken from Dreau et al. [41]

For the experiment, Nielsen [16] also looked at the non-isothermal case, for different Archimedes

numbers, by sending a heat flux through the floor. The Archimedes number is the ratio between the gravitational and viscous forces and is used to determine the motion of fluids due to density differences. The Archimedes number is given by (53).

$$Ar = \frac{g \cdot \beta \cdot h \cdot \Delta T_0}{(u_0)^2} \tag{53}$$

g, β, ΔT_0 and u_0 are the gravitational acceleration, volume expansion coefficient, temperature difference between return and supply, and inlet velocity respectively. However, the measurements showed that changing the Archimedes number had little effect on the results [16].

3.1.2 CFD simulations

Simulations by Nielsen (2008)

Numerous CFD simulations have been conducted on this flow configuration, with various turbulence models being tested. In a report authored by Rong and Nielsen [42], the benchmark was simulated in 2D using different turbulence models. Figure 10 depicts the streamlines obtained from the various turbulence models. It was observed that the standard k-ϵ model only predicts a single recirculation zone. In contrast, the standard k-ω and BSL k-ω predict two additional recirculation zones at the upper right and lower left corners. The SST $k-\omega$, on the other hand, predicts a total of four recirculation zones.

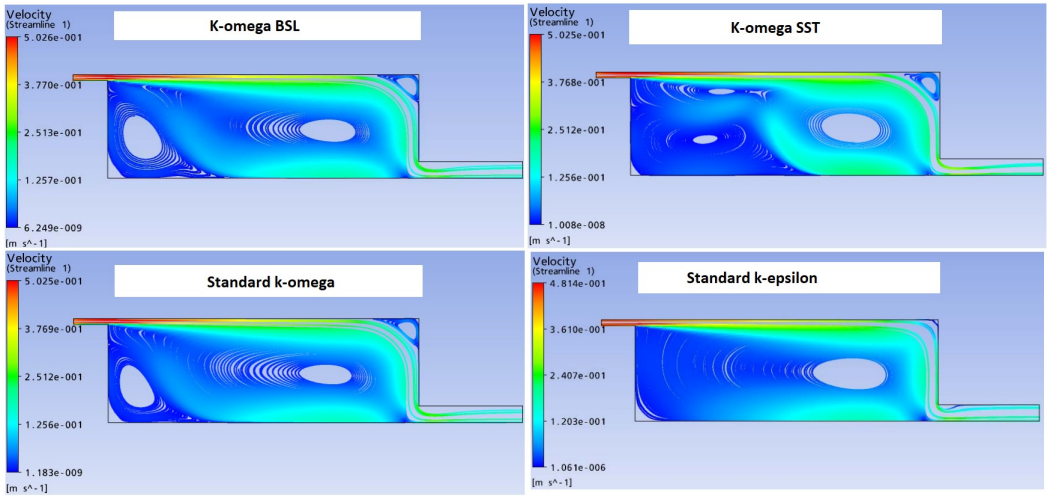

Figure 10: Streamlines from different turbulence models, figure taken from Rong and Nielsen [42].

In the same report, the velocity profiles of each turbulence model have been compared with the experimental data. The simulations agreed quite well with the measurements for the standard k-ϵ model, standard k-ω model and the BSL $k-\omega$ model. The standard k-ϵ method gave the overall best result while the SST model gave the worst results. However, none of the turbulence models managed to predict the velocity magnitude of the secondary vortex of the upper right corner [42].

Simulations by Olmedo and Nielsen (2010)

A study conducted by Olmedo and Nielsen [43] aimed to determine whether the flow was 2D or 3D, and if it was steady or unsteady. The simulations were performed using Ansys Fluent, with a mesh of 3 586 cells for the 2D case and 215 160 cells for the 3D case. The standard $k-\epsilon$ turbulence model was used for the simulations.

The result gave the following velocity profiles as seen in figures 11 and 12. In these plots y=0 is the floor of the cavity. The study concluded that the difference between steady and unsteady simulations was negligible, and the difference between 2D and 3D was minor. This was also

confirmed by the velocity contour plots and streamlines, which showed minimal changes between the different cases. The kinetic energy plots were also investigated, for these plots only a remarkable difference was observed between 2D and 3D simulations. Hence the report concluded that this flow could be characterized as a steady two-dimensional case [43].

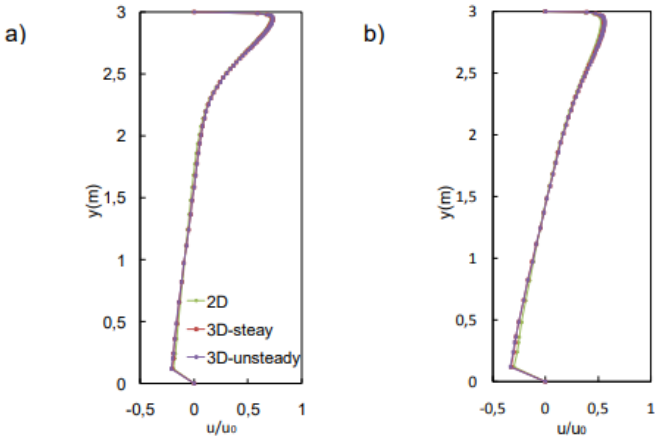

Figure 11: Non-dimensional vertical velocity profiles for 2D, 3D steady and 3D unsteady cases. a) velocity profile at the vertical line x=H. b) velocity profile at the vertical line x=2H. The figure is taken from Olmedo and Nielsen [43].

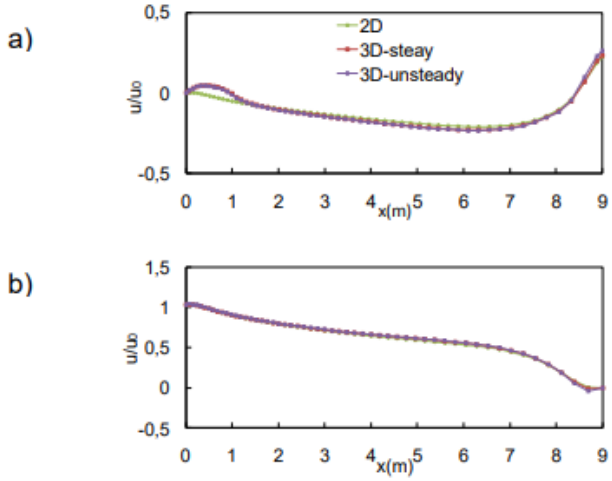

Figure 12: Non-dimensional horizontal velocity profiles for 2D, 3D steady and 3D unsteady cases. a) velocity profile at the horizontal line by floor. b) velocity profile at the horizontal line by the ceiling. The figure is taken from Olmedo and Nielsen [43].

Simulations by Bjerkeli (2020)

In Vegard Bjerkeli's master thesis [1], various RANS turbulence models were investigated in 3D using a wall-refined mesh of 342k cells. This mesh size provided satisfactory results from the grid sensitivity analysis. The study tested five turbulence models, namely the standard k-ϵ, RNG k-ϵ, realizable k-ϵ, AKN low-Re k-ϵ, and SST k-ω, all with enhanced wall treatment due to the wall-refined mesh. The SIMPLE algorithm was utilized to couple the velocity and pressure. For turbulence models with oscillatory convergence, the study performed an averaging over 9000 iterations for RNG k-ϵ, 10,000 iterations for SST k-ω, and 6000 iterations for realizable k-ϵ.

The results, depicted in Figure 13, illustrate that none of the turbulence models could fully describe the flow field compared to the experiments. At the floor's horizontal line z=h/2, near the inlet wall,

standard k-ϵ and SST $k-\omega$ predict positive u velocity, while realizable and RNG predict negative flow velocity. This suggests that different turbulence models exhibit different flow patterns. Root-Mean-Square Error (RMSE) analysis as shown in table 2 concluded that the standard k-ϵ was the best model; however, none were fully capable of modelling the entire flow field.

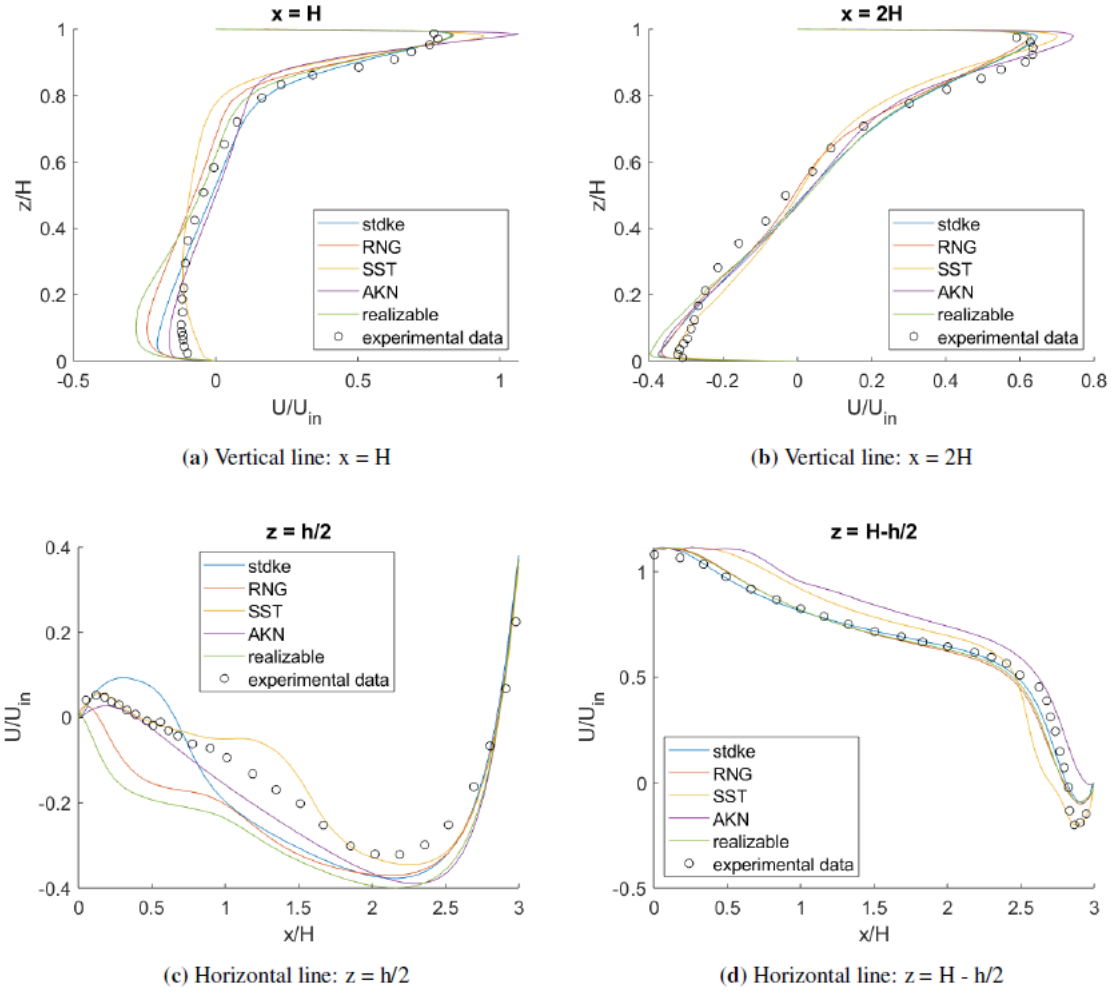

(a) Vertical line: x = H

(b) Vertical line: x = 2H

(c) Horizontal line: z = h/2

(d) Horizontal line: z = H - h/2

Figure 13: Comparing the following turbulence models for the fully turbulent benchmark: standard k-ϵ (stdke), RNG k-ϵ, SST k-ω, AKN-low-Re, realizable k-ϵ [1].

Table 2: RMSE values obtained by Bjerkeli [1] for the various RANS models on the fully turbulent case.

	x=H	x=2H	z=h/2	z=H-h/2	Average
stdke	0.055	0.045	0.071	0.059	0.057
RNG	0.089	0.045	0.100	0.081	0.079
SST	0.098	0.061	0.036	0.151	0.086
AKN	0.103	0.057	0.055	0.140	0.089
realizable	0.102	0.054	0.136	0.077	0.092

Different wall treatments were also investigated for this benchmark in Bjerkeli's master thesis [1]. The wall treatment options Enhanced wall treatment, standard wall function, non-equilibrium wall function and scalable wall function were tested in Fluent using the standard k-ϵ model. For the wall function, the mesh was created such that the y^+ values were above 30, giving a coarser mesh consisting of 108 thousand cells. This resulted in the following plots as shown in figure 14. It can

be observed that the enhanced wall treatment gave the best results at the ceiling of the cavity. However, it performed worse near the cavity floor, where none of the wall treatments provided satisfactory results. Through RMSE analysis, it was determined that the enhanced wall treatment yielded the best overall results.

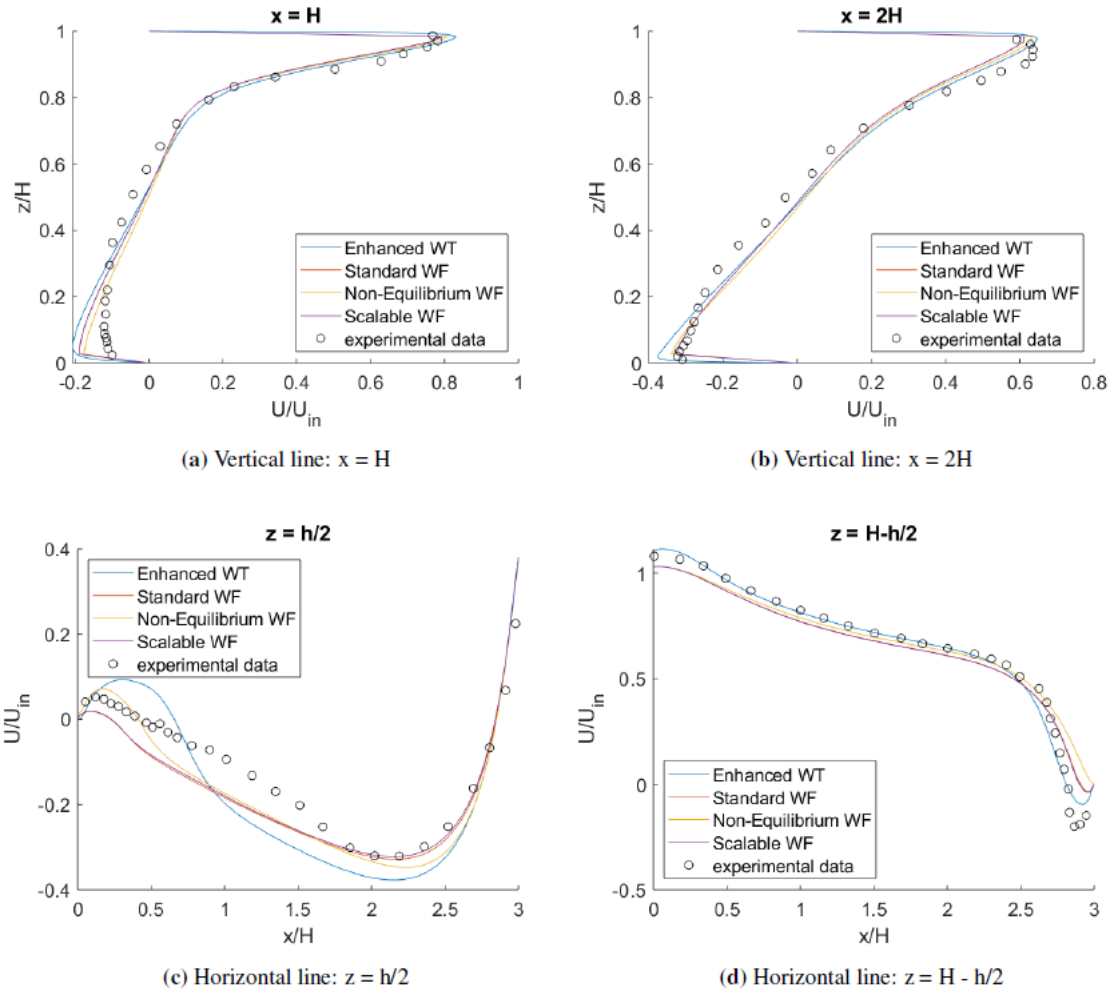

(a) Vertical line: x = H

(b) Vertical line: x = 2H

(c) Horizontal line: z = h/2

(d) Horizontal line: z = H - h/2

Figure 14: Results from different wall treatments of the fully turbulent case, the figure is taken from Bjerkeli [1].

Lastly, an investigation of the effect of the turbulence intensity at the inlet was conducted in the thesis. The turbulence intensities that were tested out were TI=4%, TI=20% and TI=50%. However, the results suggested that turbulence intensity had minimal to no effect.

Simulations by Taghinia et al. (2015) and (2016)

From the report [44] the SGS model RAST [45] and the hybrid RANS-LES approach SST-SAS were used on the fully turbulent benchmark. SST-SAS is an alternative to the DES model, where the grid spacing does not influence the RANS model. The k-ω SST model is the RANS model used, and it is modified by adding a source term to the transport equation of ω to account for unsteadiness. The model uses the PISO algorithm and a second order Crank–Nicolson for the time discretization. The mesh is refined so that the y^+ values are below 1, which is recommended when using LES [32]. This results in the mesh consisting of 2 016 000 cells. The geometry of this study only includes the cavity and the outlet section for numerical stability. It does not include the inlet section. A separate LES solution of a periodic channel flow with a length of 10*h is used as a boundary condition for the inlet section. The dimensionless time step $\Delta t U_{in}/h_{in} = 0.001$ was used, and the averaging was done over 1000 time steps after reaching statistical steady state. The

conclusion was that both modelling approaches gave an accurate flow prediction. However, the RAST model better agreed with the experimental data, as seen in figure 15.

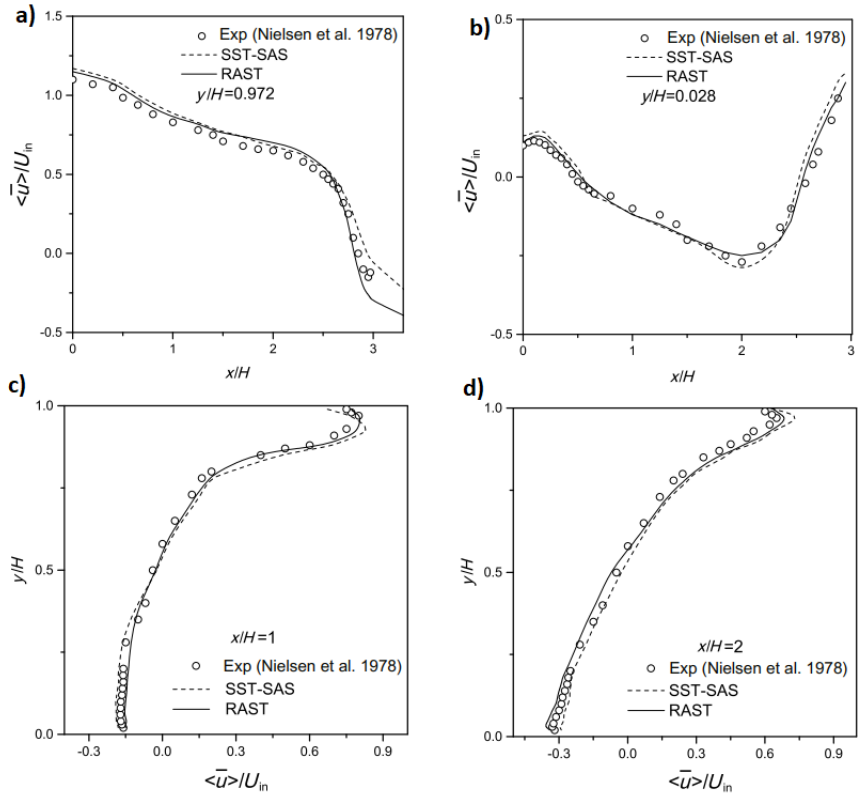

Figure 15: Velocity profiles of the turbulent case using RAST and SST-SAS model. a) velocity along a horizontal ceiling line. b) velocity along a horizontal floor line. c) velocity along the vertical line (x=H). d) velocity along the vertical line (x=2H). The figure taken from Taghina [44].

Simulations by Zasimova et.al. (2020)

The study conducted by Zasimova et al. utilized the WMLES S-Omega approach on Fluent to analyze the fully turbulent case [3]. The simulation consisted of approximately 48 million cells with a timestep of 0.001s, resulting in a Courant number less than 1. Spatially, second-order discretization schemes were employed, while the non-iterative algorithm (NITA) with second-order accuracy was utilized for temporal discretization. The Reynolds number of the flow was 5223 instead of the reported value of 5000 from Nielsen [16].The simulation geometry considered only the cavity and outlet duct to avoid backflow. For the inlet, a separate WMLES was conducted on a channel flow having the same geometry as the inlet duct and a length of 2H (6 meters). To create turbulent structures in the inlet, the vortex method was used to generate velocity disturbances, but the number of vortices used was not specified. The averaging commenced when the flow reached statistical steady state, and the flow properties were sampled over 1500-3000 seconds. The velocity at specific points was monitored to determine when the flow was in statistical steady state. The origin of the coordinate system is the corner at the floor by the inlet, and the ceiling of the cavity is located at y=3.0 meters.

According to the study, the cavity flow was divided into two areas: the jet flow zone near the ceiling and the occupant zone, which had lower velocities than the jet flow zone. Figure 16 showed that the WMLES accurately modelled the jet flow zone near the ceiling but had poor results for the occupant zone near the floor. Figure 17 displayed the contour plot of the averaged velocity magnitude at the mid-xy-plane, where the effects from walls in the transverse direction were ignored due to the use of symmetric boundary conditions. However, this had a negligible effect on the contour plot.

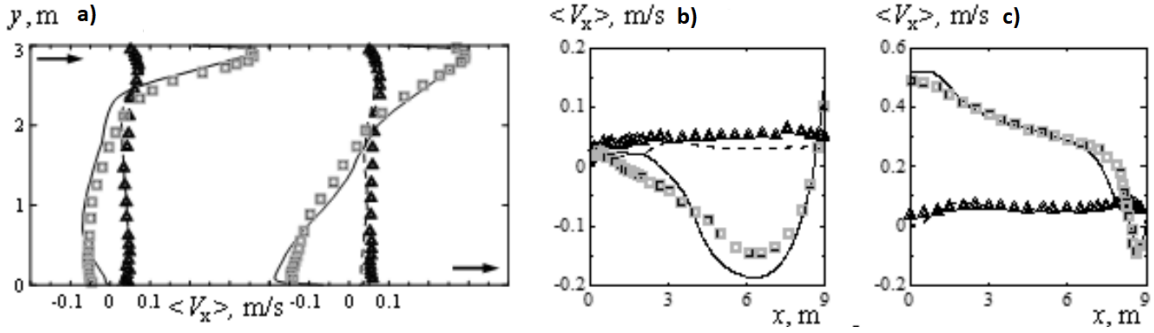

Figure 16: Velocity profiles from the WMLES simulation, squares are the measured velocities, triangles are the measured RMS value of the velocity, the line is the mean velocity profile from the simulation and the dotted line is the RMS value of the velocity from the simulation. a): the left plot is the velocity plot at x=3m line, and the right plot is the velocity plot at x=6m line. b): velocity plots by the floor of the cavity. c): Velocity plot by the ceiling of the cavity. The figure is taken from Zasimova et al. [3]

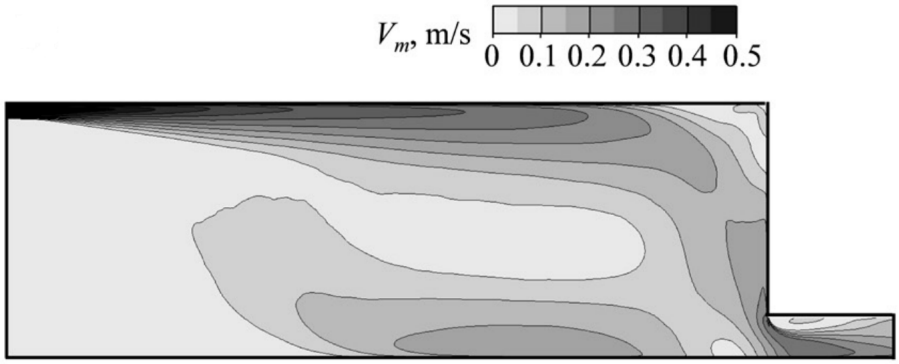

Figure 17: Mean velocity magnitude contour plot at the xy -midplane (z=1.5m) for symmetric boundary conditions in the tranverse direction. The figure is taken from Zasimova [3].

3.2 Transitional flow benchmark

3.2.1 Experimental setup

Van Hooff et al. conducted the transitional flow benchmark experiment as documented in [18]. The experimental data and setup can be found on [46] under the name "UFR 4-20 Test Case". The geometry of the experiment is illustrated in figure 18. Water flows from the water column into the test section via the conditioning section and exits through the outlet. The conditioning section was utilized to decrease turbulence intensity and accelerate flow through the contraction.

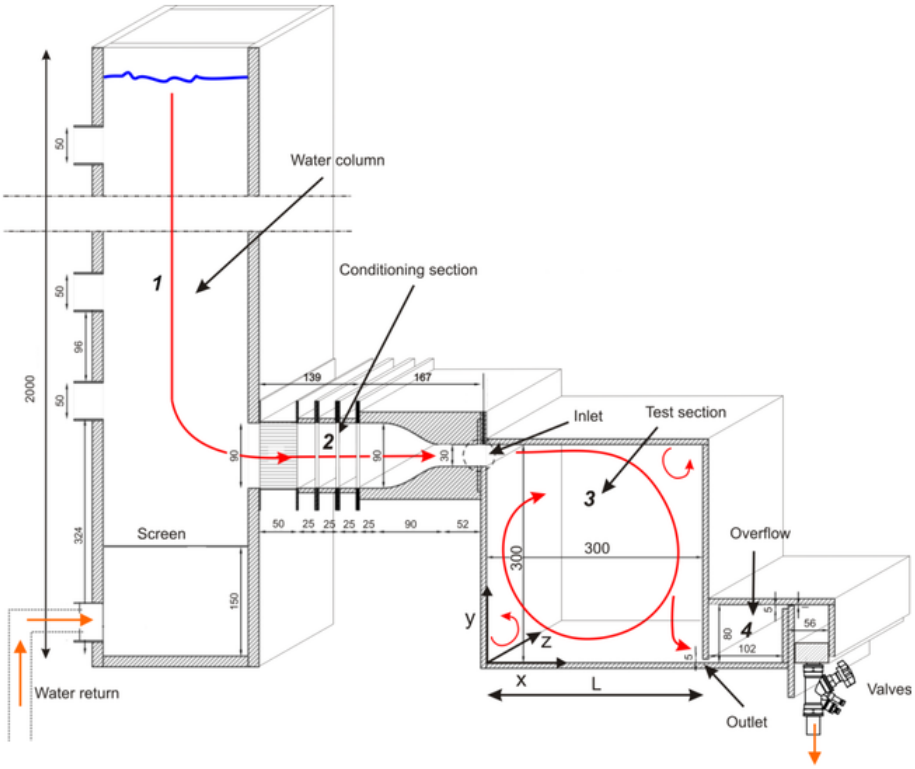

Figure 18: The experimental setup of the transitional flow benchmark, the figure is taken from Van Hooff et al. [18].

The contraction follows the fifth-order polynomial shown in equation (54).

$$h_g = \left((-10\xi^3 + 15\xi^4 - 6\xi^5)(H_i^{1/\alpha} - H_e^{1/\alpha} + H_i^{1/\alpha})\right)^{\alpha} \quad , \quad \xi = \frac{x}{L_c} \tag{54}$$

ξ is the normalized length of the contraction, h_g the normalized height of the contraction, L_c the length of the contraction, H_i and H_e are the y-coordinates of the contraction inlet and outlet. For this contraction the parameters have the following values: L_c=0.09m, H_e=0, H_i=0.03m and α=0.5.

On this geometry, two different flow configurations were tested. One flow configuration had a Reynolds number of 1000, while the other had a Reynolds number of 2500, but both led to a transitional regime. The temperature was measured at 20°C. The turbulence intensity at the wall jet region at x=0.2L was around 3-4% for both cases.

Figure 19 shows the geometry of the test section more clearly.

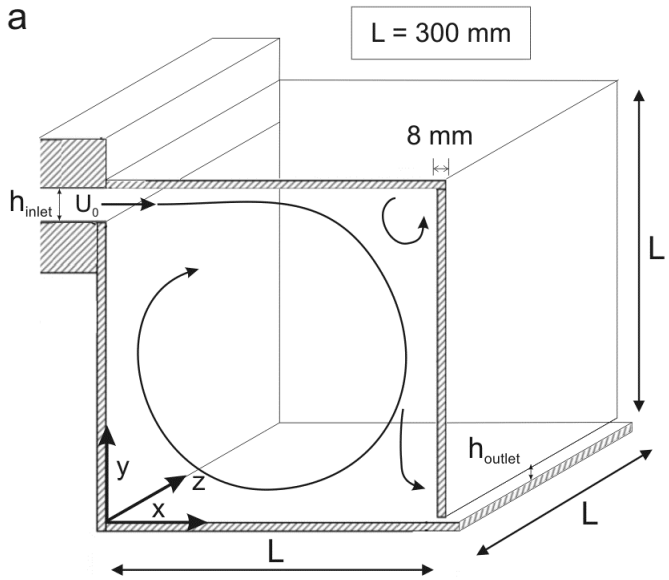

Figure 19: The test section of the transitional flow benchmark, the figure is taken from Van Hooff et al. [46].

For this benchmark, the geometry is cubical H=L=W=0.3, h=0.01 and t=0.00501 meter. Measurements were done using a 2D PIV system, measuring the velocity components in x- and y-directions. Two sets of PIV measurements were performed both in the xy-midplane. One measurement focused on the entire xy- midplane, while the other only measured the velocities near the inlet at an area of 0.18x0.12 m^2, to obtain a higher resolution near the inlet. The x-velocities were measured along the three vertical centre lines; x=0.2L, x=0.5L and x=0.8L, as seen in figure 20. The velocities were non-dimensionalized by dividing the velocity by the maximum velocity measured at that line. The turbulent kinetic energy where also determined for the PIV measurement near the inlet. The turbulent kinetic energy was determined from the measured u- and v velocity fluctuations, as seen in equation (56). Since the PIV measurements were done in 2D, the RMS value in the lateral direction was calculated by the Nielsen correlation [16] given in equation (55).

$$w_{RMS} = \sqrt{0.8} u_{RMS} \tag{55}$$

$$k = \frac{1}{2}(u_{RMS}^2 + v_{RMS}^2 + w_{RMS}^2) \tag{56}$$

The uncertainty of the measurements was found to be around 2-4% in the largest part of the test section, and higher in the shear layer and boundary layer areas due to higher turbulence levels [18]. Additionally, the measurements taken near the inlet floor had greater uncertainty because of the reflection of the laser sheet from the glass floor.

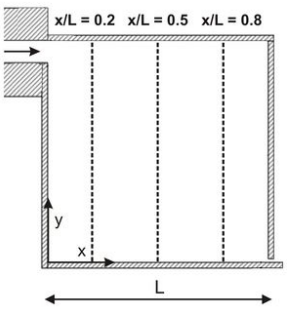

Figure 20: PIV measurements of the transitional flow benchmark, the figure is taken from Van Hooff et al. [46].

3.2.2 CFD simulations

Simulations by Van Hooff et al. (2013)

In the same web page [46] that describes the experimental setup, the authors also conducted CFD simulations both for Re=1000 and Re=2500. These simulations included the extraction area, and the outlet was extended in the x-direction to improve stability. The turbulence intensity was set to 6% for the Re=1000 case and 18% for Re=2500. A grid sensitivity analysis was performed, and a mesh consisting of 3,437,056 cells was used to ensure y^* values were significantly lower than 1. The y^* values were used instead of y^+ values, since y^+ will go to zero in regions where the flow is re-attaching or impinging. In these simulations, three different turbulence models were tested out. These models were Low-Reynolds k-ϵ, SST $k-\omega$ model and the Reynolds stress model. The SIMPLEC velocity-pressure coupling scheme was employed.

Figure 24 illustrates the velocity profiles for the inlet duct Reynolds number of 1000. Because of inaccuracy in the PIV measurements near the floor (y/L)=0.05 values below this area are not included. The predictions of all models for the velocity profile at the lines x/L=0.2 and x/L=0.5 are quite good. However, at the line x/L=0.8, the SST and Reynolds stress models predict the maximum velocity at the wrong y value, while the low-Re $k-\epsilon$ model predicts the velocity profile quite accurately.

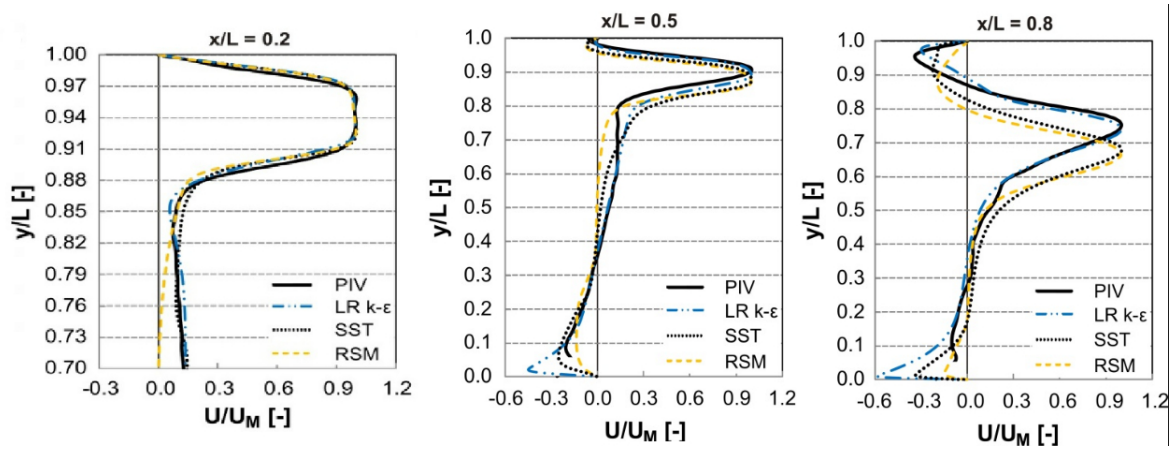

Figure 21: Velocity profiles for Re=1000 for the turbulence models: Low-Re k-ϵ, k-ω SST and Reynolds stress model, the figure is taken from Van Hooff et al. [46].

The vector velocity plots at the xy-midplane (z=0) of the different turbulence models were also investigated and compared to those obtained by the PIV measurement. The vector velocity plot for the case Re=1000 is shown in figure 22. The computed and measured center of the big recirculation vortex is also shown in this figure. The low-Re $k-\epsilon$ model predicts the deattacthment location the best, and it also predicts the center of the recirculation quite well.

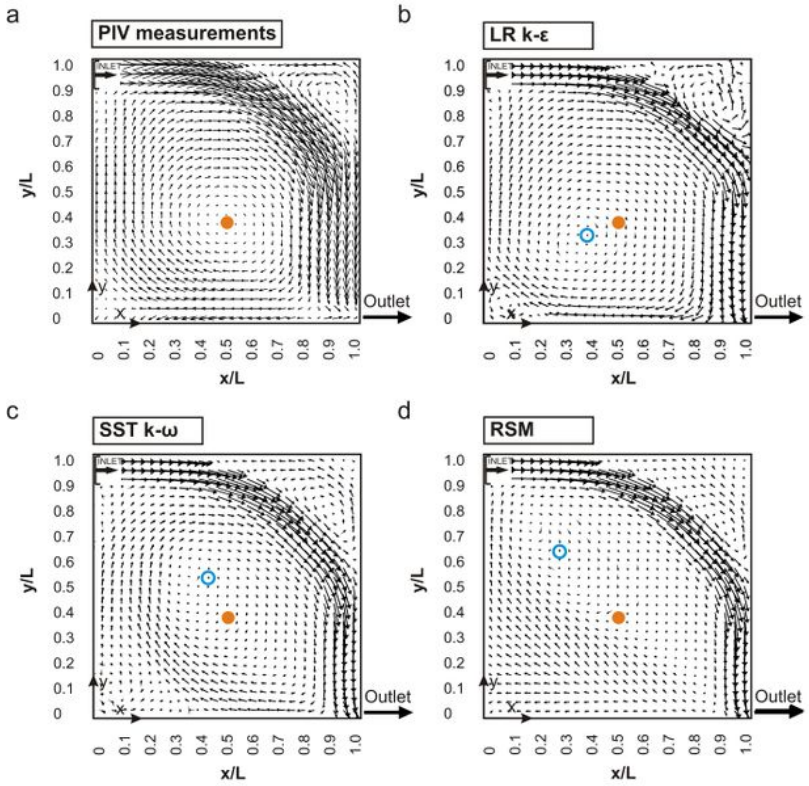

Figure 22: The vector velocity plots of the different turbulence models when Re=1000 compared to those obtained by the PIV measurement. The figure is taken from Van Hooff et al. [46].

The turbulent kinetic energy of the different turbulence models was also analyzed along the two vertical lines on the xy-midplane x/L=0.2 and x/L=0.5. This is shown in figure 23. None of the models managed to predict the turbulent kinetic energy well, and all of them under-predicted this value close to the wall. The reason for this is that none of the models are developed to model the transition from laminar to turbulent flow [46].

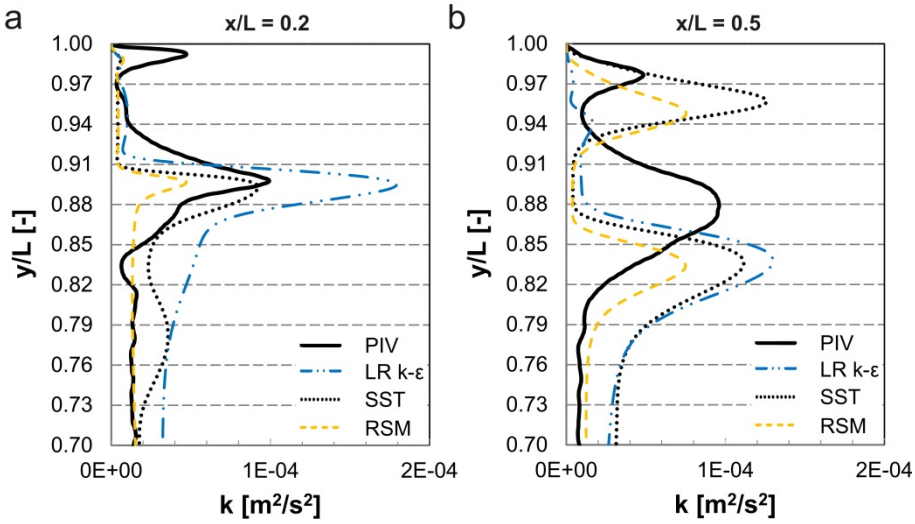

Figure 23: Turbulent kinetic energy plots for Re=1000 of the different turbulence models, the figure is taken from Van Hooff et al. [46].

Figure 24 shows the velocity plots for the Re=2500 case. Also for this case, the low-Re $k-\epsilon$ outperforms the other models. The other models predict the detachment point too early, which

is apparent in the vector velocity plot in figure 25. At higher Reynolds numbers, the detachment point is pushed further away from the inlet, and all turbulence models accurately capture this phenomenon. Additionally, the turbulence models are more effective at predicting the center of the large circulation vortex for this case than they are for the Re=1000 case.

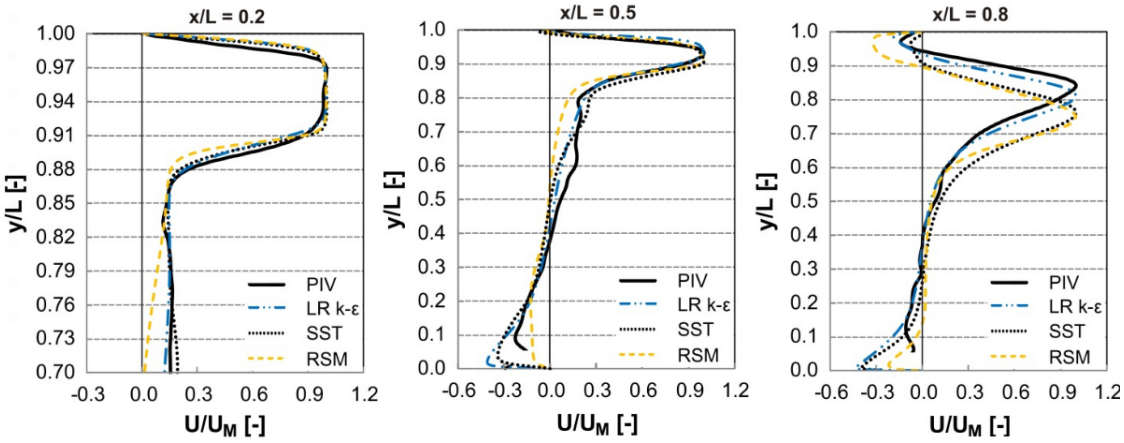

Figure 24: Velocity profiles for Re=2500 for the turbulence models: Low-Re k-ϵ, k-ω SST and Reynolds stress model, the figure is taken from Van Hooff et al.[46].

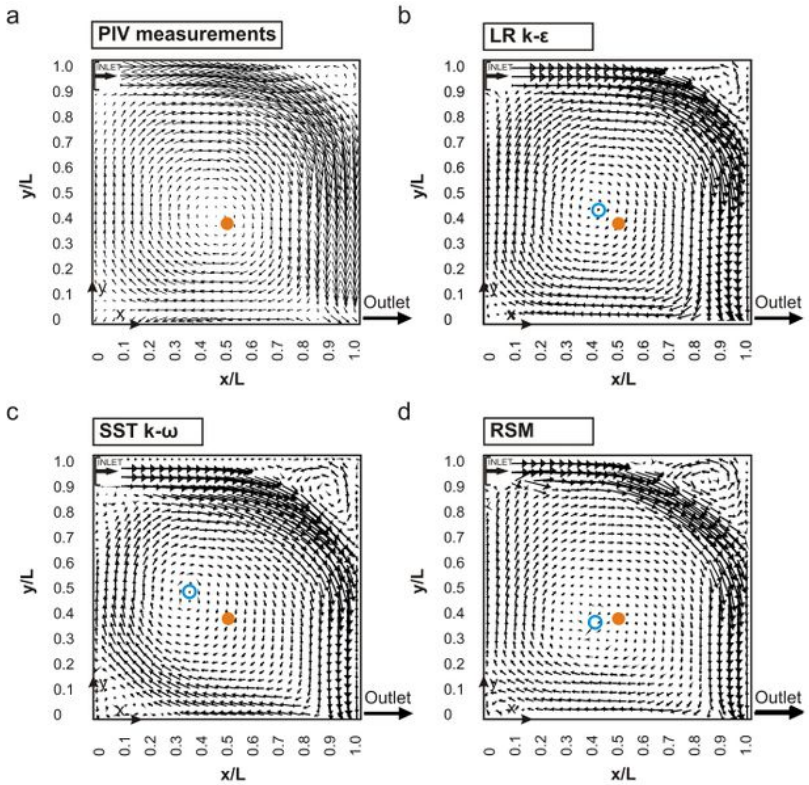

Figure 25: Vector velocity plots at the xy-midplane for the case Re=2500. The figure is taken from Van Hooff et al. [46].

Figure 26 shows the turbulent kinetic energy for the Re=2500 case. Also for this case none of the tested turbulence models manage to predict the turbulent kinetic energy with good accuracy. At x/L=0.2, all models underestimate the turbulent kinetic energy in the boundary layer, while the Low Re k-ϵ model significantly overestimates it at y/L=0.9. At the x/L=0.5 line, the turbulence models behave differently, and none of them predict the turbulent kinetic energy well.

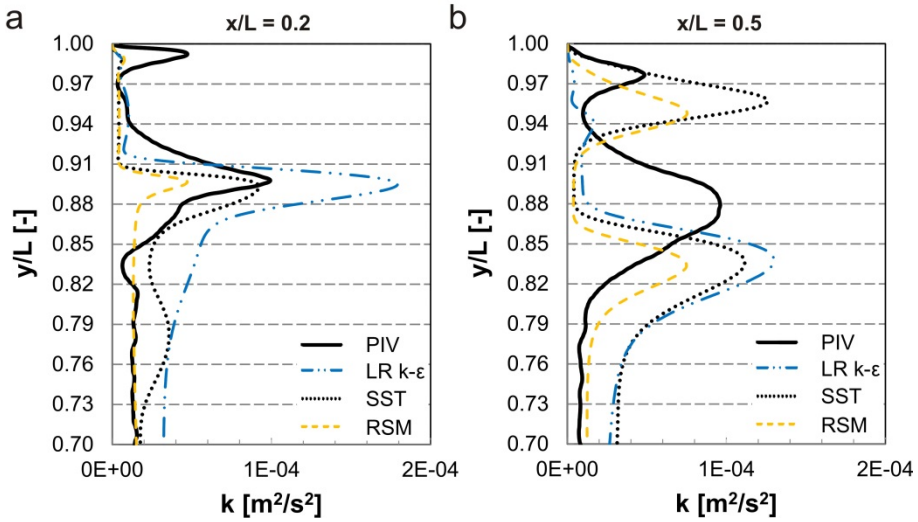

Figure 26: The turbulent kinetic energy of the case Re=2500 at the two vertical lines a): x/L=0.2, b): x/L=0.5. The figure is taken from Van Hooff et al. [46].

Simulations by Bjerkeli (2020)

In Bjerkeli's master thesis [1] the benchmark was simulated, with OpenFoam for a Reynolds number of 1000. A grid sensitivity analysis was conducted, resulting in a mesh consisting of 1.2 million cells being used, which was refined near all the walls except for the front and back walls. Four different turbulence models, namely the standard k-ϵ, SST $k-\omega$, realizable $k-\epsilon$, and RNG $k-\epsilon$, were tested, with all models exhibiting oscillating residuals and being averaged over 2000 iterations. The SIMPLE algorithm was utilized to couple the velocity and pressure.

Figure 27 illustrates the velocity profiles of the various models, with the inlet velocity being used for non-dimensionalization instead of the local maximum velocity at that line, as used by Van Hooff et al. [46]. The SST $k-\omega$ model predicts detachment accurately, while the other model predicts it further away from the inlet. However, it was observed that all models overpredict the maximum velocity of the jet. Overall, the SST $k-\omega$ turbulence model was deemed the best model, while the standard k-ϵ model was the worst model as can be shown in table 3, showing the RMSE values of the different RANS models.

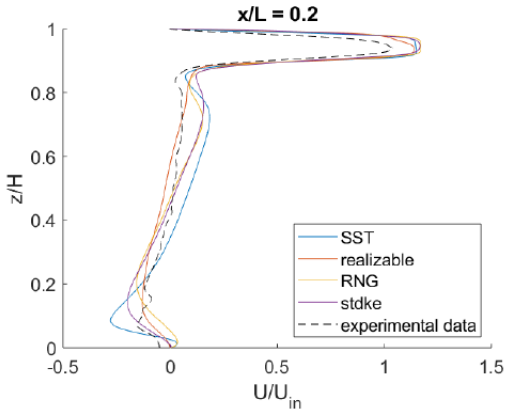

(a) Vertical line: x = 0.3L

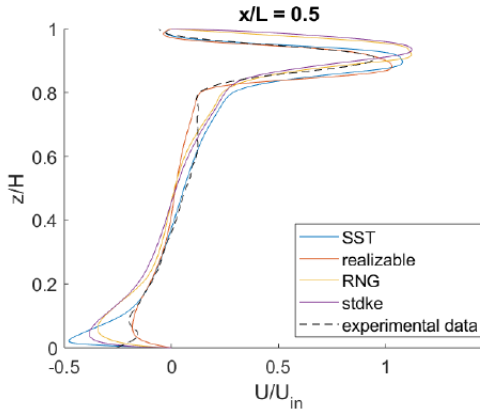

(b) Vertical line: x = 0.5L

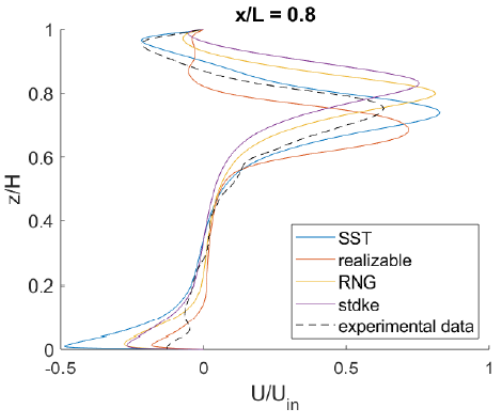

(c) Vertical line: x = 0.8L

Figure 27: The velocity profiles obtained by Bjerkeli for the transitional case with a Reynolds number of 1000, using the turbulence models SST, RNG, Realizable and standard k-ϵ [1].

Table 3: RMSE values obtained by Bjerkeli [1] from the RANS simulation of the transitional case with a Reynolds number of 1000.

	x/L=0.2	x/L=0.5	x/L=0.8	Average
SST	0.112	0.088	0.077	0.092
Realizable	0.094	0.085	0.146	0.108
RNG	0.107	0.153	0.167	0.143
stdke	0.109	0.180	0.230	0.173

Simulations by Van Hooff et al. (2014)

Van Hooff et al. [4] has conducted a simulation of this benchmark for Re=2500 using RANS and LES. The RANS models utilized were the Low-Reynolds k-ϵ and the Reynold Stress Model (RSM), and they had the same discretization schemes as in the previous report by Van Hooff et al. [46]. For LES, the dynamic Smagorinsky-Lilly model was used as the SGS model. Based on a grid sensitivity analysis, a mesh consisting of 1 386 4000 cells was used, resulting in y^* being between 0.12 and 0.68. The PISO algorithm was used for velocity-pressure coupling, and the second-order implicit method was used for time discretization in LES. At the inlet, the vortex method with 180 vortices was used for LES to create fluctuating velocity. The flow quantities were averaged over 20 flow-through times, where one FTT was measured to be 20 seconds. The timestep used was 0.004 seconds, which resulted in a maximum CFL number of one.

Figure 28 compares the velocity measurements from PIV to the results of the different turbulence

models at x/L=0.2, x/L=0.5, and x/L=0.8. For x/L=0.2 and x/L=0.5, all the turbulence models predicted the velocity quite well and were similar. However, for x/L=0.8, the LES outperformed the other RANS models. The two RANS models seemed to predict the detachment point too early compared to the PIV measurements, while the LES predicted the detachment point quite accurately. Figure 29 depicts the comparison of the turbulent kinetic energy using the same method as [46]. None of the models are able to predict the turbulent kinetic energy well.

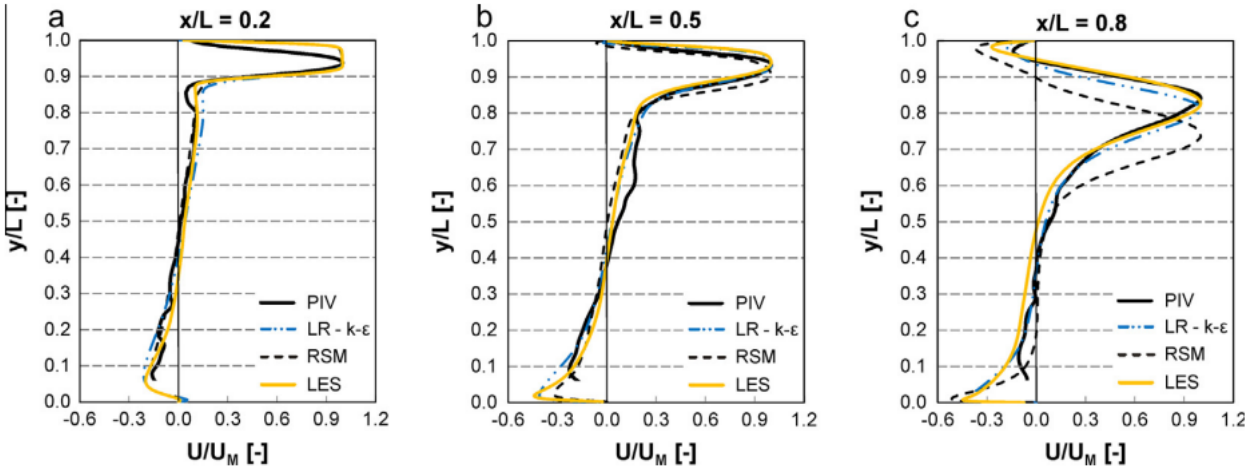

Figure 28: Velocity profiles from Van Hooff et al. [4]; left x/L=0.2; middle x/L=0.5; right x/L=0.8

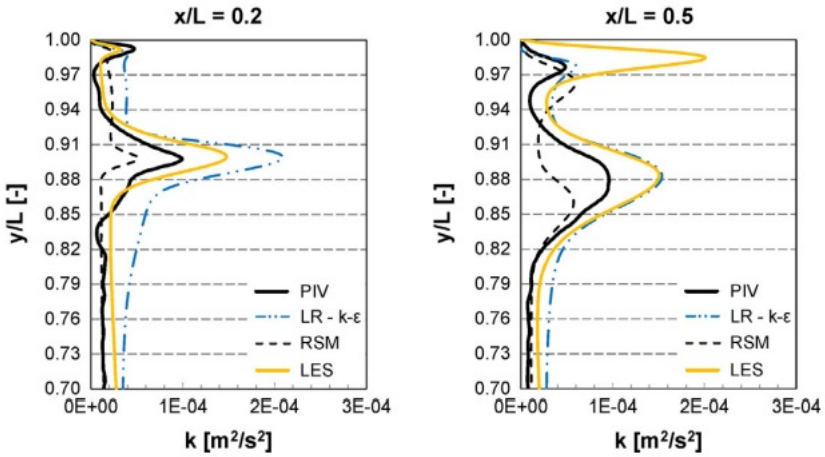

Figure 29: Turbulent kinetic energy profiles from Van Hooff et al. [4]; left x/L=0.2; right x/L=0.5.

3.3 Realism of the benchmarks

The benchmarks discussed in this thesis are significantly simplified in comparison to real-life ventilation scenarios. In actual ventilation cases, the geometries are often more complicated in both the cavity and ventilation duct. It is common to have multiple ventilation ducts that can interact with each other, along with various other sources and sinks for the airflow within the cavity, such as open windows, gaps in doorways, and human interaction with the air. Furthermore, temperature gradients within the room are not modeled, which may impact the flow field.

Scaling up the cavities from the benchmark to more realistic cavities with a ceiling of 2.4 meters, which is the minimum allowed ceiling height in Norway [47], and also scaling up the inlet velocity to keep the Reynolds number constant. This allows us to compare the flow rate from the benchmark

to the flow rate required by the Norwegian building standard TEK17. According to TEK17, a flow rate of 26 m^3 per hour per person is necessary to address air pollution from human activity, while a flow rate of 2.5 m^3 per hour per m^2 floor area is required to address air pollution from materials and products [47]. Sintef estimates that the occupant density has a value of 5 $m^2/pers$ [48]. Using these values the flow rate per area can be calculated using equation (57). This is similar to how Bjerkeli calculated the flow rate for the benchmarks he investigated [1].

$$\frac{Flowrate}{Floorarea} = (\frac{26}{5} + 2.5)m^3/(hm^2) = 7.7m^3/(hm^2) \tag{57}$$

Using this calculated value, it is possible to calculate the TEK17 standard for the airflow rate necessary for each scaled-up benchmark, by multiplying this with the floor area. The calculation of the flow rates of the scaled-up benchmarks are given in table 4.

Table 4: Calculated values for scaled-up benchmarks compared with the standard TEK17 [47] air flow rate.

	Fully turbulent case (Re=5000)	Transitional case (Re=1000)	Transitional case (Re=2500)
Height [m]	2.400	2.400	2.400
Width [m]	2.400	2.400	2.400
Length [m]	7.200	2.400	2.400
Floor area [m^2]	17.28	5.760	5.760
Ventilation duct height [m]	0.1344	0.2400	0.2400
Inlet velocity [m/s]	0.5692	0.06375	0.1594
Flow rate per hour [m^3/h]	661.0	132.2	330.5
TEK17 standard [m^3/h]	133.1	44.35	44.35

As shown in table 4, all benchmarks meet the minimum flow rate required by TEK17 standards. The fully turbulent case exceeds the TEK17 standard by a factor of 6, while the transitional cases exceed it by factors of 3 and 7.5 at Reynolds numbers of 1000 and 2500, respectively. It is important to note that the height of the ventilation duct greatly affects the flow rate. For these benchmarks, the inlet slot height is large compared to practical diffusers [16]. Additionally, practical ventilation ducts typically do not stretch the full width of the cavity like the benchmarks do, resulting in higher flow rates compared to real-world applications. Nevertheless, the flow regimes of practical ventilation systems are usually fully turbulent, transitional or both flow regimes are present at different areas of the cavity. Therefore, these benchmarks are useful for comparing different turbulence modelling approaches for practical ventilation scenarios.

4 Method

4.1 Software used

Geometry

The software DesignModeller was primarily used to create the geometry of the different benchmarks. However, for the transitional benchmark, SpaceClaim was also utilized to fix the edges of the contraction section. The geometry comprises numerous small boxes to provide greater control when creating the mesh, which makes it easier to refine the mesh at specific locations. In the fully turbulent case, the geometry consisted of 78 volumes, with the inlet and outlet containing 12 volumes each, and the cavity comprising 54 volumes. For the main cavity, 3 volumes were allocated for the z-direction, 3 for the x-direction, and 6 for the y-direction. Figure 30 shows the geometry of the fully turbulent case.

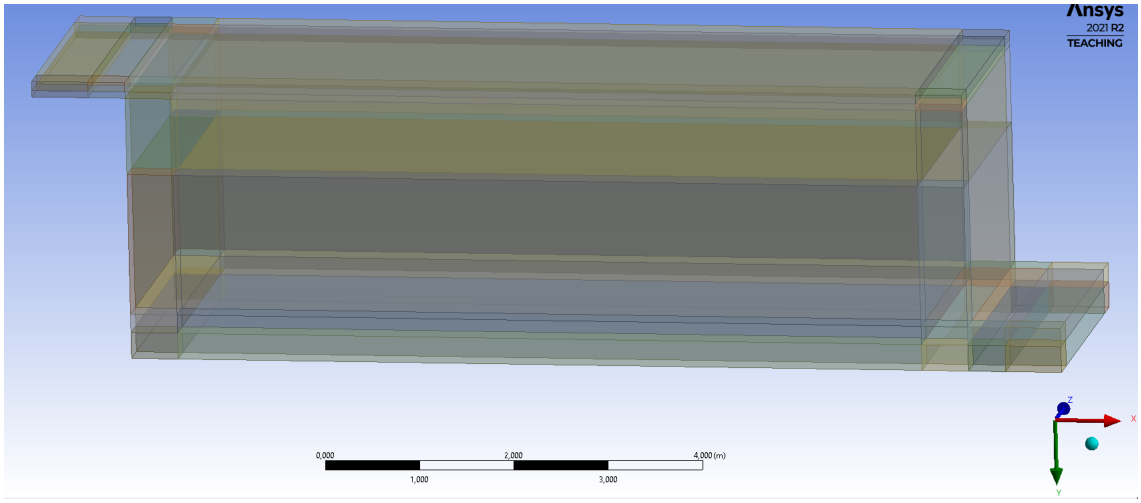

Figure 30: The geometry created of the fully turbulent case, showing the geometry in DesignModeller

For the transitional benchmark, the geometry consisted of 63 volumes, where the inlet consisted of 12 volumes, the outlet consisted of 6 volumes and the main cavity consisted of 45 volumes. For the main cavity, 5 volumes were used in the y-direction, and 3 volumes were used for the z-direction and x-direction. The contraction at the inlet was created by importing the geometry of the 2D contraction from a .txt file, and expanding the geometry in the z-direction. The geometry of the transitional benchmark can be seen in figure 31.

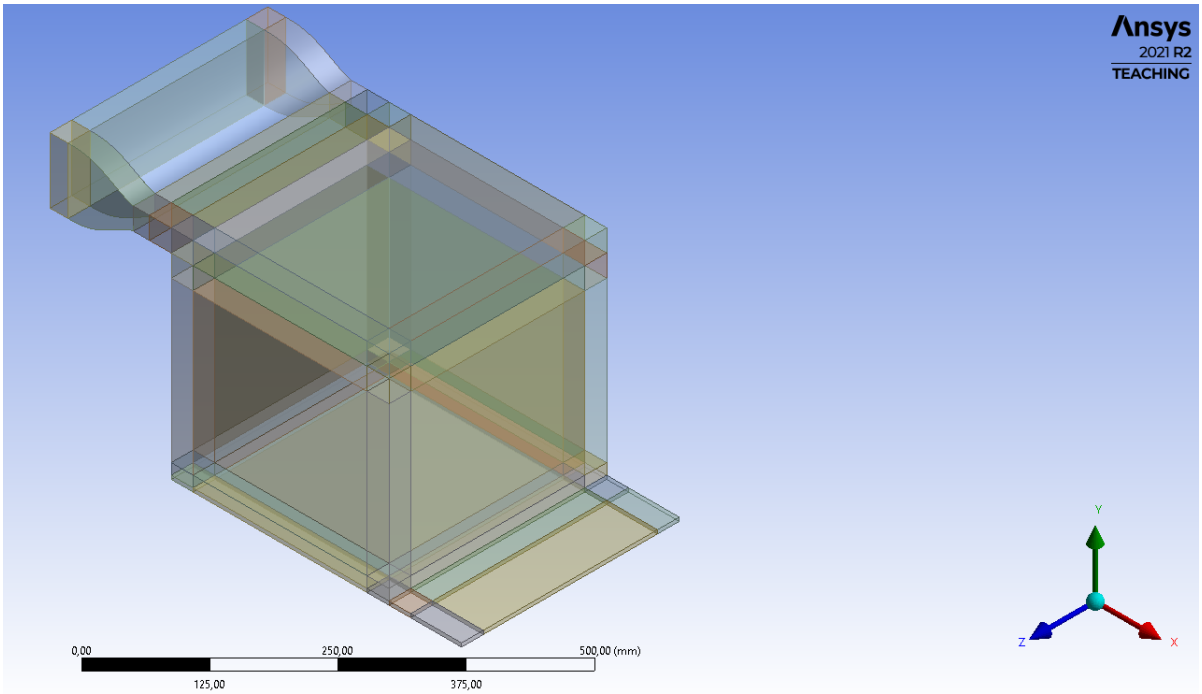

Figure 31: The geometry created of the transitional case, showing the geometry in DesignModeller.

Meshing

Ansys Meshing software was used to create the different meshes. The geometry was first imported into the meshing software, then the different volumes were defined as Multizones. The number of cells at every edge was defined, and the growth factor of the edges was defined such that the walls were refined enough. The mesh in the transition area between each volume was also investigated, such that a smooth transition was achieved. For the transitional case, special care was made in the contraction area, to avoid the simulation diverging because of the poor mesh in this area.

Simualtion software

For running the simulations the software Ansys Fluent version 2021 R2 was used. The mesh was imported into the Fluent software and then simulated. Parallelization was utilized to decrease the simulation time, and in order to run multiple cases at the same time. The current simulations were performed on the FRAM cluster provided by UNINETT Sigma2, the National Infrastructure for High-Performance Computing and Data Storage in Norway. In addition to the Fram cluster, the Idun cluster provided by NTNU was utilized for the parallelization. The Idun cluster "aims at providing a high-availability and professionally administrated compute platform for NTNU. It is an effort to combine the compute resources of individual shareholders to create a cluster for rapid testing and prototyping of HPC software." [49] The paragraph below describes the Fram cluster, and is taken from the documentation web page of the Fram cluster [50].

FRAM the new Linux cluster hosted at UiT Arctic University of Norway, is a shared resource for research computing capable of 1.1 PFLOP/s theoretical peak performance. Fram is a distributed memory system that consists of 1004 dual socket and 2 quad socket nodes, interconnected with a high-bandwidth, low-latency Infiniband network. The interconnect network is organized in an island topology, with 9216 cores in each island. Each standard compute node has two 16-core Intel Broadwell chips (2.1 GHz) and 64 GiB memory. In addition, 8 larger memory nodes with 512 GiB RAM and. The total number of compute cores is 32256.

Post-processing software

For post-processing the results the software CFD-POST, Ansys Fluent, MATLAB and Paraview were used.

To compare different simulations with experimental data, the statistical measurement Root Mean Square Error (RMSE) is commonly used. This quantity estimates the average error in the results and is useful for comparing errors as long as the results are in the same order of magnitude. Since the results are non-dimensional, obtained by dividing by the inlet velocity, the RMSE is a suitable metric for comparing results. The equation for RMSE is shown in (58), where P_i represents the predicted value from the simulation, O_i represents the experimental value, and N is the sample size of the experimental data.

$$RMSE = \sqrt{\frac{\sum_{i=1}^{N}(P_i - O_i)^2}{N}} \tag{58}$$

4.2 Simulation setups

The setups of the simulation are identical to the ones used in the specialization project of Bjuri [11]. The simulation setup on Fluent is summarized in table 5 for the RANS/URANS simulations and table 6 for the DES simulation. The URANS simulation setups are the same as the RANS. The only difference is that the time was discretized using the second-order implicit scheme, and that URANS uses the PISO algorithm, while the RANS uses the SIMPLE algorithm for decoupling the velocity and the pressure. RANS uses the SIMPLE algorithm since this is recommended for steady simulations and URANS uses PISO as this is recommended for unsteady simulations.

Table 5: RANS/URANS simulation setup

RANS/URANS simulation settings	
Pressure-velocity Flux type	Rhie-Chow: distance based
Gradient discretization	Least Squares Cell Based
Pressure discretization	Second Order
Momentum discretization	Second Order Upwind
Turbulence model discretization	Second Order Upwind

For the RANS/URANS, second-order methods were chosen to increase the accuracy of the simulation. The turbulence model discretization is how the turbulent quantities calculated by the additional transport equations are discretized. For the k-ϵ model, this means how the partial derivates of k and ϵ are discretized, while for the k-ω models, it is k and ω and for the Spalart-Allmaras it is the turbulent viscosity.

Table 6: DES simulation setup

DES simulation settings	
Pressure-velocity coupling	SIMPLE
Pressure-velocity Flux type	Rhie-Chow: distance based
Gradient discretization	Least Squares Cell Based
Pressure discretization	Second Order
Momentum discretization	Bounded Central Differencing
Turbulence model discretization	Second Order Upwind
Time discretization	Second Order Implicit

The settings given in table 6 are used for the DES simulation, as these are the default ones for the DES simulation in Ansys Fluent. The SIMPLE algorithm is used for the pressure-velocity coupling,

as this is less computationally expensive for the region where LES is used [39]. The relaxation factors that are used for the RANS, URANS and DES can be seen in table 7. This is used because these are the default settings for Ansys Fluent, giving stable solutions for all simulations. Hence, over-relaxation is not needed to enhance the stability of the simulations.

Table 7: Relaxation factors used for the RANS, URANS and DES.

Relaxation factors	
Pressure	0.3
Density	1
Body Forces	1
Momentum	0.7
Turbulent transport quantity	0.8
Turbulent viscosity	1

5 Results

The results obtained in this thesis differ from the ones obtained in the specialization project of Bjuri [11]. Firstly, for the RANS simulations done the quality of the mesh is improved, reducing the aspect ratio of the cells. For the RANS simulations, different wall functions have been tested out to observe whether this gives similar results to resolving the boundary layer, also other RANS options have been investigated. Moreover, LES and DES methods are examined further in the benchmarks.

5.1 Fully turbulent case

5.1.1 Grid sensitity analysis for RANS

A grid sensitivity analysis is conducted to determine what mesh should be used to investigate the different RANS turbulence models. The coarsest mesh investigated has approximately 526 000 nodes and is refined near all of the walls such that the y^+ value approximately stays below 5 in the entire domain. This is recommended when resolving the boundary layer for RANS modelling approaches, and is recommended when using the enhanced wall treatment in Fluent. The y^+ values for the coarsest mesh are given in table 8. Although some y^+ values in the coarsest mesh exceed the recommended value, they are close enough to minimize errors. The mesh is then refined using a factor of $2\sqrt{2}$ for each refinement, resulting in a medium mesh of 1,455,000 nodes and a fine mesh of 3,780,000 nodes. The chosen RANS model for the grid sensitivity analysis is the standard $k-\epsilon$ model, which has yielded the best results in previous simulations conducted in Bjuri's specialization project and Bjerkeli's master thesis [11, 1].

Table 8: The y^+ values for the mesh consisting of 526 000 nodes for the fully turbulent case.

	Ceiling	Floor	Inlet wall	Outlet wall	Left/Right wall
Max	5.91	4.93	4.29	4.84	7.28
Average	2.33	2.19	2.17	2.93	1.87

In figure 32, the results of the grid sensitivity analysis are presented. It was observed that refining the mesh does not significantly affect the velocity plots. You can only see a difference between the plots at the horizontal line by the floor at x/H=0.5 and by the horizontal line at the ceiling by the top outlet wall corner (x/H=2.9). However, this difference is only visible when zooming in and is minimal. Therefore, due to the small differences between the meshes and the computational benefits of using a coarser mesh, the coarsest mesh is selected for the remaining RANS simulations.

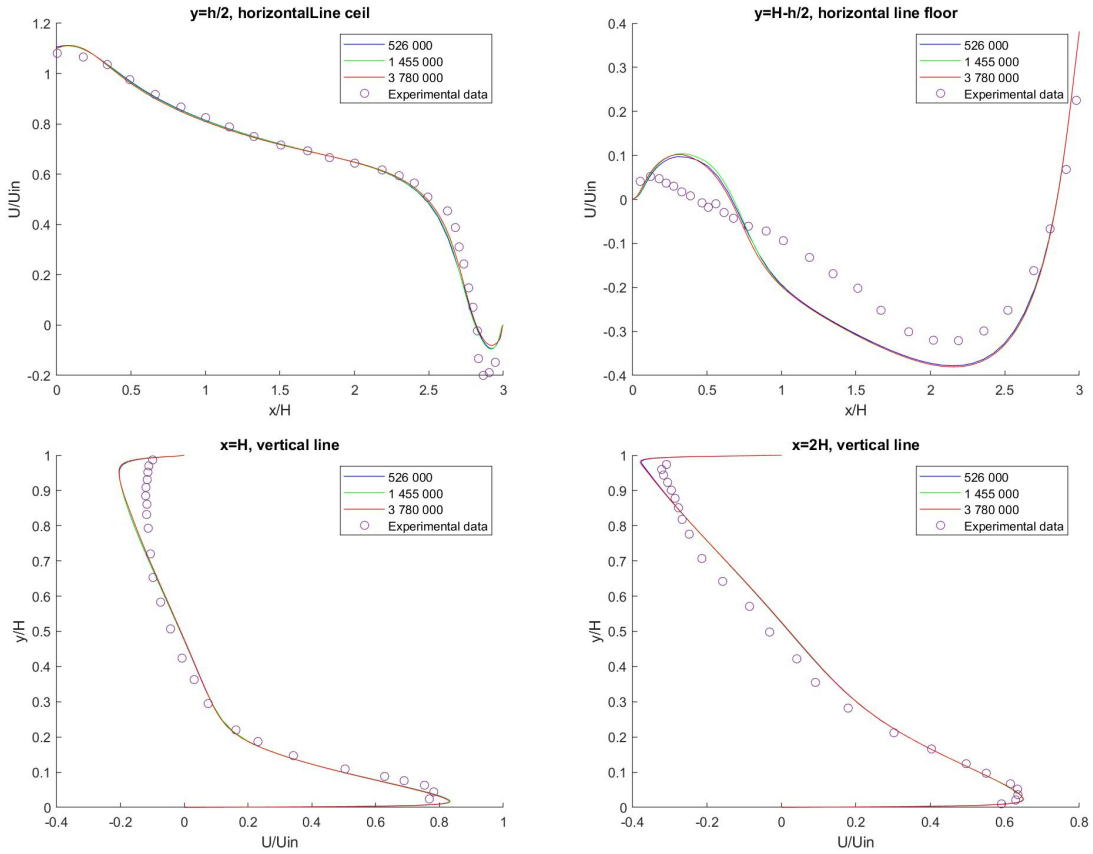

Figure 32: Grid sensitivity analysis with mesh of: 526 000, 1 455 000 and 3 780 000 nodes on the fully turbulent case. Standard $k-\epsilon$ model used

5.1.2 RANS simulations

The RANS models that are being investigated are the standard $k-\omega$, BSL $k-\omega$, SST $k-\omega$, standard $k-\epsilon$, Realizable $k-\epsilon$, RNG $k-\epsilon$ and the Spalart-Allmaras model. The default options from Fluent are utilized for the different turbulence models. Velocity profiles of $k-\omega$ models are shown in Figure 33. It is evident that these models predict the velocity profiles accurately. However, all the models overestimate the velocity at the ceiling line, especially the standard $k-\omega$ model. Nevertheless, the models can efficiently predict the corner flow at the ceiling line. Near the inlet at the floor line, the standard $k-\omega$ model predicts velocity the best, while all $k-\omega$ models slightly overestimate the velocity. At the vertical line x=H, all the $k-\omega$ models predict a too sharp velocity profile close to the ceiling. At the floor line, the BSL $k-\omega$ model incorrectly predicts a positive velocity, whereas the other models predict a negative velocity. At the other vertical line x=2H, all $k-\omega$ models can model the flow accurately, but the BSL $k-\omega$ model exhibits better coherence with experiments.

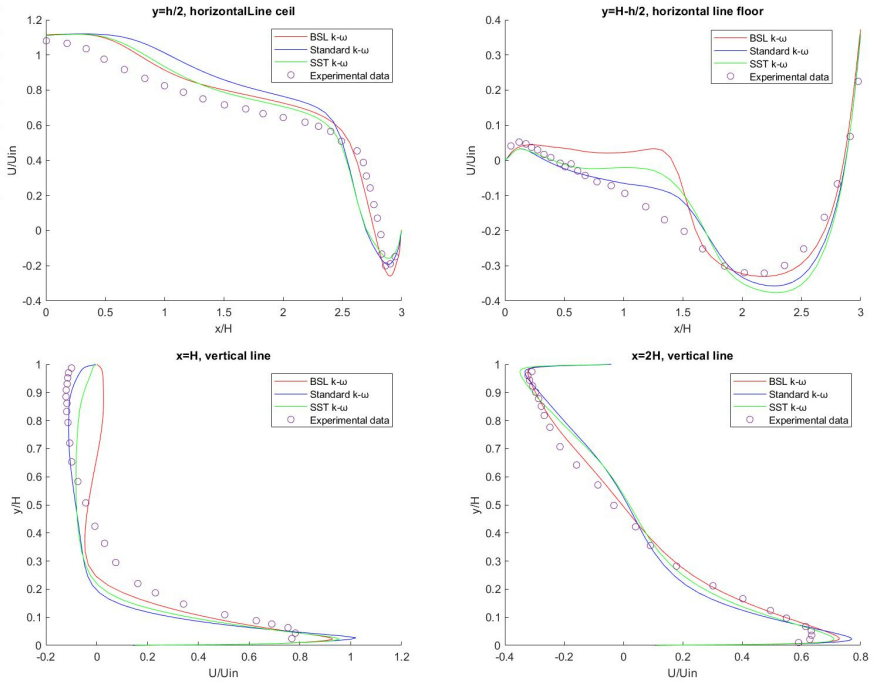

Figure 33: K-ω models on the fully turbulent case.

Figure 34 displays the velocity profiles of the $k-\epsilon$ models and the Spalart-Allmaras model. All these models are capable of accurately predicting the velocity. They perform well in predicting the velocity near the ceiling, but struggle to model the secondary flow in the upper right corner. At the horizontal line by the floor, the RNG $k-\epsilon$ and the realizable $k-\epsilon$ model inaccurately predict a negative velocity near the wall by the inlet, whereas the Spalart-Allmaras model predicts the flow well. All models predict a reverse flow near the floor, which is excessively high. However, at both of the vertical lines, the turbulence models correctly predict the shape of the velocity profile.

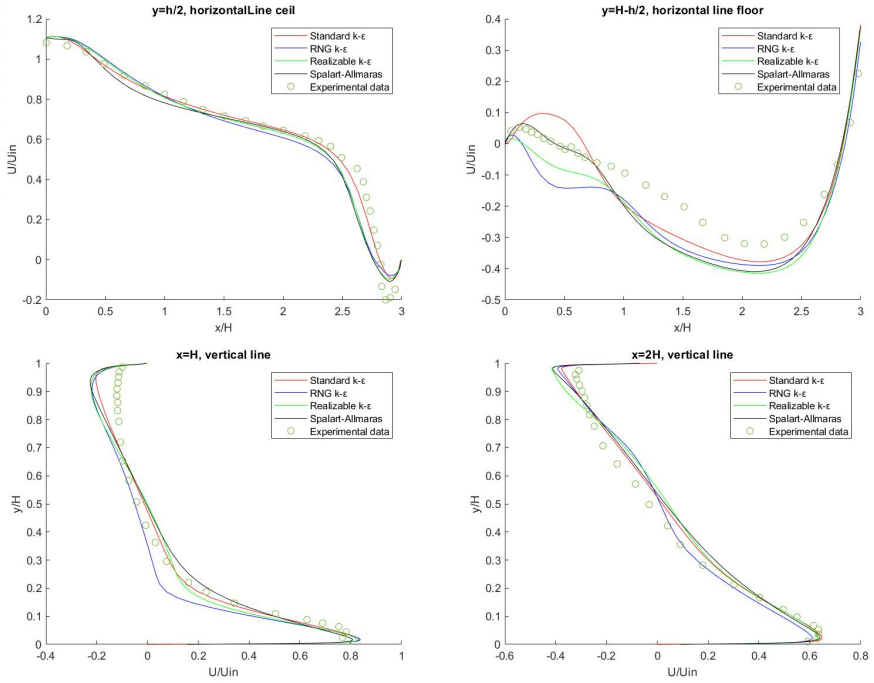

Figure 34: k-ϵ models and the Spalart-Allmaras model on the fully turbulent case.

In Table 9, the Root Mean Square Error values of various turbulence models at different lines are presented. The standard $k-\epsilon$ model yields the most accurate results overall. Additionally, the $k-\epsilon$ models exhibit lower errors compared to the $k-\omega$ models, except for the BSL $k-\omega$ model, which performs well. The Spalart-Allmaras model also yields satisfactory results for this benchmark. These findings align with the results obtained in Bjerklie's master thesis [1], where the standard $k-\epsilon$ model was the best-performing model. However, when compared to the LES results from Taghinia et al. [2], the RANS results are less precise, as expected. When comparing the RMSE values in Table 9 to those obtained by Bjerkeli [1], it is evident that Bjerkeli's values are lower than the values presented in this thesis.

Table 9: RMSE values of the default RANS models on the fully turbulent case.

Turbulence models	Horizontal line ceiling	Horizontal line floor	Vertical line x=H	Vertical line x=2H	Average
BSL $k-\omega$	0.0956	0.0718	0.1177	0.0599	0.0863
SST $k-\omega$	0.1462	0.0588	0.1158	0.0671	0.0970
Standard $k-\omega$	0.1700	0.0427	0.1332	0.0816	0.1069
RNG $k-\epsilon$	0.1117	0.0926	0.0916	0.0658	0.0904
Realizable $k-\epsilon$	0.1107	0.086	0.0796	0.0699	0.0866
Standard $k-\epsilon$	0.0669	0.0748	0.0565	0.0691	0.0668
Spalart-Allmaras	0.1137	0.0757	0.0680	0.0649	0.08058

Figure 35 displays streamline plots for the midplane obtained using the BSL $k-\omega$, SST $k-\omega$, standard $k-\omega$ and standard $k-\epsilon$ models. A comparison with Rong and Nielsen's streamline plot [42] given in figure 10 reveals that both BSL $k-\omega$ streamline plots show three circulation vortices. However, Rong and Nielsen predicted vortex at the lower left corner is closer to the corner than the one obtained in this study. For the SST $k-\omega$ model, Rong and Nielsen get four recirculation vortices, while only two are seen in figure 35. For the standard $k-\omega$ model, both streamline plots show three circulation vortices. However, the lower left vortex in Rong and Nielsen's streamline plot is larger than in this study. For the standard $k-\epsilon$ model, Rong and Nielsen only predict one large circulation vortex, while figure 35 displays an additional vortex at the upper right corner.

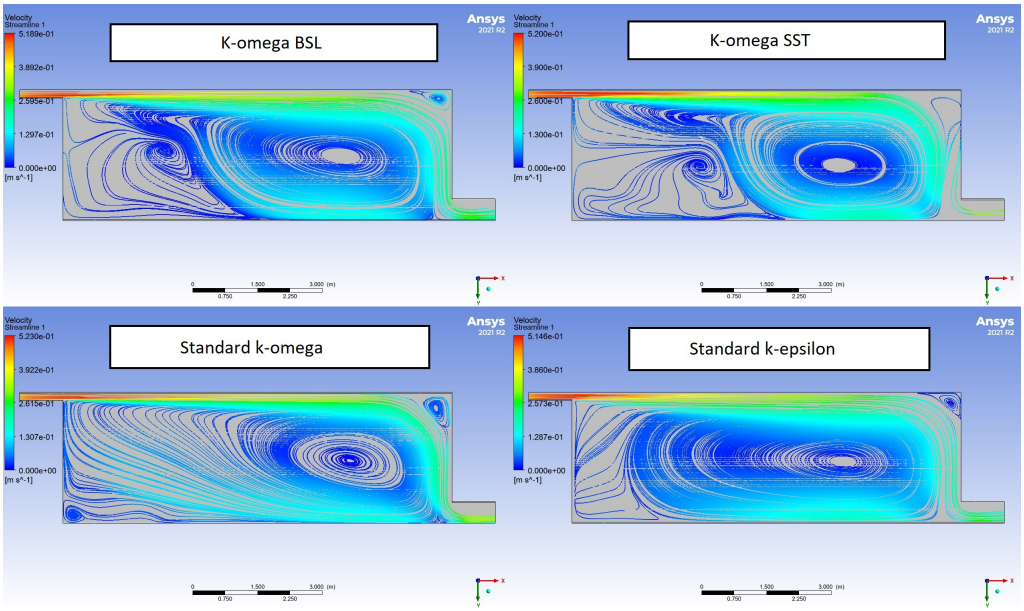

Figure 35: Streamlines of the BSL $k-\omega$, SST $k-\omega$, standard $k-\omega$ and standard $k-\epsilon$ model on the fully turbulent case at the xy-midplane.

5.1.3 Wall treatment approaches

Several wall treatment approaches were tested out on the fully turbulent benchmark. These included the standard wall function, scalable wall function, non-equilibrium wall function, and enhanced wall treatment, which resolves the boundary layer. Table 1 lists the recommended y^+

values for each approach. The mesh used when employing wall functions is less refined near the walls, requiring fewer nodes compared to when resolving the boundary layer. Figure 36 shows the mesh for both cases, for the refined mesh consisting of 526 000 nodes and the wall function mesh containing 135 000 nodes. The latter represents a reduction of around 75%, resulting in less computational effort for the simulation. This is the benefit of utilizing wall functions.

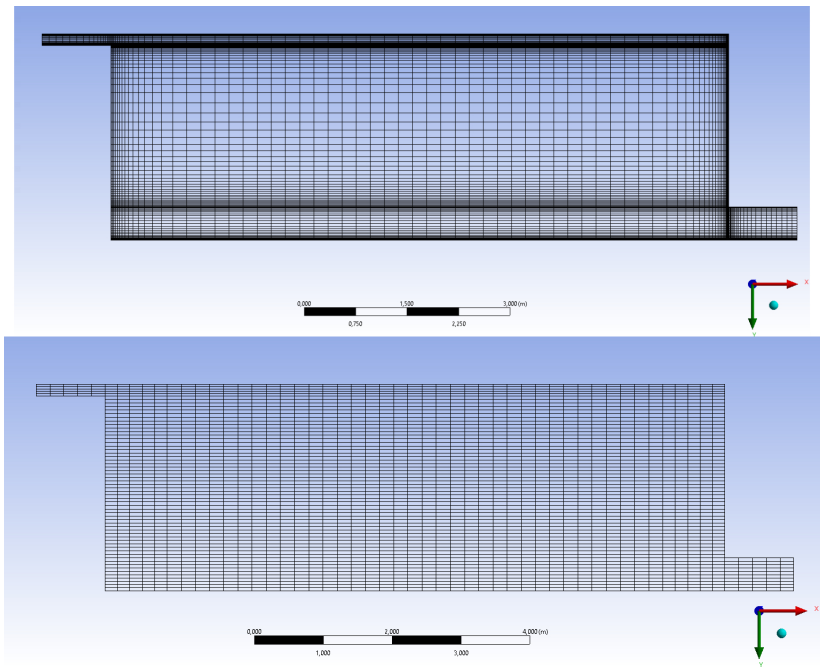

Figure 36: The top mesh has been refined to include 526,000 nodes, while the lower mesh, which utilizes wall functions, only has 135,000 nodes.

Several wall treatment approaches were tested on the standard $k-\epsilon$, RNG $k-\epsilon$, and realizable $k-\epsilon$ turbulence models. Figure 37 shows the velocity profiles obtained using the standard $k-\epsilon$ model for the different wall treatment approaches. The results are almost identical to those obtained in Bjerkeli's master thesis [1] shown in figure 14. Both the scalable and standard wall functions can predict the velocity profile quite well, but they struggle with the secondary flow by the corner. In these areas, the enhanced wall treatment performs better. Overall, the enhanced wall treatment yields the best results for predicting the velocity field for the standard $k-\epsilon$ model. Similar results were obtained using the same wall treatment methods on the realizable $k-\epsilon$ model.

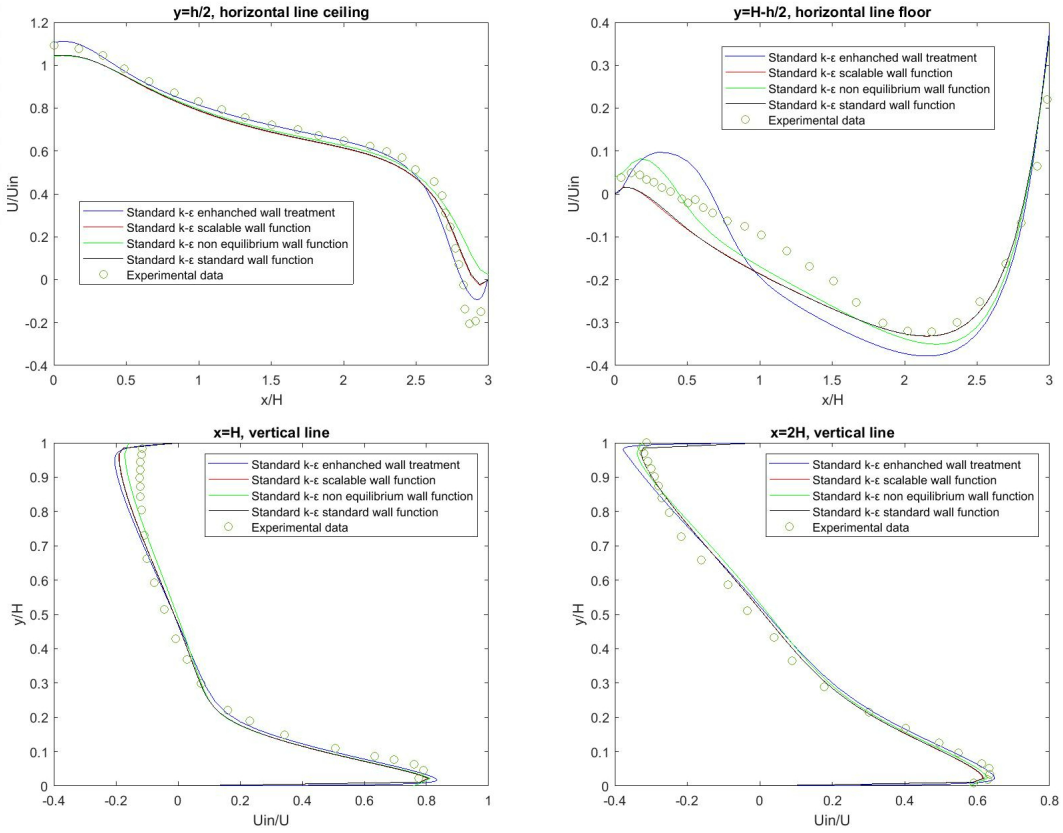

Figure 37: Velocity profiles of different wall treatment approaches when using the standard $k-\epsilon$ model on the fully turbulent case.

Figure 38 displays the velocity profiles of various wall treatments for the RNG $k-\epsilon$ model. Similar to the standard $k-\epsilon$ model, the velocity profiles of the different wall treatments follow a similar trend. However, at y=H-h/2, the standard and scalable wall function show better agreement with experimental data. Table 30 presents the RMSE values for the RNG $k-\epsilon$ model with different wall treatment approaches. Using the standard wall function reduces errors compared to enhanced wall treatment. In conclusion, wall functions can be employed for the fully turbulent case to reduce computational expenses as compared to resolving the boundary layer. However, it may yield less accurate results near corners and walls.

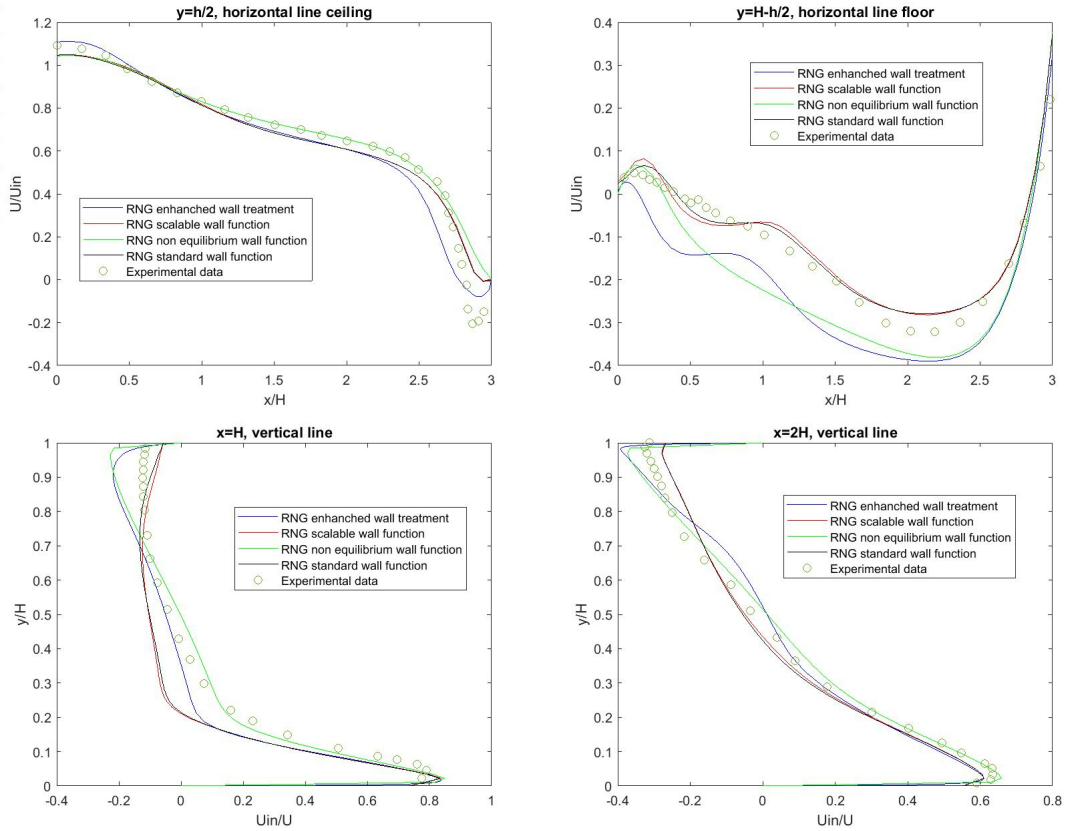

Figure 38: Velocity profiles of different wall treatment approaches when using the RNG $k-\epsilon$ model on the fully turbulent case.

5.1.4 Correctors and other options for RANS

Until now, only the default turbulence models have been utilized in Fluent. Nevertheless, several correctors and options are available, as described in section 2.4.5, that could potentially enhance the results. The strain-vorticity-based production and corner correction option were experimented for the Spalart-Allmaras model, but neither produced any noticeable improvement from the default Spalart-Allmaras. For the $k-\epsilon$ model, the production limiter option and pressure gradient effects options were tested, with the pressure gradient effect showing a minimal improvement on the Realizable $k-\epsilon$ model, as shown in figure 91. It also showed an improvement on the RNG $k-\epsilon$ models, though not as significant as the improvement achieved using the standard wall function. The corner and low-Re correction options were examined for the $k-\omega$ models. These correctors did not enhance the results for the standard $k-\omega$ and BSL $k-\omega$ models. However, the low-Re corrector improved the prediction of the velocity profiles for the SST $k-\omega$ model, as demonstrated in figure 39. The SST $k-\omega$ model with the low-Re corrector gives a better prediction for the flow near the floor close to the inlet wall, as seen in the horizontal line by the floor (y=H-h/2) and the vertical line (x=H). This can additionally be seen in table 10, which shows the RMSE values of the different corrector options for the SST $k-\omega$ model. In this table, it can be seen that the low-Re corrector gives overall the least error for the SST $k-\omega$ model. In conclusion, using the pressure gradient effect option for the $k-\epsilon$ models may produce better results, and at the very least, will not result in worse results. The low-Re corrector is only effective for the SST $k-\omega$ model and should be used cautiously for the other $k-\omega$ models.

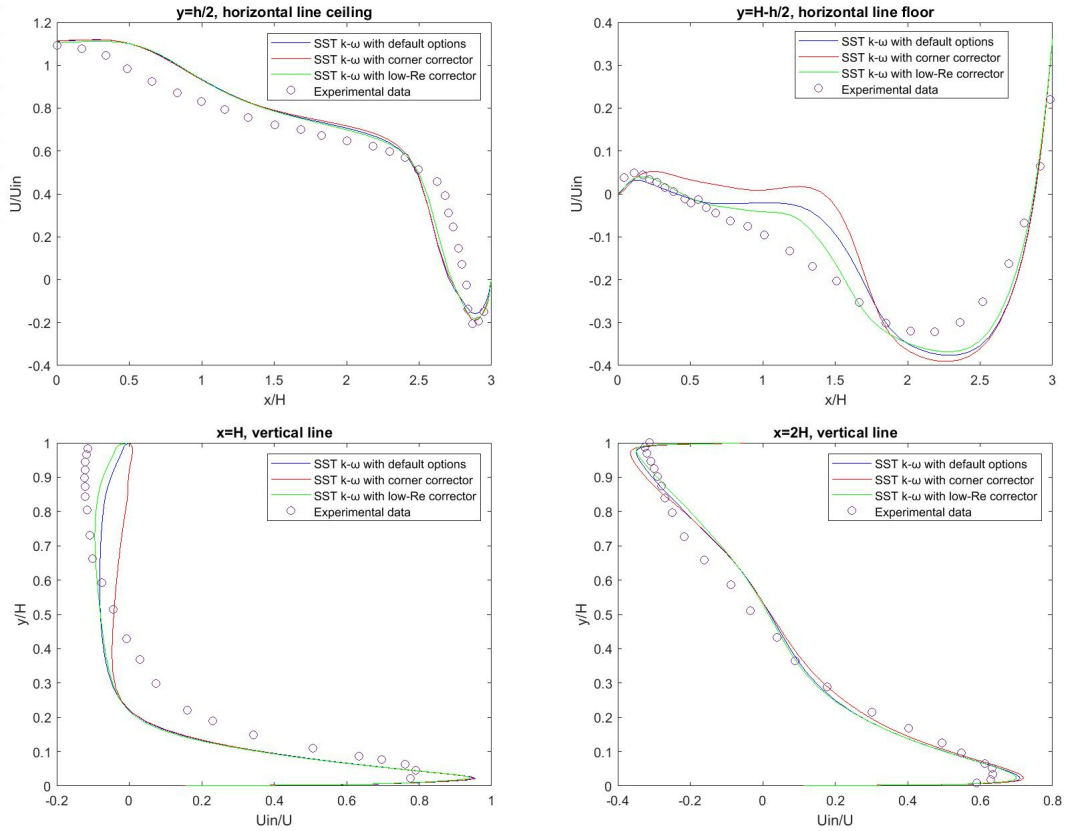

Figure 39: Velocity profiles of different correctors in Fluent using the SST $k-\omega$ model on the fully turbulent case.

Table 10: RMSE values for the different correctors of the SST $k-\omega$ model, for the fully turbulent case.

	Horizontal line ceiling	Horizontal line floor	Vertical line x=H	Vertical line x=2H	Average
Default options	0.1462	0.0588	0.1158	0.0671	0.0970
Corner corrector	0.1434	0.0813	0.1281	0.0681	0.1052
Low-Re corrector	0.1350	0.0451	0.1135	0.0650	0.0897

Using different wall treatment approaches, correctors or other options in Fluent gives less RMSE value for the SST $k-\omega$, RNG $k-\epsilon$ and realizable $k-\epsilon$ model. The biggest change is with the SST $k-\omega$ and RNG $k-\epsilon$ model which gives a relatively big improvement. The updated RMSE values when optimizing the RANS models are given in table 11.

Table 11: RMSE values when the RANS models are optimized for the fully turbulent case. The places with bold texts shows where an improvement was made.

Turbulence models	Horizontal line ceiling	Horizontal line floor	Vertical line x=H	Vertical line x=2H	Average
BSL $k-\omega$	0.0956	0.0718	0.1177	0.0599	0.0863
SST $k-\omega$	**0.1350**	**0.0451**	**0.1135**	**0.0650**	**0.0897**
Standard $k-\omega$	0.1700	0.0427	0.1332	0.0816	0.1069
RNG $k-\epsilon$	**0.0986**	**0.0439**	**0.0951**	**0.0383**	**0.06898**
Realizable $k-\epsilon$	**0.1071**	**0.0858**	**0.0750**	**0.0694**	**0.0843**
Standard $k-\epsilon$	0.0669	0.0748	0.0565	0.0691	0.0668
Spalart-Allmaras	0.1137	0.0757	0.0680	0.0649	0.08058

5.1.5 URANS

URANS simulation was also conducted on the optimized RANS models. A timestep of 0.1 seconds was used, as this was proved through a time sensitivity analysis to give sufficient results for DES. After reaching statistical steady state, the simulations were averaged over 20 FTTs. Figure 40 displays the results of the URANS velocity profiles using the standard $k-\omega$ model. The RANS and URANS velocity profiles are similar, with the only disparity being near the floor, where the URANS overestimates the velocity close to the inlet wall. For other RANS/URANS models, the URANS performs the same or worse than RANS. The primary differences between the RANS and URANS velocity profiles can be observed near the floor of the cavity.

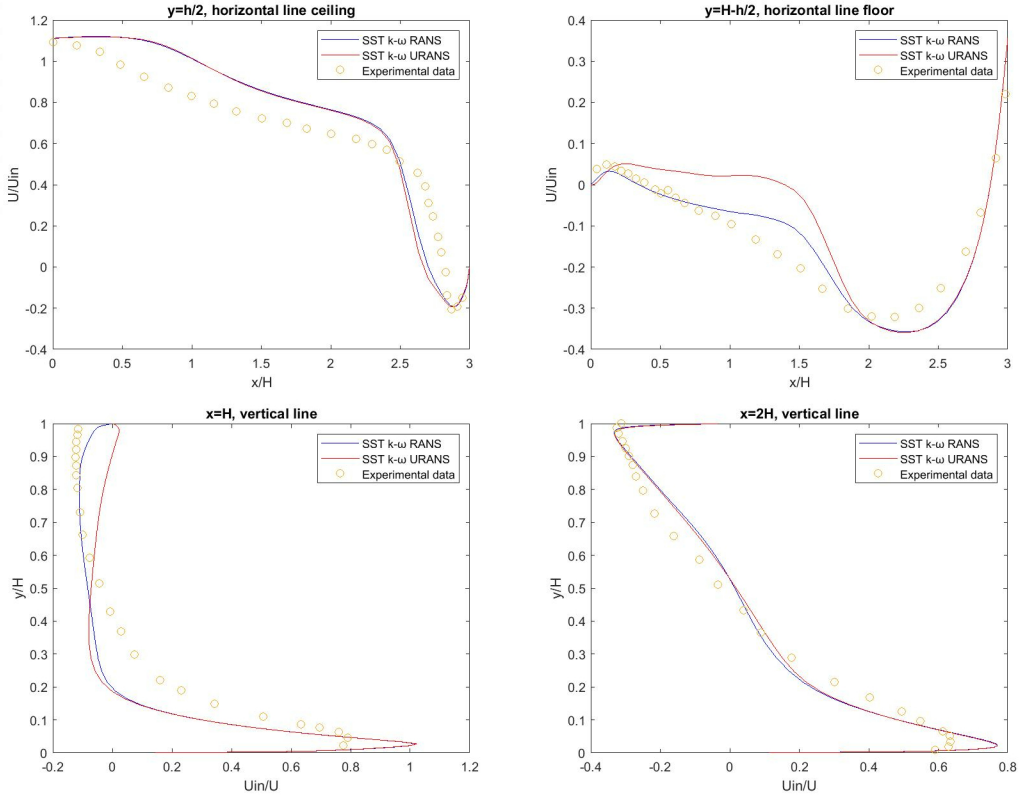

Figure 40: Velocity profiles of RANS and URANS of the standard $k-\omega$ on the fully turbulent case.

5.1.6 DES

For the DES approach, an appropriate mesh is needed to resolve enough of the eddies at the LES region. Two main criteria are used to verify if the mesh is sufficient for LES and DES. The first criterion requires that the y^+ values at the walls should be one or less [32]. The second criterion is that the mesh should be capable of resolving 80% of the turbulent kinetic energy [27]. This is equivalent to having the f-value, as defined in equation (33), above five throughout the flow domain. However, for the investigation of DES, it is only necessary that the f-value is above 5 in the far-field region, where LES is activated. To investigate these criteria, RANS simulations are conducted while adjusting the mesh. The standard $k-\epsilon$ model is used for the RANS simulation, as it provided the best results and lowest RMSE values. The mesh that mostly fulfilled these criteria consisted of 6,934,000 nodes and is displayed in figure 41. The mesh was refined at the free-shear region, where the inlet flow interacts with the air in the cavity, and near the walls. The y^+ values were mostly around unity and are listed in table 12. Although the y^+ values at the inlet, outlet, left, and right walls were slightly above 1, the average y^+ value remained below one at these walls, making any error negligible.

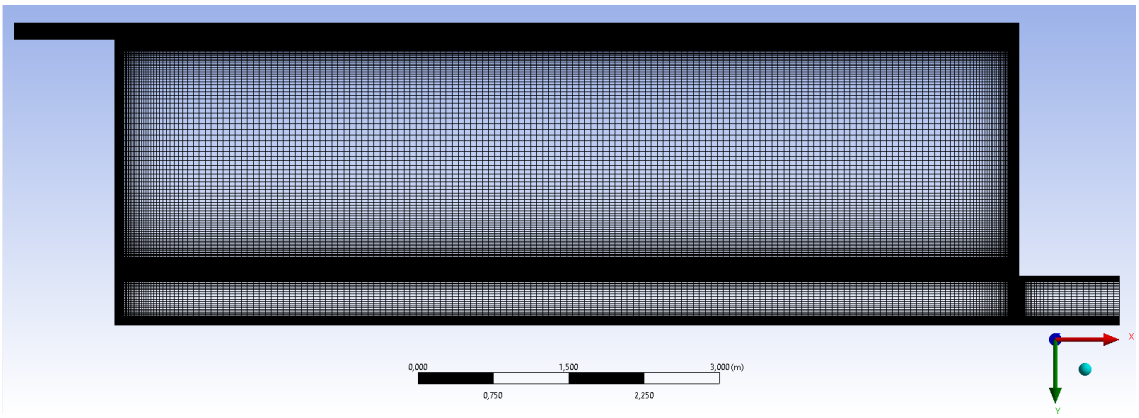

Figure 41: Mesh used for DES refined near the walls and in the free-shear region consisting of 6 934 000 nodes for the fully turbulent case.

Table 12: The y^+ values of the mesh used for DES of the fully turbulent case gathered by a RANS simulation on the DES mesh using the standard $k-\epsilon$ method.

Wall	Floor	Ceiling	Inlet	Outlet	Left/Right
Max	0.5361	0.5051	1.2882	2.5378	1.4932
Average	0.2195	0.1362	0.6013	0.5459	0.2605

Figure 42 displays the contour plot of the f-value for the fully turbulent case at the xy-midplane. It is noticeable that the f-value remains mostly above five on the xy-midplane. However, around the cavity inlet, where most of the shearing occurs, the f-value is slightly below 5. However, this region requires significant refinement to ensure the f-value surpasses five. Although the f-value is below 5 near the walls, it is unnecessary to fulfil this criterion in this area as RANS will be utilized in this area.

Figure 42: F-value at the xy-midplane of the fully turbulent case gathered from a RANS simulation using the standard $k-\epsilon$ model.

The DES model used on this mesh was the DES realizable $k-\epsilon$ model with the default options defined in Fluent. This model was chosen due to its good RANS model performance compared to other RANS models. The FTT was calculated to be 130 seconds by using equation (25). This was a rough estimation because of the uncertainties when calculating the average velocity of the air in

the cavity. The time step, which gave a CFL number of one was approximately 0.005 seconds, a small time step compared to the FTT. A time-step sensitivity analysis was conducted to investigate the feasibility of increasing the time step and reducing simulation time.

The simulations were initialized with the RANS model that produced the least error when compared to experimental data, which was the standard $k-\epsilon$ model. Statistical steady-state was achieved and confirmed by monitoring the total turbulent kinetic energy at each time step. The averaging sensitivity analysis, as depicted in figure 43, showed that averaging over 6 FTTs was sufficient to obtain statistically independent velocity profiles. Averaging over more than 6 FTTs had a negligible effect on the results.

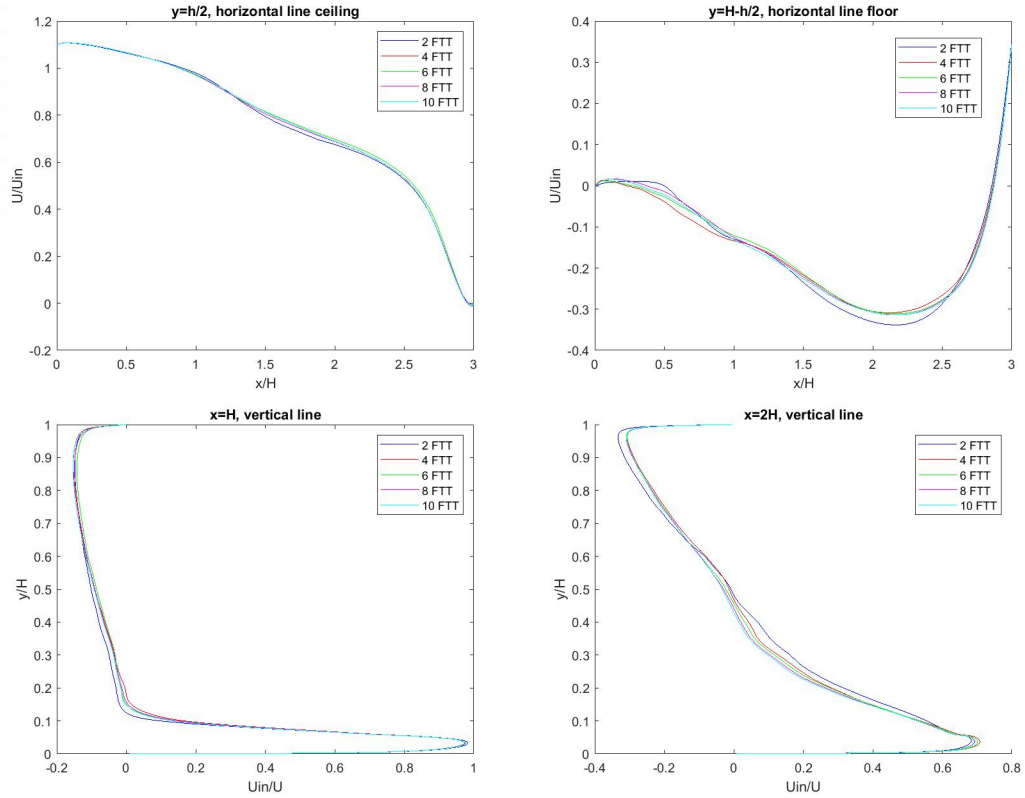

Figure 43: Averaging sensitivity analysis for DES realizable $k-\epsilon$ on the fully turbulent case with a time step of 0.1 seconds.

For the time sensitivity analysis, five different time steps were investigated $\Delta t = 0.5$, $\Delta t = 0.1$, $\Delta t = 0.05$, $\Delta t = 0.025$ and $\Delta t = 0.01$ seconds. Figure 44 displays the velocity profiles with the different time steps. The velocity plot for $\Delta t = 0.5$ seconds differs significantly from the other time steps, indicating that a time step of 0.5 seconds is too large to simulate the turbulence from the eddies of the flow. Another observation is that the velocity profiles obtained when using a time step of 0.01 seconds differ from the velocity profiles of the time steps $\Delta t = 0.1$, $\Delta t = 0.05$ and $\Delta t = 0.025$ seconds. Using a time step of 0.01 seconds gives more accurate results compared to the other time steps, but the trade-off is more computational expensiveness. Consequently, a time step of 0.1 seconds is used for the rest of the DES and LES analyses, although it may result in additional errors compared to using a time step of 0.01 seconds.

Figure 44 shows the velocity profiles for the DES realizable $k-\epsilon$ model. Observing the graph, the velocity is over-predicted at the ceiling line, and the secondary vortex at the upper right corner is not predicted at all. Additionally, the velocity profile at the first vertical line is too sharp compared to the experiment. The DES model anticipates less turbulence mixing in the cavity, leading to a flow that lacks dissipative behaviour compared to the experiment. For the horizontal velocity profile near the floor (y=H-h/2) and the vertical line x=2H, the DES give relatively good results, but struggles slightly with predicting the velocity near the walls.

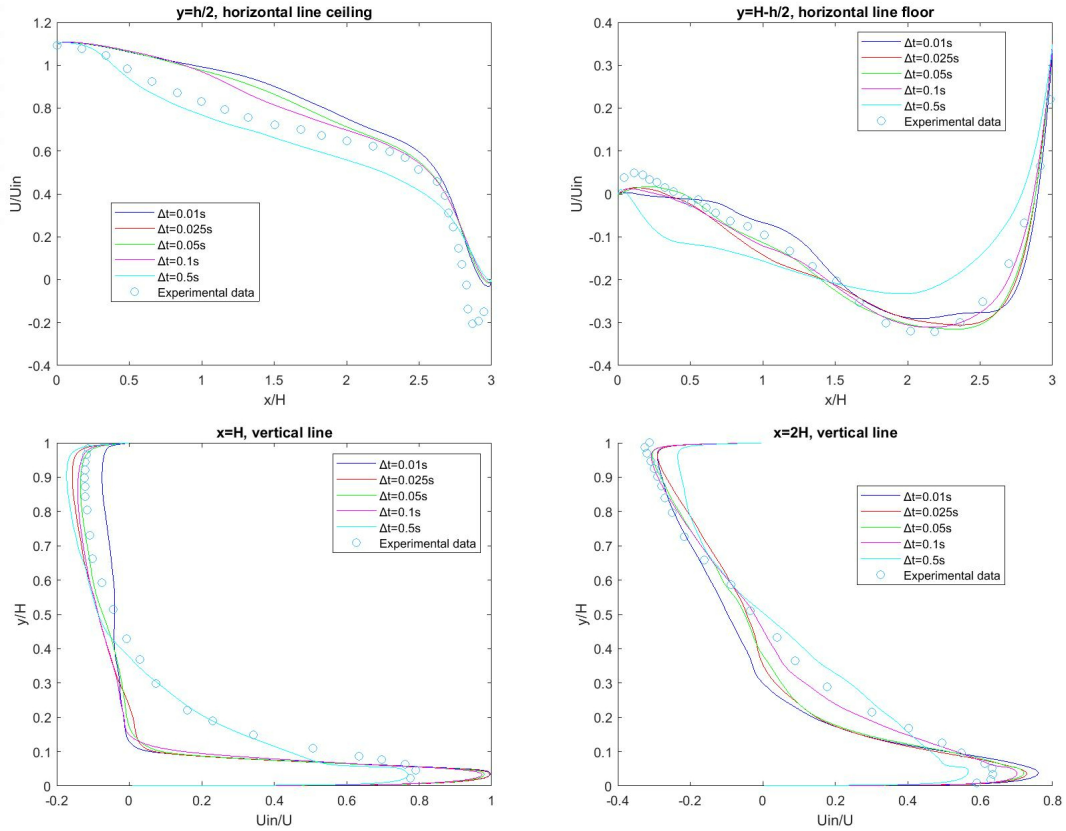

Figure 44: Velocity profiles from the DES realizable $k-\epsilon$ model with different time steps on the fully turbulent case.

Various synthetic turbulence methods were tested at the inlet to improve the velocity profiles and introduce more turbulent structures in the incoming flow. The approaches tested out were the spectral synthesizer, synthetic turbulence generator and vortex method, all are available in Fluent. For the vortex method, 999 vortices were used, as recommended by Gerasimov [37], who suggests using $N/4$ vortices. Since the inlet mesh consists of 4500 faces, ideally, 1125 vortices should be used. However, the maximum number of vortices allowed in Fluent is 999. In figures 45 and 46, the abbreviations listed in table 13 are used.

Table 13: The abbreviations used for the legends of figures 45 and 46 of the various DES synthetic turbulence approaches at the inlet.

Deatached Eddy simulation: No Pertubations	DES NP
Deatached Eddy simulation: Spectral Synthesizer	DES SS
Deatached Eddy simulation: Synthetic Turbulence Generator	DES STG
Deatached Eddy simulation: Vortex Method	DES VM

The velocity profiles of the DES realizable $k-\epsilon$ model with the different synthetic turbulent approaches at the inlet are given in figure 45. It can be observed that all of the synthetic turbulence models give an improvement compared to having no perturbations at the inlet. However, the vortex method outperforms the other approaches, as demonstrated in table 31, which shows the RMSE values of the different methods. Despite the improvements, all approaches still struggle to predict the secondary flow near the upper right corner and over-predict the velocity at the horizontal ceiling line (y=h/2) close to the inlet. Additionally, the vertical line x=H velocity profile remains too sharp near the inlet for all the approaches.

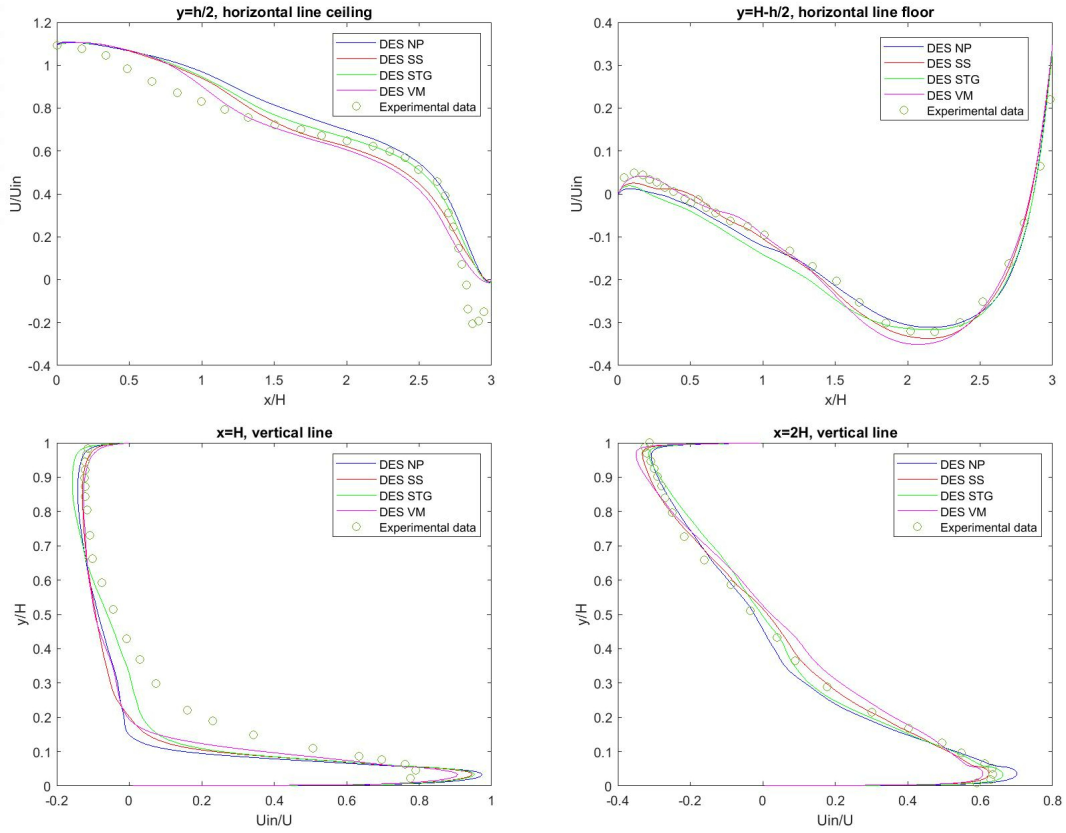

Figure 45: Velocity profiles when using different synthetic turbulence approaches at the inlet for the DES realizable $k-\epsilon$ model on the fully turbulent case.

The turbulence intensities of the different approaches at the inlet of the cavity are given in figure 46. The turbulence intensity is calculated by dividing the RMS velocity by the bulk inlet velocity. The figure also includes the measured turbulence intensity for the experiment. It is observed that all the DES approaches significantly underestimate the turbulence intensity. When there is no perturbation for the velocity at the inlet, the turbulence intensity is close to zero, which is very different from the experimental measurement. The spectral synthesizer approach results in a turbulence intensity that is only 20% of the measured value. Using the synthetic turbulence generator and vortex method gives a turbulence intensity that is only half of what was measured in the experiment. This could explain why a sharp velocity profile is observed at the vertical line x=H. This is also the reason why the vortex method and synthetic turbulent generator approach give a less sharp velocity profile and a better prediction of the velocity profile at the horizontal ceiling line y=h/2.

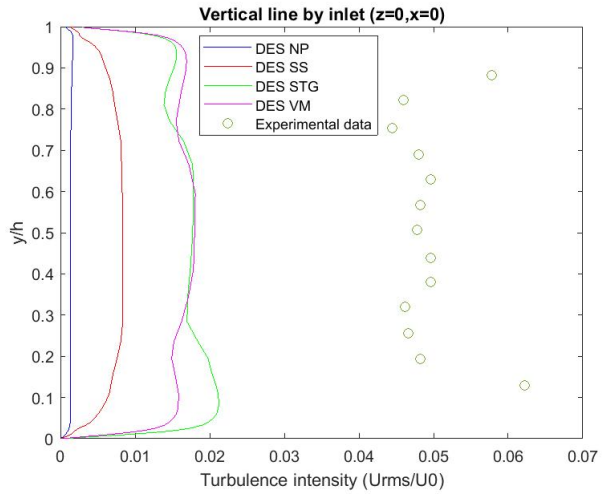

Figure 46: Plot of the turbulence intensities at the inlet of the cavity for the different synthetic turbulence approaches on the DES realizable $k-\epsilon$ model on the fully turbulent case. The turbulence intensities are calculated at the vertical line of the cavity by dividing the RMS velocity value with the inlet bulk velocity of the CFD inlet.

A reason for this underprediction of the turbulent intensity could be grey zone effects coming from the switching between RANS and LES modelling. Especially near the inlet switching to LES too late could result in the RANS region dissipating and reducing the turbulent structures created at the inlet. The DES TKE Dissipation Multiplier, which shows at what region LES and RANS modelling is being used, is shown in figure 47 for the xy-midplane when the vortex method is used at the inlet. When this value is one, LES is used, and when it is zero, RANS is used. As expected, RANS is used in the near-wall region, while LES is used in the far-wall region. LES is applied in the shear region close to the ceiling but not above it, implying that it is not used for the entire wall jet region. LES is also not used near the inlet wall, where RANS is mainly used. Inside the inlet duct, RANS is mostly used. This could have the undesirable effect of RANS dampening the perturbation at the inlet, which might be a reason for the turbulent intensity being so low at the inlet of the cavity. Additionally, this RANS dampening effect also happening in the wall jet could be the reason why no secondary flow is observed at the upper right corner of the cavity.

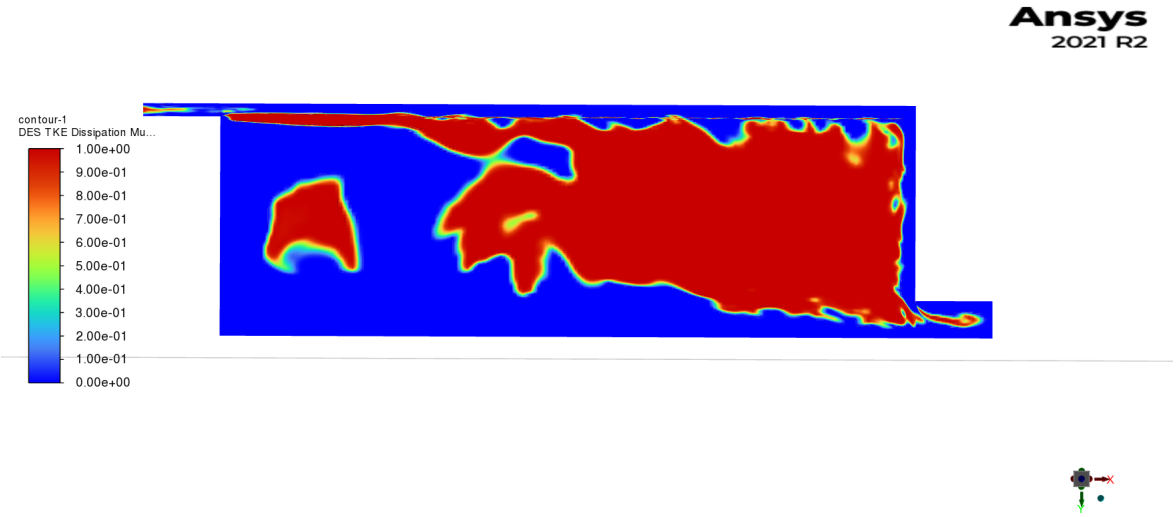

Figure 47: Contour plot at the xy-midplane of the DES TKE multiplier variable of the DES realizable $k-\epsilon$ method with the vortex method at the inlet for the fully turbulent case.

To gain better control over the transition between the areas where RANS and LES are utilized, the Spalart-Allmaras DES model was implemented. This model utilizes mesh quality as the sole variable to determine whether RANS or LES is used. Essentially, RANS is only employed in the near-wall area, while LES is reserved for the far-wall region. The DES Spalart-Allmaras model with the vorticity-based production term and the vorticity/strain-based production term were investigated. All DES models use the spectral synthesizer method to generate turbulent structures at the inlet. For reference, the abbreviations used in the legend for both figure 49 and 48 are provided in table 14.

Table 14: Abbreviations used for the figures with the different DES models.

Deatached Eddy simulation: Spalart-Allmaras vorticity-based production	DES S-A V-P
Deatached Eddy simulation: Spalart-Allmaras vorticity/strain-based production	DES S-A V-S-P
Deatached Eddy simulation: Realizable $k-\epsilon$	DES $k-\epsilon$

Analyzing figure 48, it can be observed that the DES Spalart-Allmaras overpredicts the velocity at the horizontal ceiling line (y=h/2) close to the inlet of the cavity and perform worse than the DES realizable $k-\epsilon$ model here. However, the DES Spalart-Allmaras model can predict the secondary flow phenomena at the upper right corner well, while the DES realizable $k-\epsilon$ struggles to predict this corner vortex. At the horizontal line by the floor, the DES Spalart-Allmaras models perform worse compared to the DES realizable $k-\epsilon$. Also, at the vertical line x=H, the DES Spalart-Allmaras models give a sharper velocity profile. Overall the DES Spalart-Allmaras models perform worse than the DES realizable $k-\epsilon$ model, the only exception being at the upper right corner. This can be seen in table 32 showing the RMSE values of the velocity. The DES Spalart-Allmaras model with the vorticity/strain-based production term performs better than the DES Spalart-Allmaras model with the vorticity-based production term at the horizontal line by the ceiling (y=h/2) and by the vertical line (x=2H).

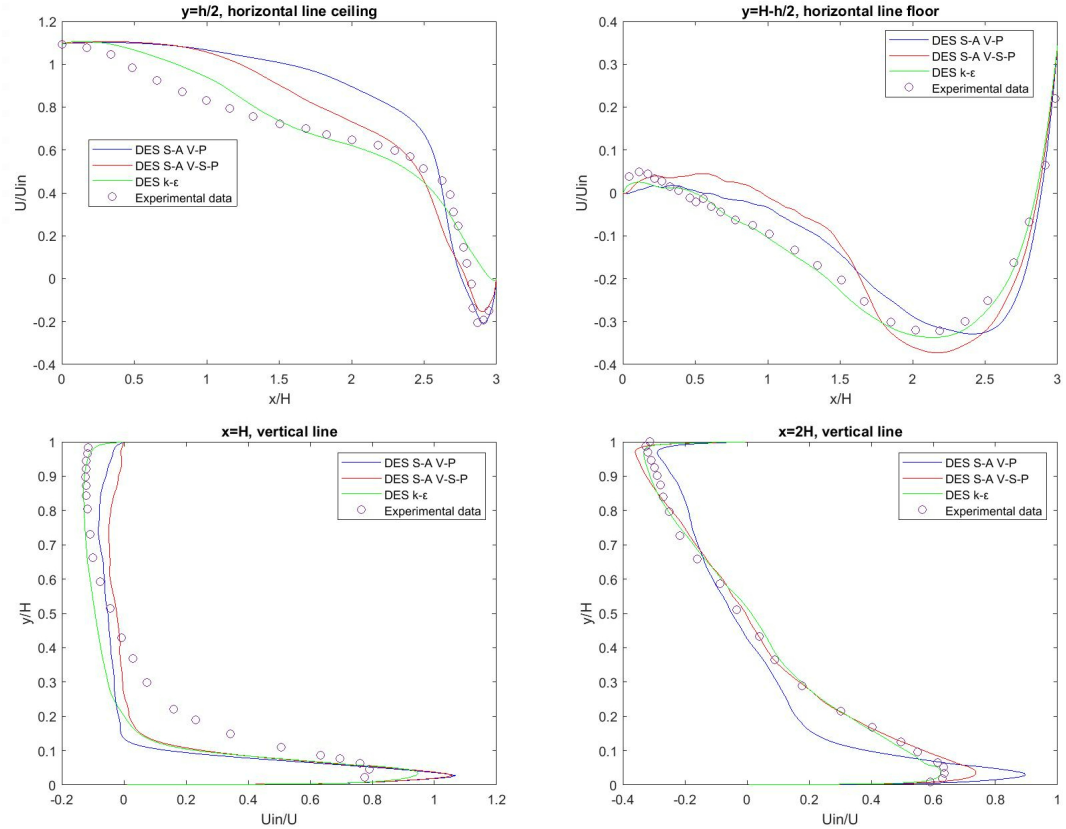

Figure 48: Velocity profiles of the different DES models using Spectral Synthesizer method at inlet for the fully turbulent case.

In figure 49, the turbulence intensity of the various DES models for the vertical line at the cavity's inlet is shown. It is noticeable that the DES realizable $k-\epsilon$ and the DES Spalart-Allmaras models with the vorticity-based production term offer similar results. However, the DES Spalart-Allmaras model with vorticity/strain-based production term yields higher turbulence intensity, particularly near the ceiling wall and the inlet's floor. This is characteristic behaviour for turbulent flow in a rectangular channel flow. Despite this, the turbulence intensity is still significantly lower in the middle of the wall jet, approximately 30% lower than the experimentally measured turbulence intensity. The grey zone effect caused by switching between the RANS and LES modes at the inlet should have a lesser impact on turbulence intensity, as this switching only takes place near the walls for DES Spalart-Allmaras. Nevertheless, it could still be a contributing factor to the underpredicted turbulence intensity in the middle of the wall jet.

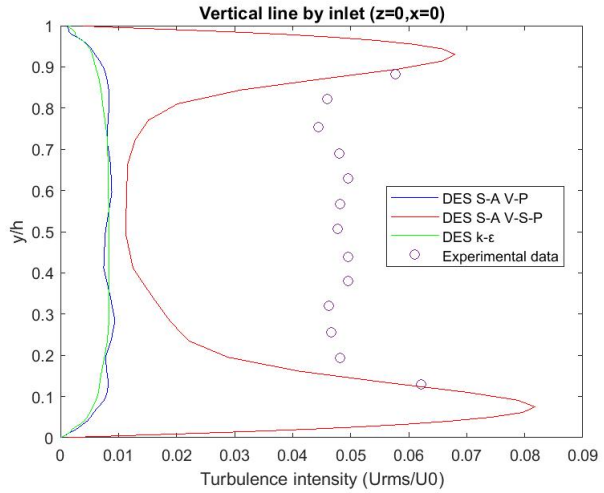

Figure 49: Turbulence intensity at vertical line of the cavity inlet with the different DES models of the fully turbulent case.

5.1.7 LES

LES approaches were investigated on the fully turbulent case as Taghinia et al. and Zasimova et al. [2, 3] achieved great success in predicting velocity profiles using LES. Various SGS were tested, including WMLES, WMLES $S-\Omega$, and dynamic Smagorinsky-Lilly. The LES approaches utilized the same averaging approach and time step as DES. Figure 50 displays the velocity profiles of the different LES SGS models, along with the results of Taghinia et al. [2]. D-S represents the dynamic Smagorinsky-Lilly model. At the horizontal ceiling line (y=h/2), WMLES over-predicts the velocity near the inlet, while WMLES $S-\Omega$ and dynamic Smagorinsky-Lilly under-predict it in that area. The dynamic Smagorinsky-Lilly model gives the best prediction at this line, but none of the models accurately predicts the secondary corner flow. At the vertical line x=H, the WMLES model produces a too steep velocity profile, whereas the dynamic Smagorinsky-Lilly model agrees best with the experimental data. Overall, the dynamic Smagorinsky-Lilly approach performs the best, as shown in table 33, which displays the RMSE values of the different LES approaches. However, none of the models performs as well as Taghinia et al. [2]. However, the results from Taghinia et al. are poor near the horizontal line close to the floor.

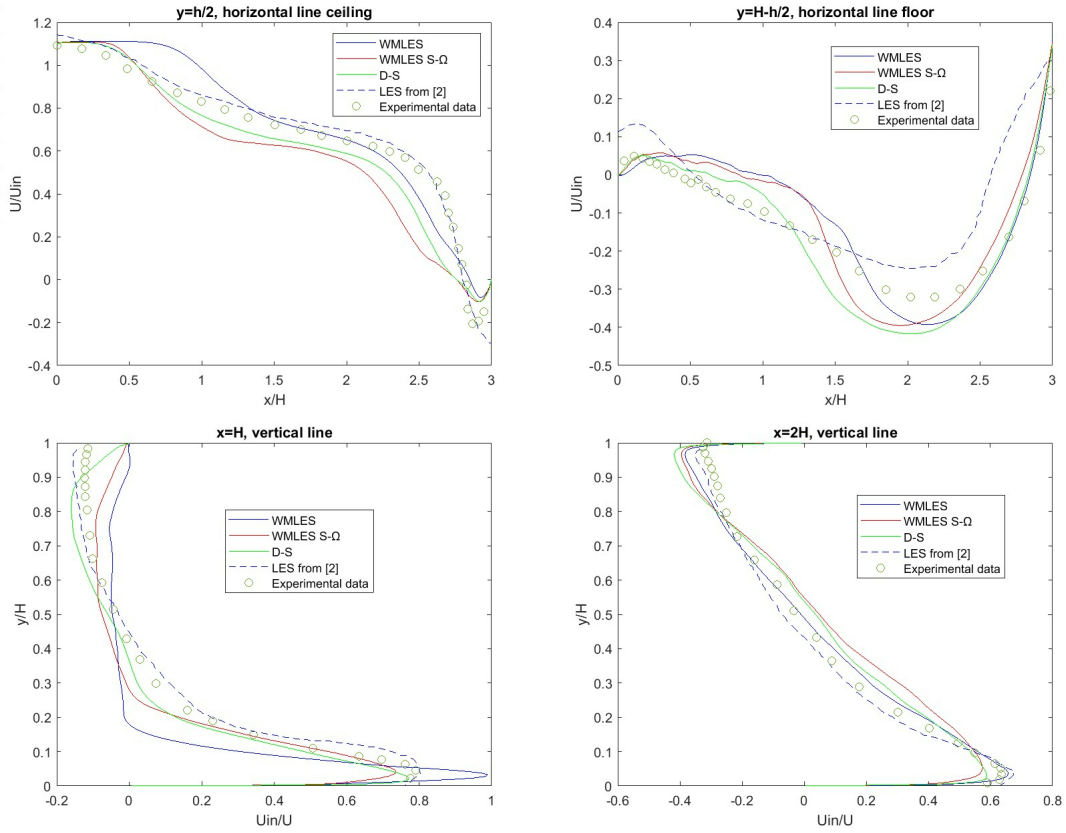

Figure 50: Velocity profiles of different LES SGS models on the fully turbulent case. Compared with the results obtained by Taghinia et al. [2] using LES

Figure 51 shows the turbulence intensity of the different LES SGS models at the vertical line of the cavity inlet. None of the LES SGS models can accurately predict the turbulence intensity at the inlet. All of the models underpredict the turbulence intensity at the inlet. The dynamic Smagorinsky-Lilly give similar behaviour to the DES Spalart-Allmaras with vorticity/strain-production based. Both models predict a high peak of turbulence intensity at the upper and lower walls of the inlet, which is typical for turbulent rectangular channel flow. The peak of the dynamic Smagorinsky model is slightly lower. Overall, the dynamic Smagorinsky model predicts the most accurate turbulence intensity, but still underestimates it by half.

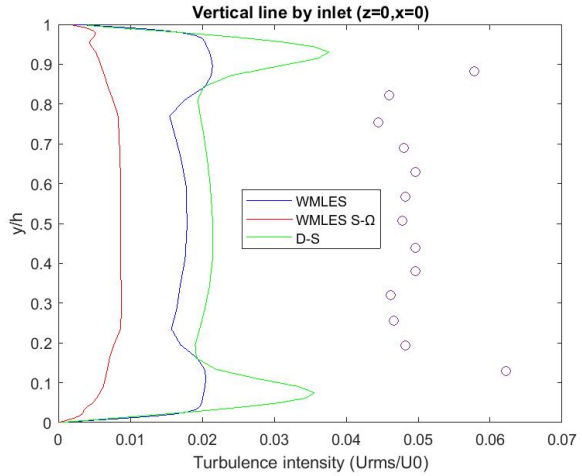

Figure 51: Turbulence intensity for the different LES SGS models at the vertical line of the inlet of the cavity of the fully turbulent benchmark.

To investigate if it was possible to get a higher turbulence intensity at the inlet of the cavity, leading to potentially better results, the turbulence intensity amount at the CFD inlet was investigated. In addition, the inlet duct length was extended by doubling the length. This is done as the perturbation at the CFD inlet will have space to develop into having the right amount of turbulence at the cavity inlet. The following turbulence intensities were tested on the CFD inlet: 4%, 10%, 20% and 50%. The LES subgrid model used was the dynamic Smagorinsky-Lilly SGS model with the vortex method used at the CFD inlet with 999 vortices used, as this was the model achieving the best results. The velocity profiles of the various LES settings together with the LES results obtained by Taghinia et al. [2], are given in figure 52. It can be observed that increasing the turbulence intensity, from 4% to 10% has a big impact on the velocity profiles, especially at the horizontal line by the ceiling and the vertical line x=H. Increasing the turbulence intensity makes the velocity profile less sharp as more turbulence is introduced into the flow, making the jet more dissipative. When the turbulence intensity is set to 50% the velocity is predicted extremely well at the area near the floor. Hence, having a turbulence intensity of 50% yields the best results as seen in table 34, showing the RMSE values of the different turbulence intensity settings. Using this amount of turbulence intensity leads to a velocity prediction which performs similarly to what Taghinia et al. [2] achieved.

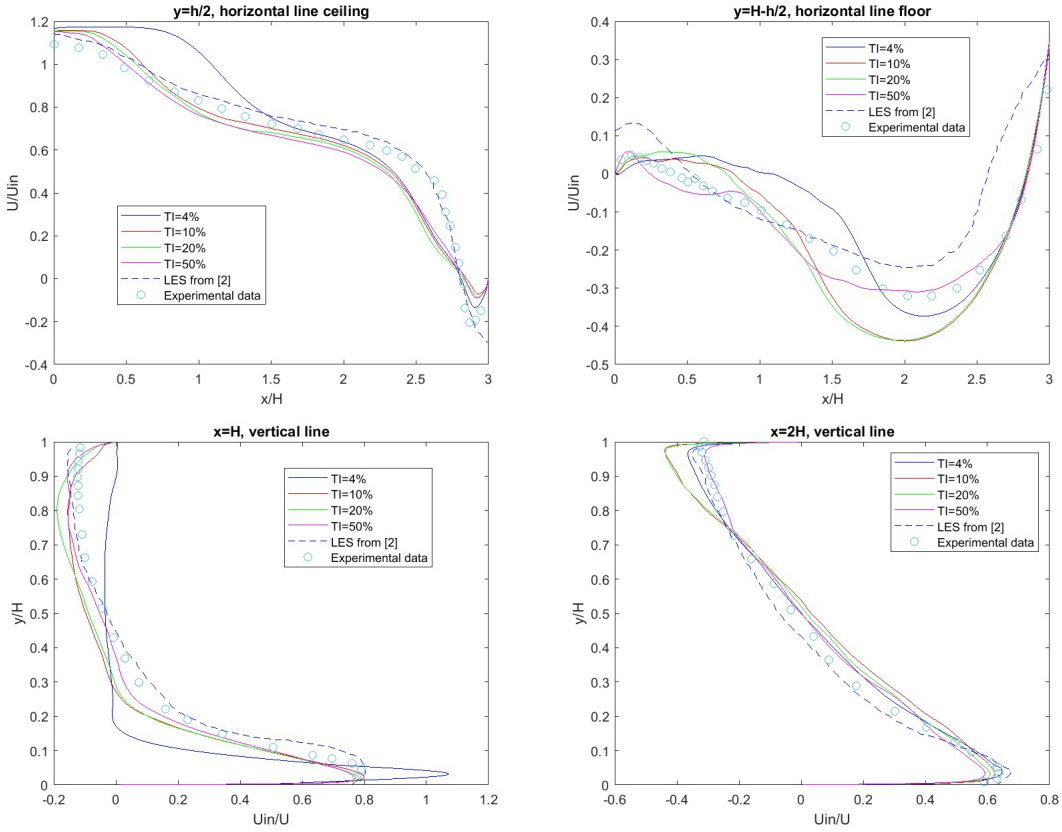

Figure 52: Velocity profiles when different turbulence intensities at the CFD inlet are used for the dynamic Smagorinsky-Lilly SGS model of the fully turbulent benchmark. In addition, the inlet duct length is doubled. Additionally, the velocity profiles from Taghinia et al. are given [2].

The turbulence intensity at the vertical line of the inlet of the cavity is shown in figure 53. It can be observed that increasing the turbulence intensity at the CFD inlet leads to an increasing turbulence intensity at the cavity inlet as expected. Resulting in a more accurate prediction of the turbulence intensity at the inlet of the cavity. However, the turbulence intensity at the upper and lower wall of the inlet seems to be over-predicted. This better prediction of the turbulence intensity results in the velocity profiles being predicted better.

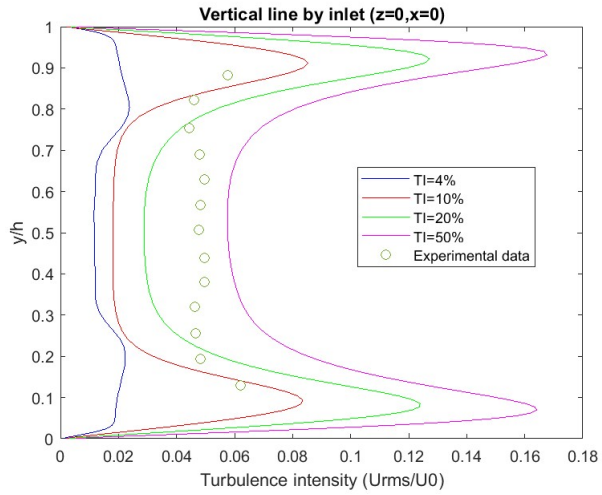

Figure 53: Turbulence intensity using different turbulence intensity settings at the CFD inlet for the Dynamic Smagorisnky-Lilly SGS model at the vertical line at the inlet of the cavity for the fully turbulent case.

To verify whether tuning the synthetic turbulence at the inlet, can result in a suitable inlet condition for the velocity profile entering the cavity, the inlet profile was compared with a DNS profile of a rectangular channel flow with a similar Reynolds number given by Moser et al.[5]. The resulting profiles of the u^+_{RMS} and y^+ values for the different turbulence intensities at the CFD inlet of the LES are shown in figure 54 compared with the results of Moser et al. [5]. It is evident that increasing turbulence intensity at the inlet causes the u^+_{RMS} peak to increase in size. By utilizing a turbulence intensity of 50% at the CFD inlet, a comparable profile to that achieved in Moser's DNS simulation can be obtained. Hence, it is almost possible to recreate the inlet condition of the cavity by using synthetic turbulence at the CFD with the correct amount of turbulence. This finding is significant as all LES and hybrid LES/RANS approaches in current literature uses an LES to create the inlet condition of the cavity before conducting the main simulation of airflow inside the cavity. This approach is computationally demanding, as an additional LES must be run to obtain the correct inlet condition. The results from this thesis indicate that it is possible to recreate this inlet condition by using the right amount of synthetic turbulence at the CFD inlet, reducing computational time and expenses.

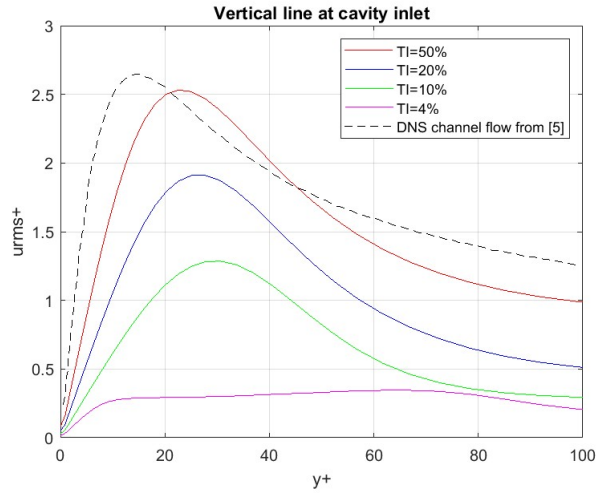

Figure 54: The y^+ and u^+_{RMS} profiles from the LES dynamic Smagorinsky-Lilly with different turbulence intensities specified at the CFD inlet for the fully turbulent case. Compared with DNS results for a rectangular channel flow of a similar Reynolds number from Moser et al. [5].

Figure 55 shows the RMS velocity values for various turbulence intensities at the CFD inlet. The RMS velocity profiles are compared with both the experimental data and the results obtained from Taghinia et al. [2]. Upon observation, it can be noted that none of the predicted RMS velocity profiles provides an excellent match compared to the experimental data. However, the profile obtained from Taghinia et al. offers a better fit in comparison to the experimental data. At the ceiling's horizontal line, the profile obtained from a turbulence intensity of 4% differs from the other profiles. The other profile, although able to predict the shape relatively well, predicts the wrong RMS values. At the floor's horizontal line, the RMS values are underpredicted, except for the area close to the outlet where it is overpredicted. At the vertical line x=2H, the RMS values are underpredicted for all of the different turbulence intensities at the CFD inlet.

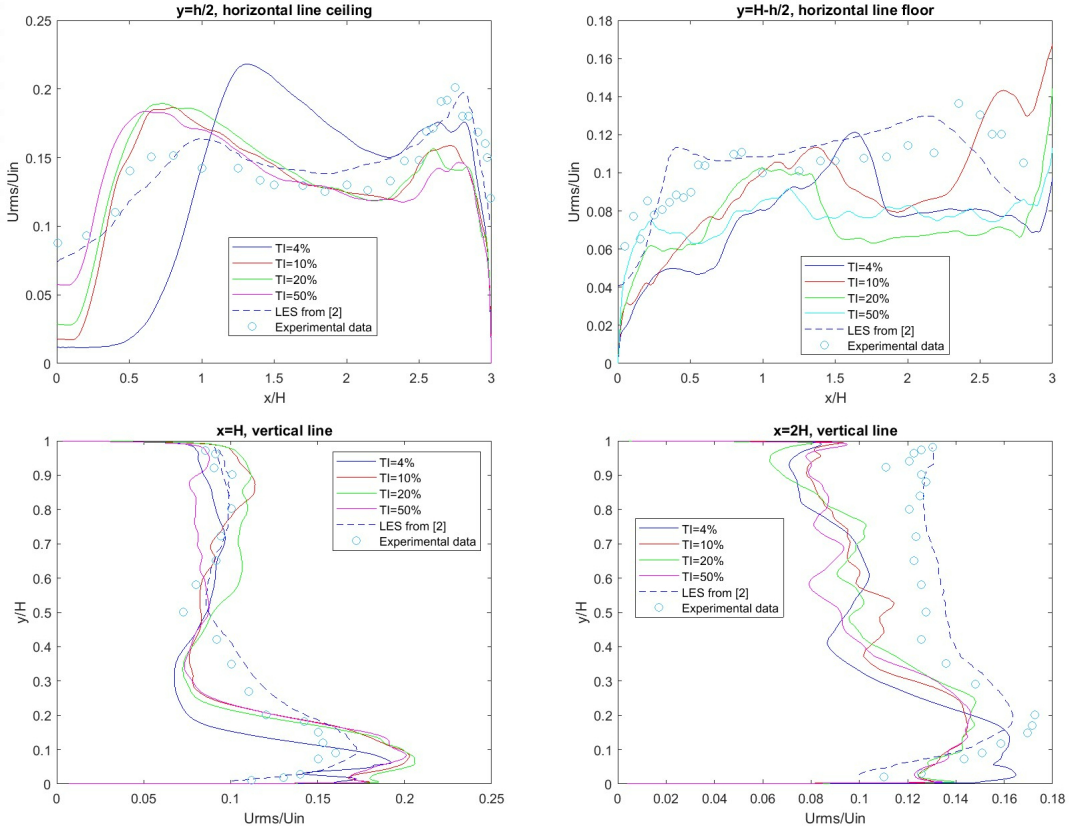

Figure 55: RMS velocity profiles with the different turbulence intensity settings for the dynamic Smagorinsky-Lilly approach for the fully turbulent case. Compared with the experimental data and the results obtained from Taghinia et al.[2].

The same setup, with the same turbulence intensities at the CFD inlet, was also investigated with the DES Spalart-Allmaras approach. However, for cases with a turbulence intensity of 10% or higher, simulations diverged after a few timesteps. On the other hand, simulations did not diverge for a turbulence intensity of 4%. Therefore, the stability of a DES appears to be sensitive to the amount of synthetic turbulence applied at the inlet. Consequently, the DES is unable to produce the same results as the LES using the same amount of synthetic turbulence at the inlet, which is a significant disadvantage when using DES for cavity flows.

5.1.8 Comparing the turbulence models

In analyzing the fully turbulent benchmark, it has been determined that the most accurate RANS model to use is the default standard $k-\epsilon$ model. The DES model giving the best results is the DES realizable $k-\epsilon$ model with the vortex method used at the inlet for synthetic turbulence. Meanwhile, for LES, the dynamic Smagorinsky-Lilly SGS model with a modification of the turbulence intensity

to 50% at the CFD inlet is the most suitable approach for this benchmark. Figure 56 displays the velocity profiles of these turbulence modelling methods. It is worth noting that while the RANS model produces the most accurate velocity profile at the ceiling, none of the approaches accurately predict the secondary vortex at the corner. The DES and LES offer the best agreement at the line by the floor. The profile of the DES at the vertical line x=3H is too sharp. Overall, the LES demonstrates the best agreement, as evidenced by the RMSE values in table 15. It is noteworthy that the DES simulation setup could not replicate the LES simulation setup due to divergence issues encountered while attempting to introduce the same synthetic turbulence at the inlet.

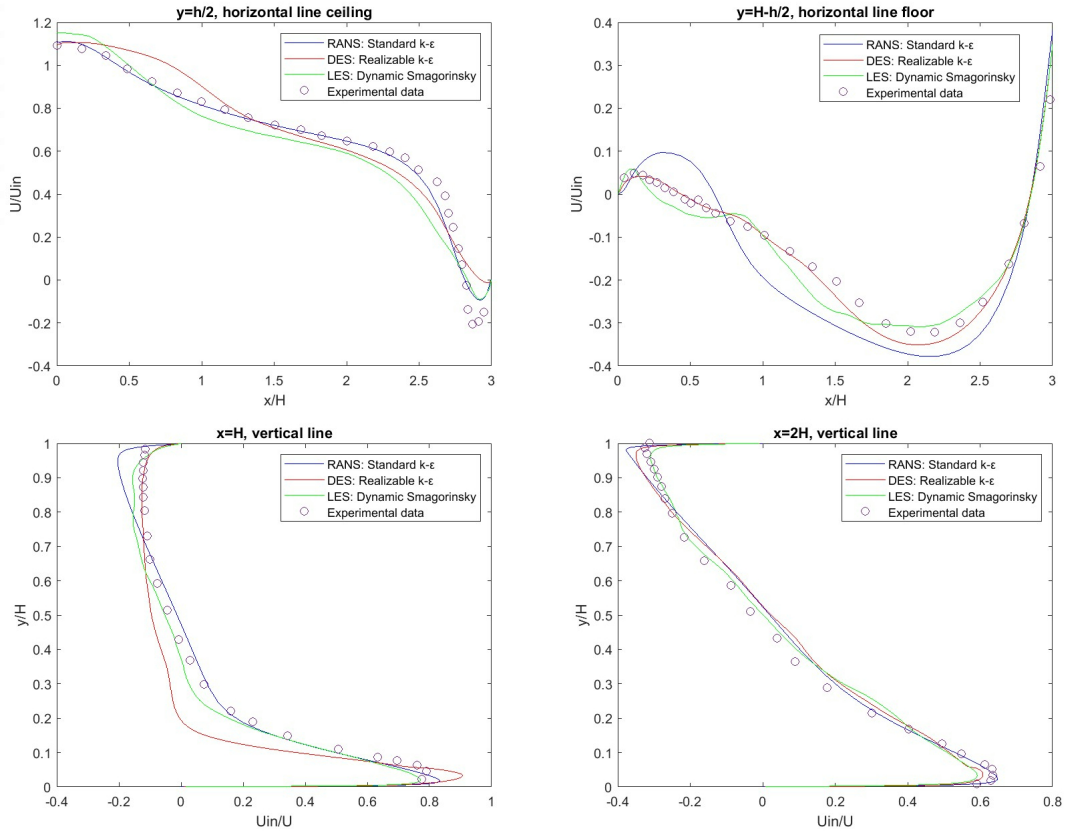

Figure 56: Velocity profiles of the most accurate RANS model, LES and DES approaches of the fully turbulent case.

Table 15: RMSE values of the most accurate RANS model, LES and DES approaches of the fully turbulent case.

	Horizontal line ceiling (y=h/2)	Horizontal line floor (y=H-h/2)	Vertical line x=3H	Vertical line x=6H	Average
RANS:	0.0669	0.0748	0.0565	0.0691	0.0668
DES:	0.1043	0.0254	0.1091	0.0707	0.0774
LES:	0.1063	0.0337	0.0508	0.0714	0.0656

5.2 Transitional case

For the transitional case, two different flow scenarios where the Reynolds number is 2500 and 1000 are further investigated on the same geometry. Both Reynolds numbers resulted in transitional flow inside the cavity as examined by Van Hooff et al. [18].

5.2.1 Grid sensitivity analysis for RANS

To optimize the mesh for the remaining RANS and URANS simulations, a grid sensitivity analysis was performed on the transitional case. The coarsest mesh was selected to ensure that the maximum y^+ value did not exceed 5. To determine the y^+ values, a RANS simulation was conducted using the standard $k-\omega$ model, which proved to be the best RANS model for this benchmark in Bjuri's specialization project [11]. The RANS simulation was run on the case with a Reynolds number of 2500, as this would be the limiting case leading to the highest y^+ values. The y^+ values of the coarsest mesh are presented in table 16, with a maximum value of 8. However, the average value stays below 5, indicating that the error is negligible.

Table 16: The y^+ values at the walls of the transitional case with a Reynolds number of 2500 for the standard $k-\omega$ model.

	Ceiling	Floor	Inlet wall	Outlet wall	Left/right wall
Max	3.915	5.320	4.695	8.476	6.427
Average	1.133	1.603	1.696	1.243	0.5024

This resulted in the coarsest mesh consisting of 656 000 nodes. For each refinement of the mesh, a factor of $2\sqrt{2}$ was used, which resulted in the medium mesh consisting of 1 820 000 nodes and the finest mesh consisting of 5 459 000 nodes. The resulting velocity profiles when the Reynolds number is 2500 are given in figure 57. It can be observed that the velocity profiles differ slightly. For the rest of the RANS simulations, the medium mesh consisting of 1 820 000 nodes is used, as this mesh does not differ too much from the finest mesh and has the benefit of being less computationally expensive.

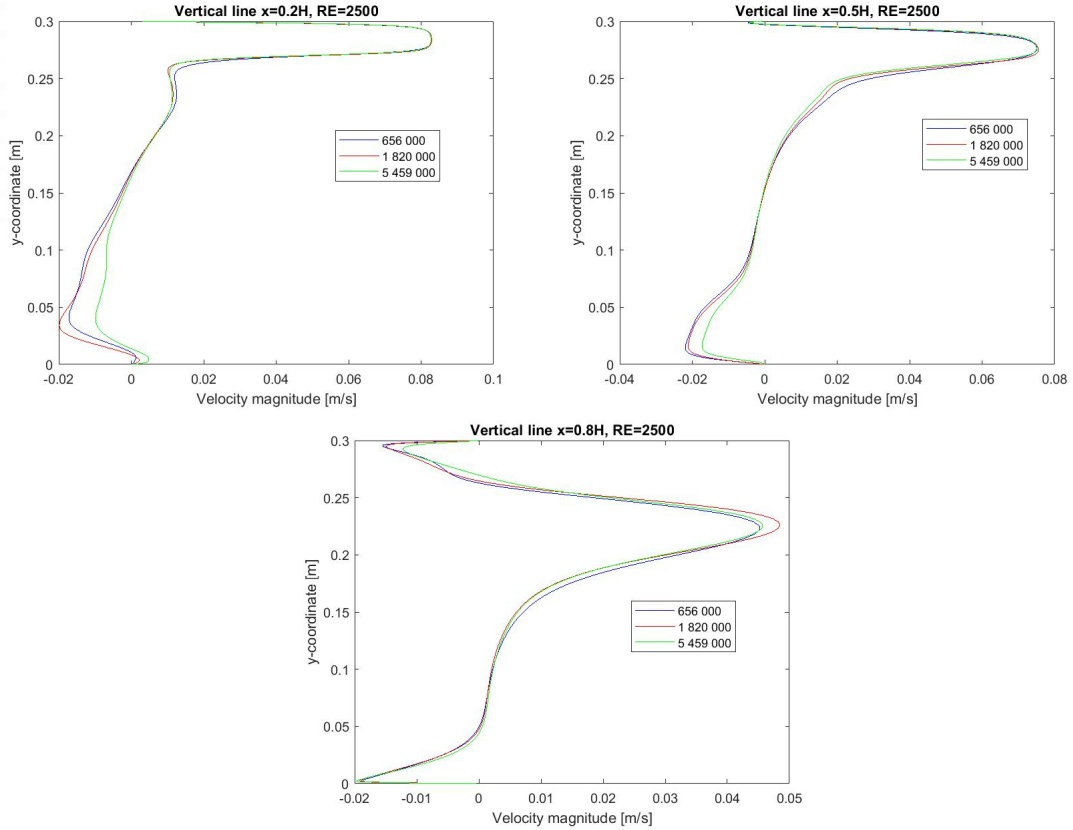

Figure 57: Grid sensitivity analysis when the standard $k-\omega$ model is used on the transitional case with a Reynolds number of 2500.

Figure 58 shows the velocity profiles of the grid sensitivity analysis when the Reynolds number is 1000. There are some remarkable differences between the velocity profiles of the different meshes. As the number of nodes increases, the negative velocity near the floor also increases for the vertical line x=0.2H and x=0.5H. Moreover, as the mesh becomes more refined, the velocity peak shifts downwards and increases in magnitude at the lines x=0.5H and x=0.8H. Using the medium mesh when the Reynolds number is 1000, does not give too big errors compared to using the finest mesh, which is more computationally expensive. Hence the medium mesh is also used when the Reynolds number is 1000.

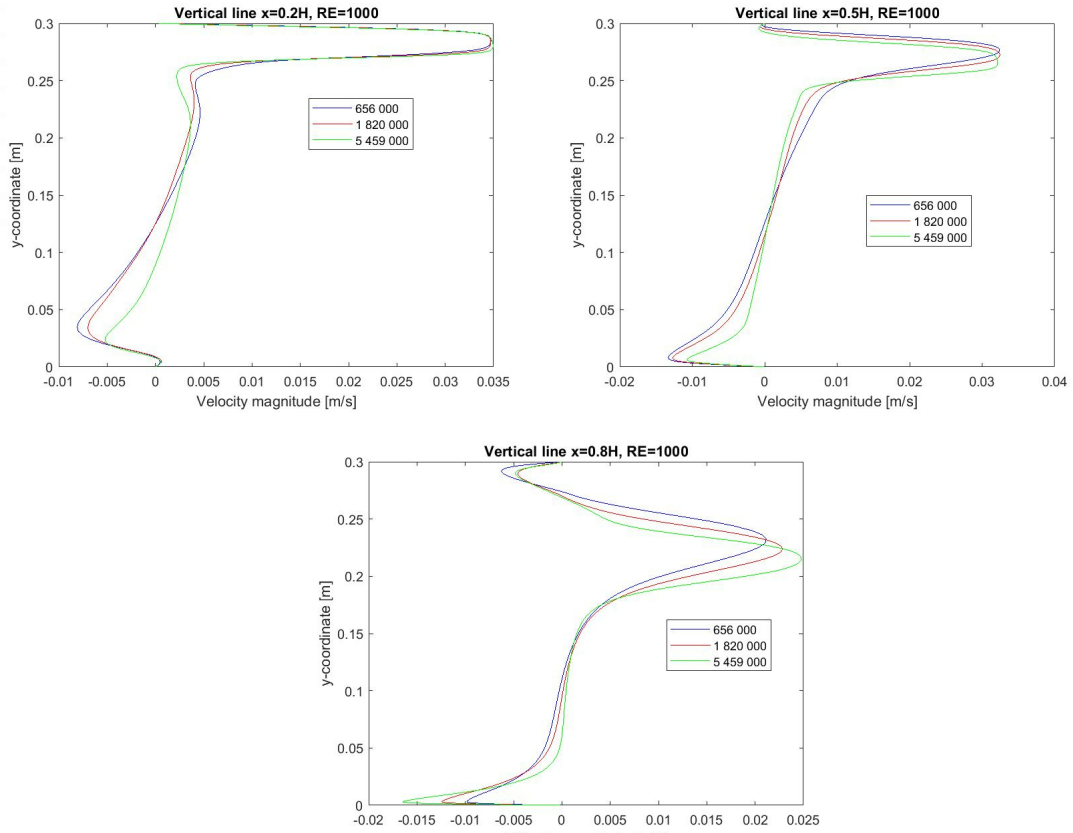

Figure 58: Velocity profiles of the transitional benchmark with a Reynolds number of 1000, when a grid sensitivity analysis is conducted for the standard $k-\omega$ model.

5.2.2 RANS simulations

For the transitional case, the same RANS models were used as for the fully turbulent case. In Figure 59, the velocity profiles of the $k-\epsilon$ models and the Spalart-Allmaras model are shown for a Reynolds number of 2500. It is evident that the $k-\epsilon$ models all display similar behaviour in predicting detachment too late. This leads to a velocity peak that is too close to the ceiling and results in significant errors at the vertical line x=0.8H. On the other hand, the Spalart-Allmaras model accurately predicts the location of the detachment point well, resulting in much-improved velocity profiles compared to the $k-\epsilon$ models.

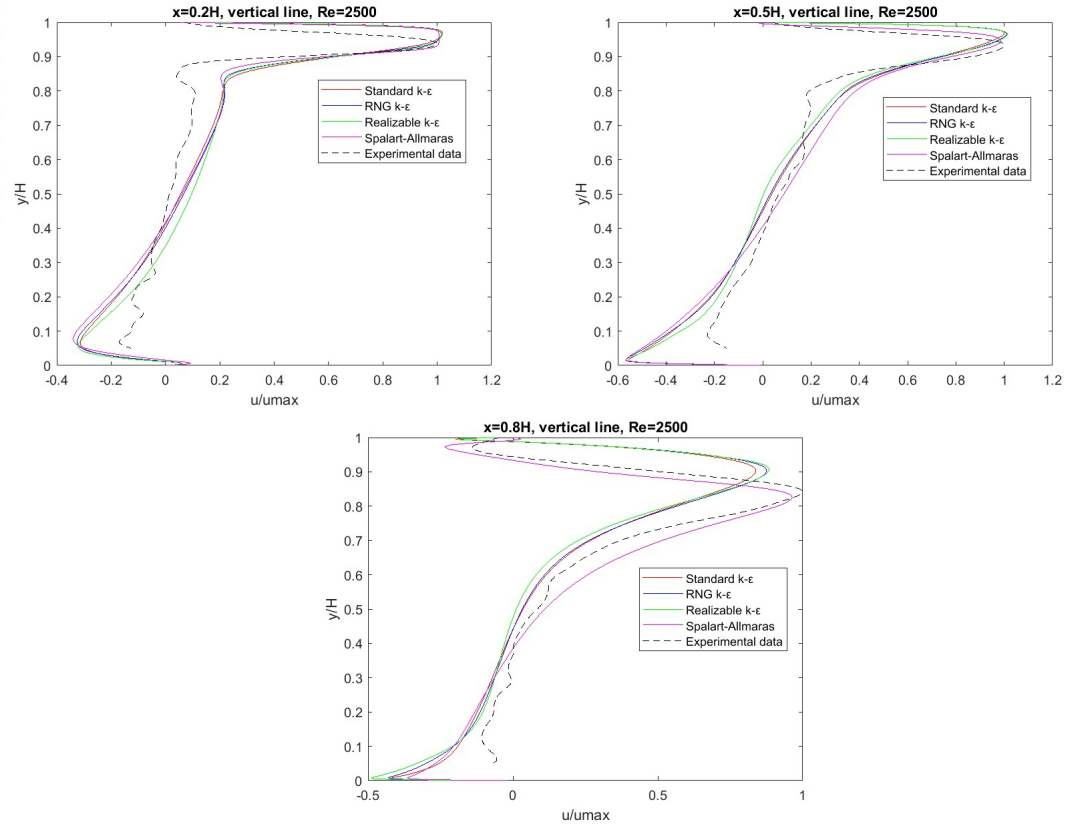

Figure 59: Velocity profiles of the default $k-\epsilon$ models and the Spalart-Allmaras model for the transitional case with a Reynolds number of 2500.

In figure 60, the velocity profiles of the $k-\omega$ models are presented. It is evident that the BSL $k-\omega$ model accurately predicts both the location and velocity magnitude of the peak at all lines. In contrast, the other $k-\omega$ models predict detachment too early, resulting in a velocity peak that is inaccurately close to the floor at the vertical line x=0.8H. On the other hand, the $k-\epsilon$ models predict detachment too late, causing the peak of the wall jet to be closer to the ceiling. Upon comparing the velocity profiles of this study with the study of Van Hooff et al. [46], it can be observed that in both studies, the velocity profiles from the SST $k-\omega$ model are too close to the floor. However, in the study by Van Hooff et al., the velocity magnitude is not as underpredicted compared to this study.

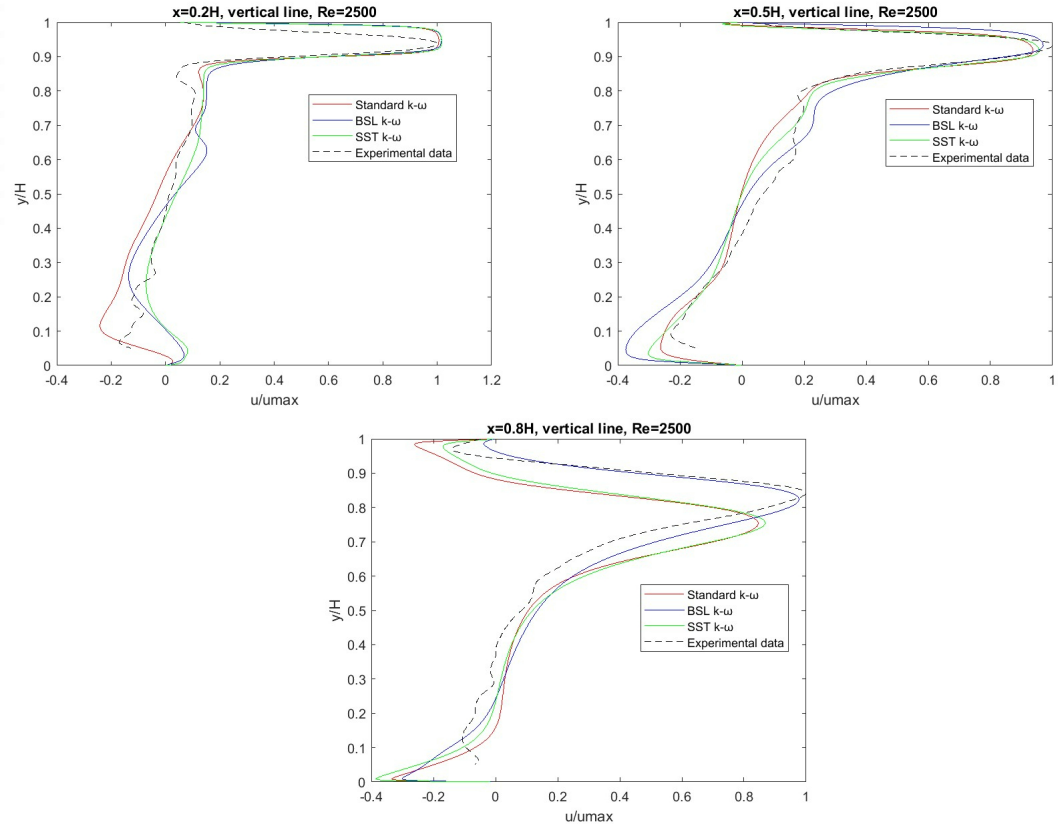

Figure 60: Velocity profiles of the default $k-\omega$ models for the transitional case with a Reynolds number of 2500.

Table 17 provides the RMSE values for the various RANS models at different vertical lines for the transitional benchmark with a Reynolds number of 2500. The table reveals that the $k-\omega$ models have a lower error compared to the $k-\epsilon$ models. Among the $k-\omega$ models, the BSL model has the least amount of error while the Spalart-Allmaras model also performs well. However, most models struggle to accurately predict the velocity profile at the line x=0.8H due to improper detachment point prediction, resulting in significant errors at this line.

Table 17: RMSE values of the various default RANS models for the transitional benchmark with a Reynolds number of 2500.

	Vertical line x=0.2H	Vertical line x=0.5H	Vertical line x=0.8H	Average
BSL $k-\omega$	0.1314	0.0968	0.0813	0.1032
SST $k-\omega$	0.1241	0.0544	0.2348	0.1378
Standard $k-\omega$	0.1247	0.063	0.2522	0.1466
RNG $k-\epsilon$	0.1518	0.1421	0.2149	0.1696
Realizable $k-\epsilon$	0.1507	0.1361	0.2238	0.1702
Standard $k-\epsilon$	0.1530	0.1417	0.2092	0.1680
Spalart-Allmaras	0.1456	0.1139	0.0967	0.1187

Looking at the velocity profiles in figure 61 for the case where the Reynolds number is 1000. It can be noticed that also for this case the $k-\epsilon$ models predict a velocity profile close to the ceiling due to the late detachment point. While the Spalart-Allmaras model can predict the velocity profiles with good accuracy. After comparing the results with those obtained by Bjerkeli [1], as shown in figure 27, it is apparent that both the standard $k-\epsilon$ and the RNG $k-\epsilon$ models predict the peak too close to the ceiling, which is also observed in this thesis. However, the velocity profiles in Bjerkeli's master thesis are overpredicted when compared to the ones collected in this study. Additionally, the realizable $k-\epsilon$ model detaches too early in Bjerkeli's master thesis, resulting in a velocity profile that is too close to the floor, which is not the case in this thesis. Therefore, it

appears that the mesh is influencing the performance of the RANS models.

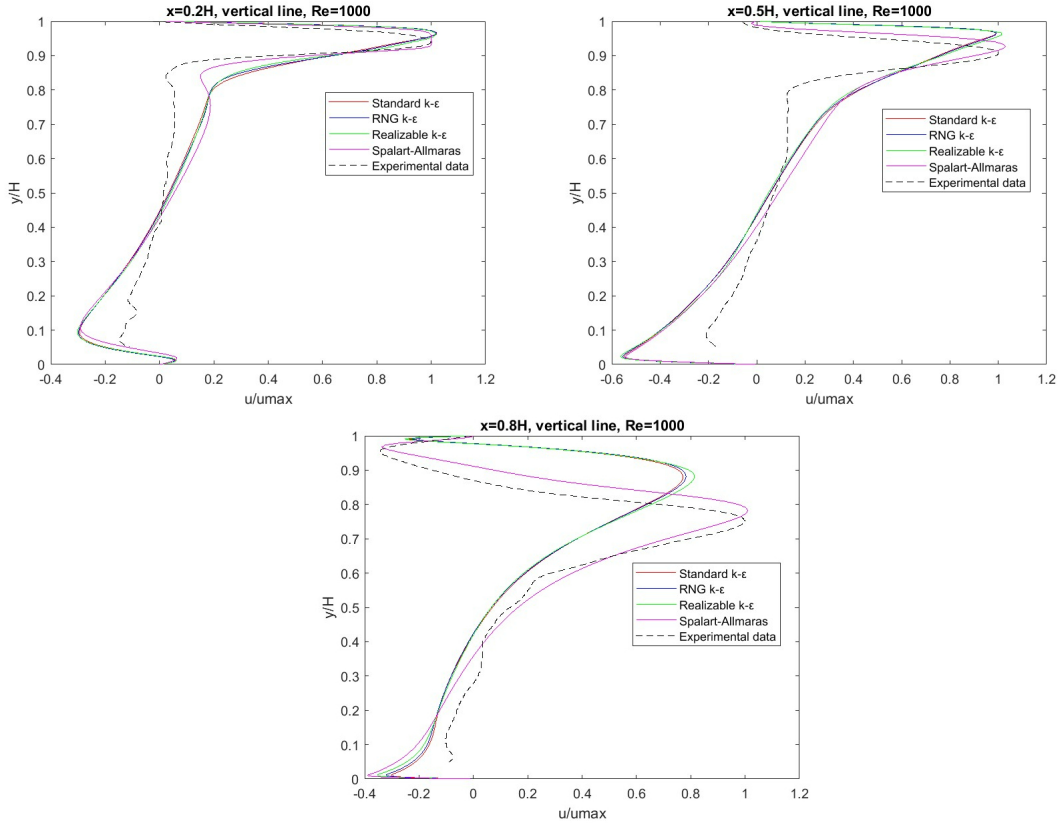

Figure 61: The velocity profiles for the $k-\epsilon$ models and the Spalart-Allmaras model of the transitional benchmark with a Reynolds number of 1000.

The velocity profiles of the $k-\omega$ models for the case with a Reynolds number of 1000 are given in figure 62. It is evident that also for this case the $k-\omega$ models perform better overall compared to the $k-\epsilon$ models. The SST $k-\omega$ and BSL $k-\omega$ models exhibit similar velocity profiles, while the standard $k-\omega$ model performs better at all vertical lines. At the vertical line x=0.8H, the standard $k-\omega$ model accurately predicts the velocity peak's location but slightly overestimates it. On the other hand, the BSL $k-\omega$ and SST $k-\omega$ models underestimate the velocity magnitude and predict the detachment point earlier, resulting in the peak being closer to the floor. Comparing these results with the one from Van Hooff et al. [46], it is apparent that the SST $k-\omega$ model behaves similarly in this thesis compared to the study of Van Hooff et al.

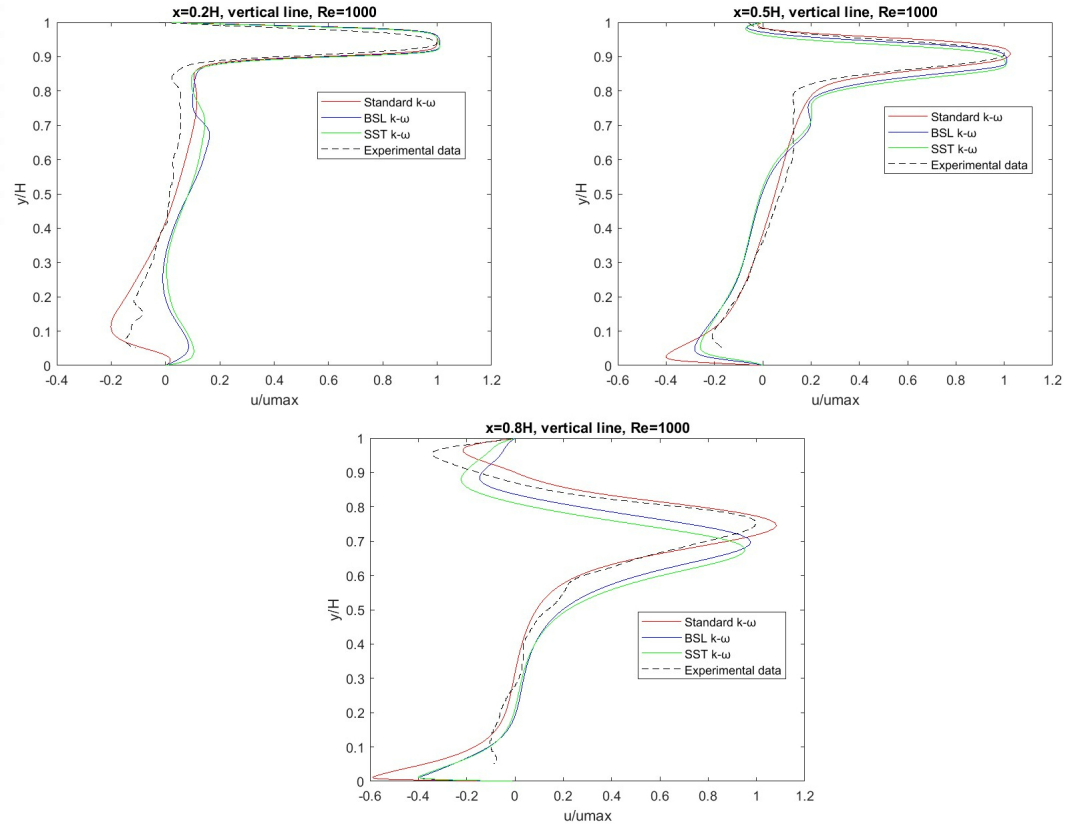

Figure 62: The velocity profiles for the $k-\omega$ models of the transitional benchmark with a Reynolds number of 1000

The predicted turbulent kinetic energy plots at the wall jet at the two vertical lines x=0.2H and x=0.5H are given in figure 63. The $k-\epsilon$ models tend to overpredict the turbulent kinetic energy by a factor of approximately 6 at x=0.5H, and even more at x=0.2H. On the other hand, the $k-\omega$ model provides a significantly better prediction. Despite this, none of the RANS models can accurately predict the turbulent kinetic energy profiles. Also in Van Hooff et al. [46], studies the RANS models were not able to predict the turbulent kinetic energy profiles with good accuracy. This aligns with the velocity plots, as an excessively high turbulent kinetic energy can cause the flow to remain attached to the ceiling for a longer duration, leading to an incorrect prediction of the velocity peak, which occurs too close to the ceiling. For the case where the Reynolds number is 2500, a similar behaviour is observed as can be observed in figure 92.

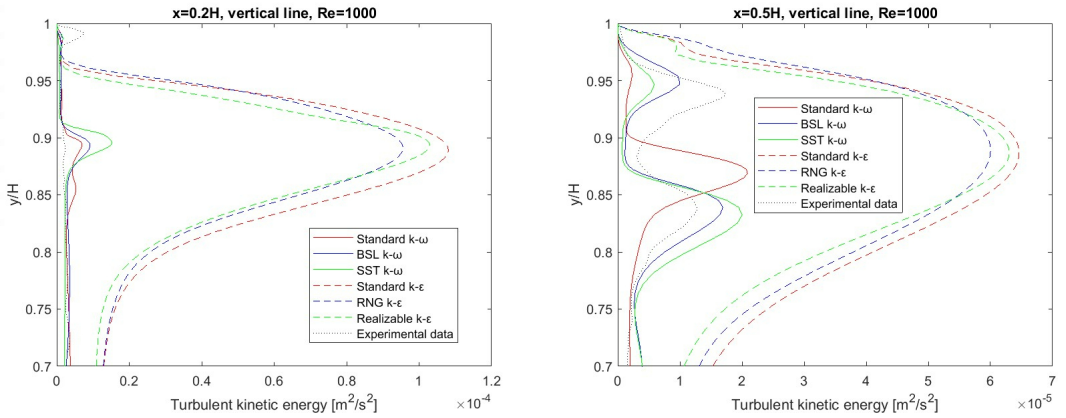

Figure 63: Turbulent kinetic energy plots of the various default RANS models on the transitional benchmark with a Reynolds number of 1000.

The RMSE values of the velocity profiles obtained from the different turbulence models are given in table 18. It can be observed that also for this Reynolds number the $k-\omega$ models and the Spalart-Allmaras model give a much better performance than the $k-\epsilon$ models. This is expected, as examined in the velocity profiles. In particular, the standard $k-\omega$ model gives the overall least error. Comparing the RMSE values between the case with a Reynolds number of 1000 and 2500, it can be concluded that the $k-\epsilon$ models have even greater errors when the Reynolds number is 1000 compared to 2500. Comparing the RMSE value with the ones obtained by Bjerkeli [1], it can be observed that Bjerkli achieve much less RMSE values for all of the default RANS models compared to what was the case in this thesis.

Table 18: RMSE values of the default RANS models on the transitional benchmark with a Reynolds number of 1000.

	Vertical line x=0.2H	Vertical line x=0.5H	Vertical line x=0.8H	Average
BSL $k-\omega$	0.1063	0.0915	0.1751	0.1243
SST $k-\omega$	0.1092	0.1247	0.2398	0.1579
Standard $k-\omega$	0.0667	0.0497	0.0810	0.0658
RNG $k-\epsilon$	0.1351	0.2079	0.3548	0.2326
Realizable $k-\epsilon$	0.1292	0.2042	0.3592	0.2309
Standard $k-\epsilon$	0.1355	0.2131	0.3219	0.2235
Spalart-Allmaras	0.1081	0.1453	0.1385	0.1306

5.2.3 Wall treatment approaches

The same wall treatment techniques tested out for the fully turbulent benchmark were also applied on the transitional case. When refining the boundary layer the medium mesh consisting of 1 820 000 nodes where used, while a mesh consisting of 496 000 nodes was used when employing wall functions. This is equivalent to a 73 % reduction in the mesh size, which will give less computational effort. The meshes utilized are shown in figure 64.

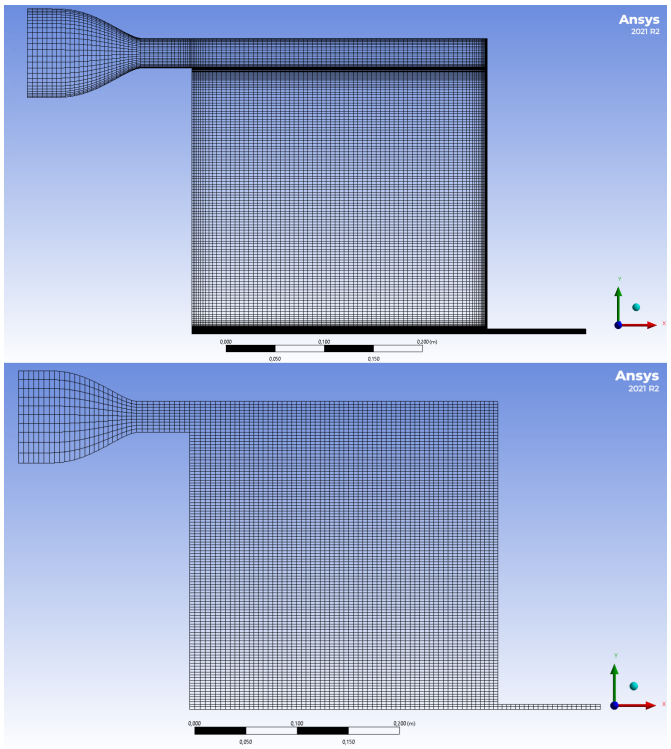

Figure 64: Meshes used for the different wall treatment approaches. The upper mesh uses the enhanced wall treatment consisting of 1 820 000 nodes, which resolves the boundary layer. The lower mesh utilizes wall functions consisting of 496 000 nodes.

In the transitional case with a Reynolds number of 2500, Figure 65 shows the different wall treatment methods used for the RNG $k-\epsilon$ model. The outcomes suggest that the standard wall function predicts the location of the velocity peak more precisely at the x=0.8H line compared to other approaches. However, it underestimates the velocity magnitude. The wall treatment methods behave similarly on both the standard $k-\epsilon$ and realizable $k-\epsilon$ model. Moreover, they produce similar results when applied to the case with a Reynolds number of 1000, as seen in the velocity profiles of the realizable $k-\epsilon$ model in Figure 93. This implies that the standard wall function not only reduces the simulation computational cost but also provides more accurate velocity profiles for the $k-\epsilon$ models. Despite that, the $k-\epsilon$ models with standard wall function are still outperformed by the default $k-\omega$ models.

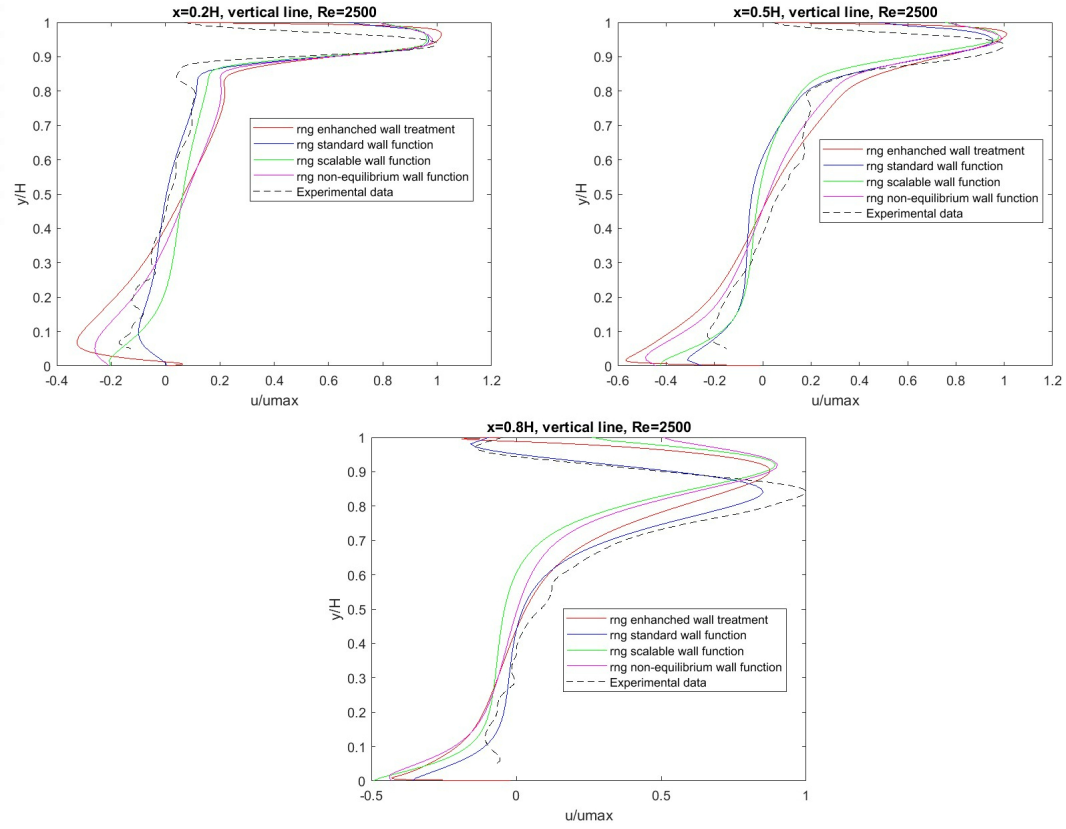

Figure 65: Velocity profiles when using different wall treatment approaches on the RNG $k-\epsilon$ model, on the transitional case with a Reynolds number of 2500.

Figure 66 shows the turbulent kinetic energy plots for the different wall treatment approaches of the realizable $k-\epsilon$ method on the transitional case with a Reynolds number of 1000. The plots reveal that utilizing wall functions reduces the turbulence kinetic energy in the wall jet. When comparing the standard wall function to the enhanced wall treatment, the turbulent kinetic energy decreases by over 50%. This reduction in kinetic energy causes the flow to detach earlier, leading to the velocity peak of the jet being closer to the floor. Consequently, better predictions can be achieved, particularly on the line x=0.8H. Similar observations can be made from the turbulent kinetic energy profiles of the case with a Reynolds number of 2500.

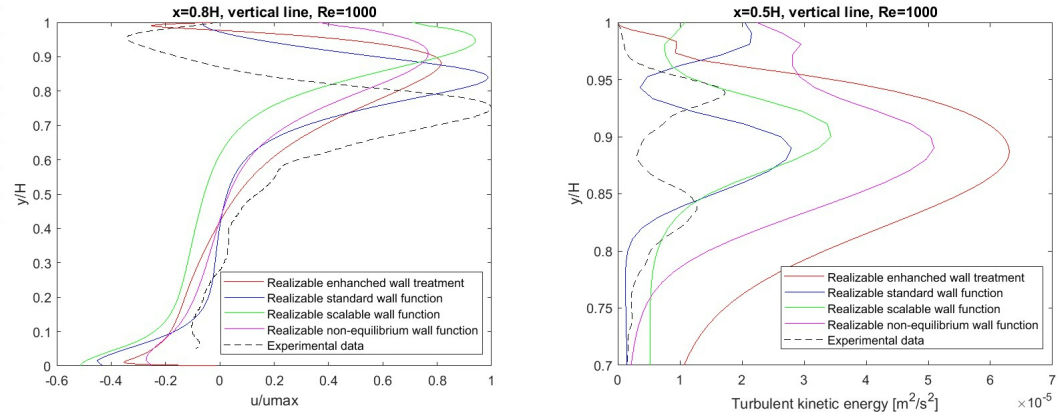

Figure 66: The turbulent kinetic energy from different wall treatment approaches on the realizable $k-\epsilon$ model on the transitional case with a Reynolds number of 1000.

5.2.4 Correctors and other options for RANS

The same correctors and RANS options tested out on the fully turbulent case, were also investigated on the transitional flow benchmark. The low-Re corrector gave a more precise prediction of the velocity profile on the transitional benchmark for the SST $k-\omega$ and the standard $k-\omega$ model with a Reynolds number of 2500. The velocity profile obtained from several corrector options on the SST $k-\omega$ model for a Reynolds number of 2500 is shown in figure 67. The low-Re corrector accurately predicted the velocity profile at the vertical line x=0.8H and improved upon the SST $k-\omega$ model with default settings. This was also true for a Reynolds number of 1000, as seen in figure 94. However, the low-Re corrector did not improve the standard $k-\omega$ and BSL $k-\omega$ model at a Reynolds number of 1000. In fact, it gave worse results for the BSL $k-\omega$ model and should not be used on this model for transitional flow. However, for the BSL $k-\omega$ model, the corner corrector option gave a minor improvement.

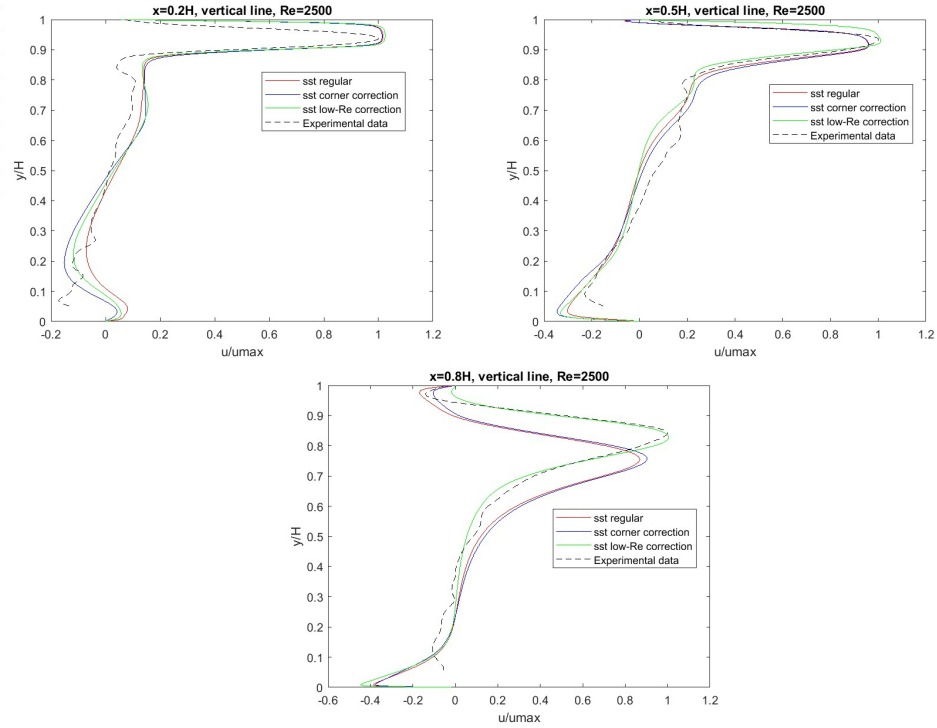

Figure 67: Velocity profile when using different correctors in Fluent of the SST $k-\omega$ model on the transitional case with a Reynolds number of 2500.

Figure 68 displays the velocity profiles generated by various options for the Spalart-Allmaras model with a Reynolds number of 1000, with abbreviations matching those in table 14. The results indicate that vorticity/strain-based production offers slightly better accuracy, with a slightly improved velocity peak prediction. However, for a Reynolds number of 2500, this option produces worse velocity field predictions, as illustrated in figure 95. Therefore, one should be cautionious when using the vorticity/strain-based production setting on a transitional flow. All other RANS correctors and options tested did not show significant improvements compared to the default settings.

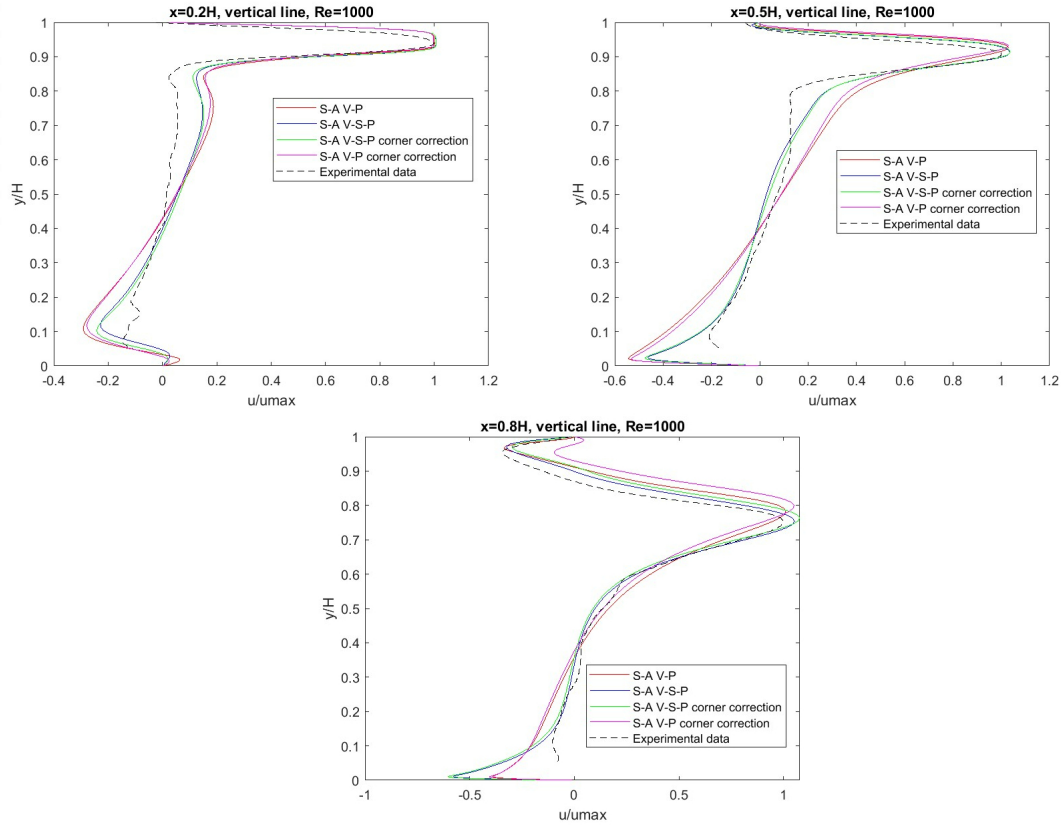

Figure 68: Velocity profile when using different correctors and other options in Fluent of the Spalart-Allmaras model on the transitional case with a Reynolds number of 1000.

After utilizing the corrector options and wall functions, we were able to optimize the RANS models and obtain the RMSE values for a Reynolds number of 2500 and 1000 respectively. Table 19 and 20 display the results of the optimized RANS models. The SST $k-\omega$ model with the low-Re corrector had the least error for a Reynolds number of 2500. However, there was not much difference in the RMSE values between all of the optimized RANS models. On the other hand, when it came to a Reynolds number of 1000, the optimized $k-\epsilon$ models that utilized wall functions had significantly higher errors in comparison to the $k-\omega$ models and the Spalart-Allmaras model. The standard $k-\omega$ model gave the best performance for the case with a Reynolds number of 1000.

Table 19: RMSE values of optimized RANS models on the transitional benchmark with a Reynolds number of 2500. The bold text shows the RANS models improved by utilizing correctors, wall functions or other options in Fluent.

	Vertical line x=0.2H	Vertical line x=0.5H	Vertical line x=0.8H	Average
BSL $k-\omega$	**0.1233**	**0.1073**	**0.0658**	**0.0988**
SST $k-\omega$	**0.1240**	**0.0996**	**0.0538**	**0.0925**
Standard $k-\omega$	**0.1329**	**0.1159**	**0.1127**	**0.1205**
RNG $k-\epsilon$	**0.1180**	**0.1258**	**0.0642**	**0.1027**
Realizable $k-\epsilon$	**0.1302**	**0.1208**	**0.1045**	**0.1185**
Standard $k-\epsilon$	**0.1421**	**0.1302**	**0.1622**	**0.1448**
Spalart-Allmaras	0.1456	0.1139	0.0967	0.1187

Table 20: RMSE values of optimized RANS models on the transitional benchmark with a Reynolds number of 1000. The bold text shows the RANS models improved by utilizing correctors, wall functions or other options in Fluent.

	Vertical line x=0.2H	Vertical line x=0.5H	Vertical line x=0.8H	Average
BSL $k-\omega$	**0.1097**	**0.0918**	**0.1541**	**0.1185**
SST $k-\omega$	**0.0801**	**0.0775**	**0.1085**	**0.0887**
Standard $k-\omega$	0.0667	0.0497	0.0810	0.0658
RNG $k-\epsilon$	**0.0889**	**0.1697**	**0.3562**	**0.2049**
Realizable $k-\epsilon$	**0.0931**	**0.1577**	**0.3376**	**0.1961**
Standard $k-\epsilon$	**0.0947**	**0.1699**	**0.3487**	**0.2044**
Spalart-Allmaras	**0.0822**	**0.0716**	**0.0825**	**0.0787**

5.2.5 URANS

URANS simulations were conducted on the transitional benchmark using the optimized RANS models. A time step of 0.01 seconds was used for the case with a Reynolds number of 2500, as it proved to be sufficient in a time sensitivity analysis for the DES approach. Similarly, a time step of 0.025 seconds was used for the case with a Reynolds number of 1000. The simulations were averaged until they reached statistical steady state and were averaged over a sufficient time to obtain independent flow statistics. Figure 69 shows the RANS and URANS simulation velocity profiles of the RNG $k-\epsilon$ method for the transitional case with a Reynolds number of 2500. Both RANS and URANS predict similar velocity profiles, but URANS performs slightly better in predicting the velocity magnitude at the velocity peak on the line x=0.8H, as shown in table 39, which displays the RMSE values of the URANS and RANS of the RNG $k-\epsilon$ model. For the other optimized RANS models for the case with a Reynolds number of 2500, the URANS performs similarly or worse than the RANS.

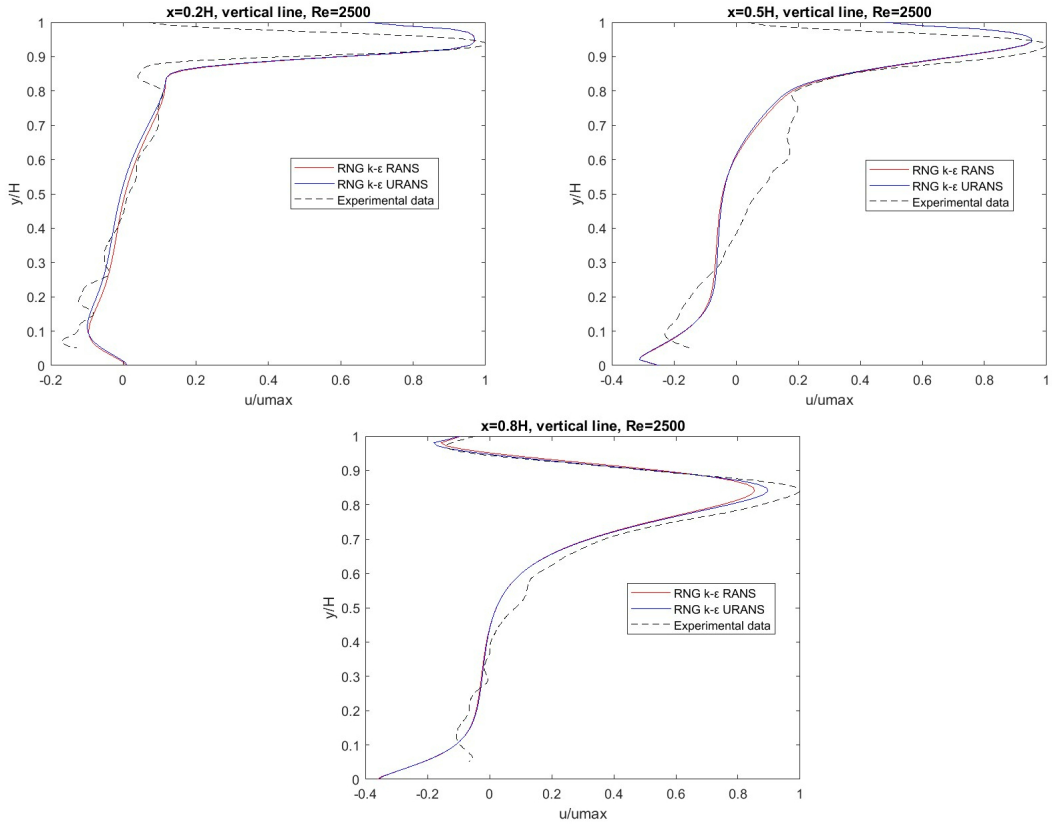

Figure 69: Velocity profiles of RANS and URANS simulation of the optimized RNG $k-\epsilon$ model of the transitional case with a Reynolds number of 2500.

In the transitional case with a Reynolds number of 1000, figure 70 displays the velocity profiles for the optimized standard $k-\omega$ model using both RANS and URANS. Upon observation, it is evident that URANS performs similarly to RANS, but with slightly worse results. This trend is also observed in other optimized RANS models for the same case. The findings are consistent with the fully turbulent case, indicating that running URANS simulations does not provide any added benefits over running a RANS simulation.

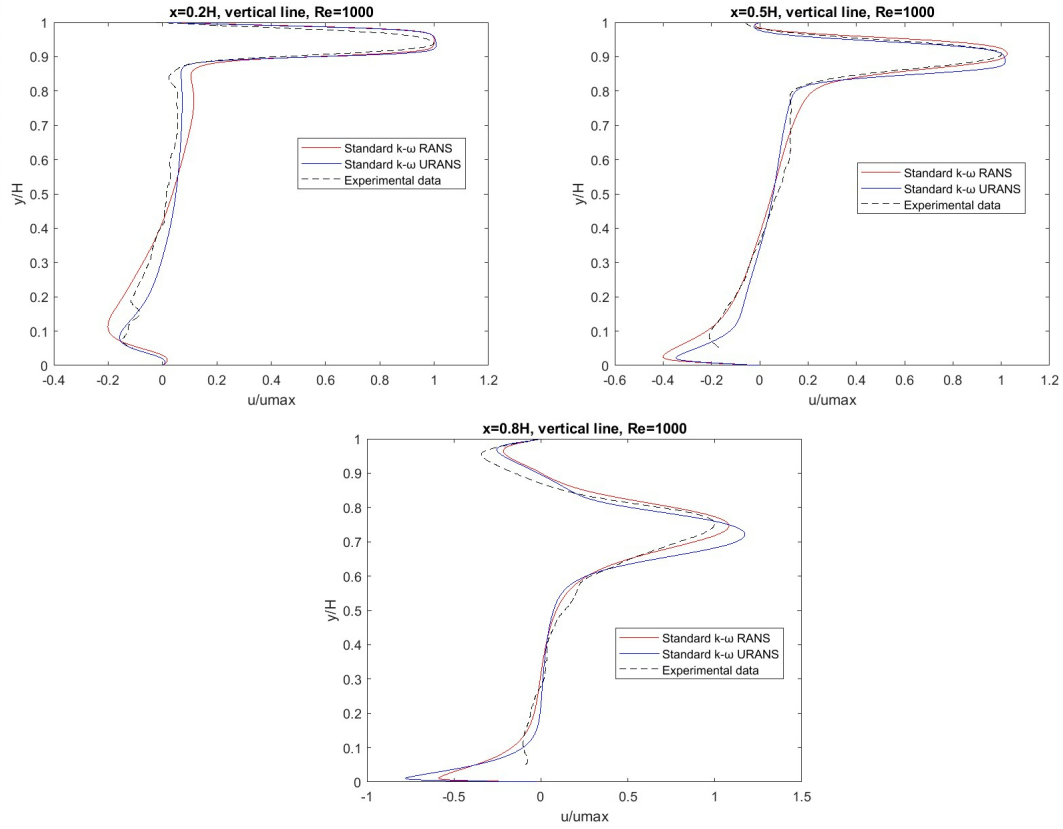

Figure 70: Velocity profiles of RANS and URANS simulation of the optimized standard $k-\omega$ model of the transitional case with a Reynolds number of 1000.

5.2.6 DES

In order to apply the DES approach, the same criteria used for the fully turbulent case were applied to the transitional benchmark mesh. The maximum value for y^+ should be one and the f-value should be above five for most of the cavity. To check these criteria, a RANS simulation was conducted on the transitional case with a Reynolds number of 2500 using the SST $k-\omega$ model with the low-Re corrector enabled which provided the best results for the case with a Reynolds number of 2500. The case with a Reynolds number of 2500 was used to check these criteria rather than the case with a Reynolds number of 1000, as the Re=2500 case produces the highest y^+ values and was the limiting case. The resulting mesh, which satisfied these criteria, had 7 441 000 nodes. You can see this mesh in figure 71 and the corresponding y^+ values in table 21. It is worth noting that the maximum y^+ values remain below 1 except for the left and right walls, although the average y^+ value at these walls is still below 1, which minimizes errors.

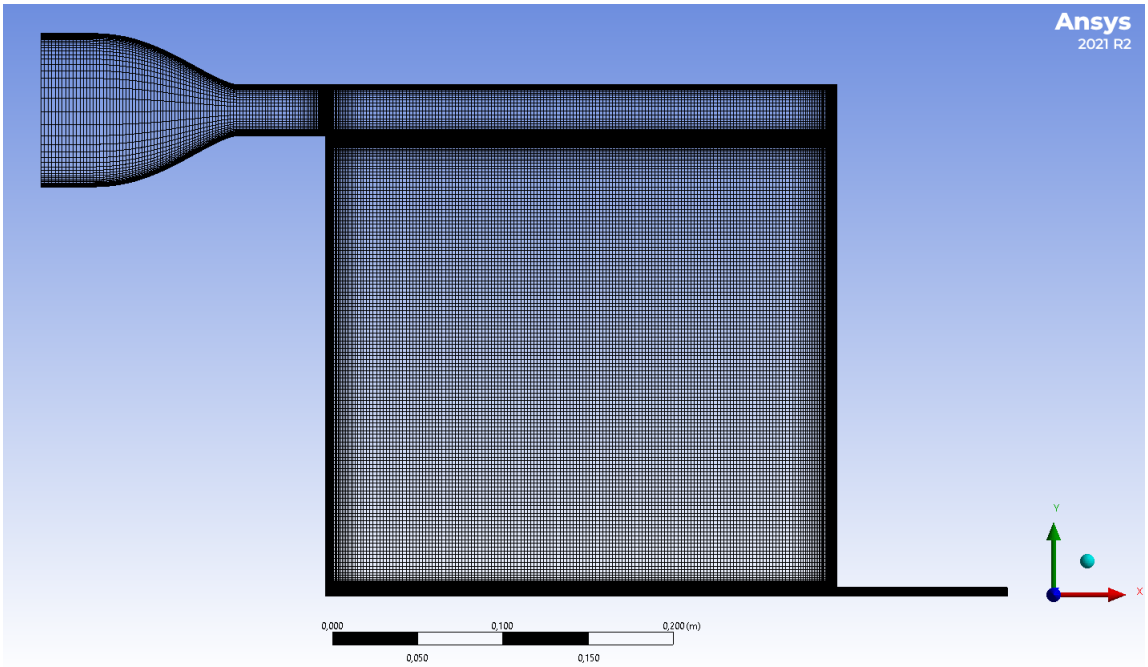

Figure 71: Mesh utilized on DES and LES approaches on the transitional benchmark, which consists of 7 441 000 nodes.

Table 21: The y^+ values for the transitional case with a Reynolds number of 2500 at the various walls for the mesh that is utilized for DES and LES. The SST $k-\omega$ model with the low-Re corrector option enabled is the RANS model used to obtain these values.

	Ceiling	Floor	Inlet wall	Outlet wall	Left/right wall
Max	0.4671	0.5025	0.5763	0.1206	1.849
Average	0.0692	0.1271	0.1797	0.4425	0.0815

Figure 72 shows the contour plot of the f-value at the xy-midplane for the transitional case with a Reynolds number of 2500, from the SST $k-\omega$ model with the low-Re corrector enabled. The plot indicates that the f-value remains mostly above 5, apart from the near-wall, free-shear regions, and upper right and lower left corners. These specific areas require excessive mesh refinement to attain an f-value greater than 5, which leads to more computationally expensive simulations.

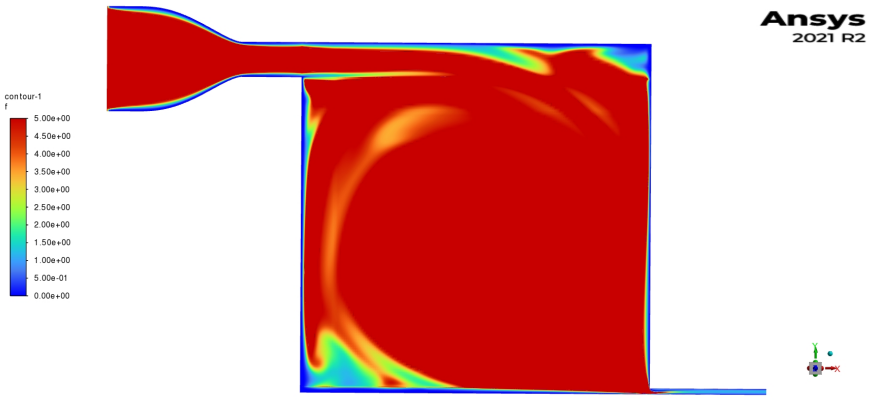

Figure 72: F-value at the xy-midplane of the transitional case with a Reynolds number of 2500 of the mesh used for LES and DES. Values obtained from a SST $k-\omega$ simulation with low-Re corrector enabled.

An averaging sensitivity analysis was carried out on the transitional case to determine the appropriate duration for the averaging procedure. Flow through times of 20 and 50 seconds were used for the Reynolds numbers of 2500 and 1000 respectively, which is consistent with Van Hooff et al. studies [4]. For the averaging sensitivity analysis, the DES SST $k-\omega$ model was utilized with a time step of 0.01 and 0.025 seconds for the cases with a Reynolds number of 2500 and 1000 respectively. The results of the velocity profile from the averaging sensitivity analysis are presented in figure 73. The impact of the averaging time on the velocity profiles is minimal, primarily affecting the regions close to the floor. After six flow-through times, the velocity profiles appear to converge. The same can be observed for the case with a Reynolds number of 1000, as seen in figure 96. Therefore, six flow-through times of averaging are sufficient to obtain independent statistics for the velocity magnitude.

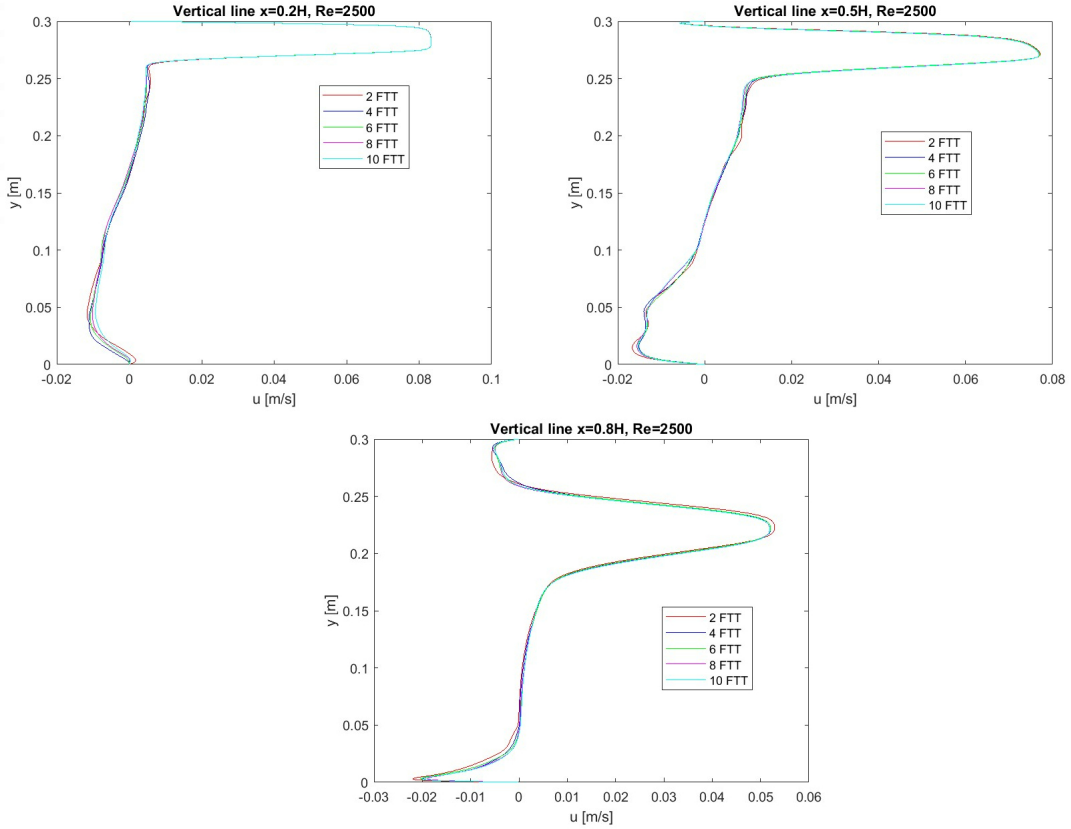

Figure 73: Averaging sensitivity analysis of transitional case with a Reynolds number of 2500. The DES SST $k-\omega$ model is used wit a time step of 0.01 seconds.

A CFL number equal to one resulted in a time step of 0.00008 and 0.00012 seconds for the cases with a Reynolds number of 2500 and 1000 respectively. Since these time steps are many magnitudes smaller compared to the flow-through time, a time sensitivity analysis was conducted. Using the experience from the fully turbulent case, it is possible to increase the time steps with many magnitude higher than the time step required for a CFL number of one. Hence the time steps investigated were, $\Delta t = 0.01$, $\Delta t = 0.005$ and $\Delta t = 0.0025$ seconds for the case with a Reynolds number of 2500. For these simulations the DES SST $k-\omega$ model was utilized, as the SST $k-\omega$ gave good performance compared to the other RANS models. From figure 74, it can be observed that there is little difference between the different time step sizes. Hence a time step of 0.01 seconds is used for the rest of the DES and LES approaches for the case with a Reynolds number of 2500. Comparing the velocity profile with the experimental data, the DES SST $k-\omega$ model predicts detachment too early, implying that the velocity peak is predicted too close to the floor. Furthermore, at the line x=0.5H, the DES model underpredicts the velocity magnitude of the peak.

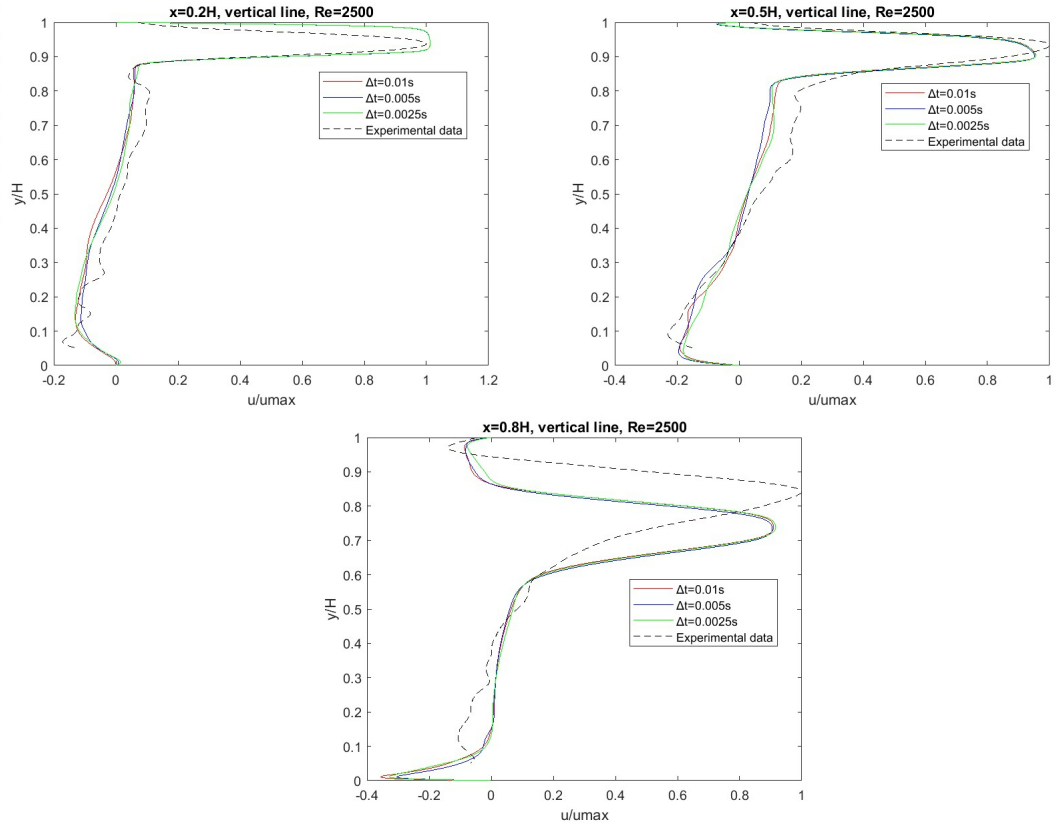

Figure 74: Time sensitivity analysis of the default DES SST $k-\omega$ model on the transitional benchmark with a Reynolds number of 2500.

The following time steps were utilised for a Reynolds number of 1000 on the transitional case: $\Delta t = 0.025$, $\Delta t = 0.01$ and $\Delta t = 0.005$ seconds. Also, for this case, the DES SST $k-\omega$ was utilized. The velocity plots gathered from these time steps are given in figure 75. Through this analysis, it can be concluded that changing the time step has a small effect on the velocity profile. Hence the time step of 0.025 seconds is used for the rest of the DES and LES for this case. Although the detachment happens too early in this case, resulting in a velocity profile lower than the experimental one, the velocity magnitude is predicted correctly.

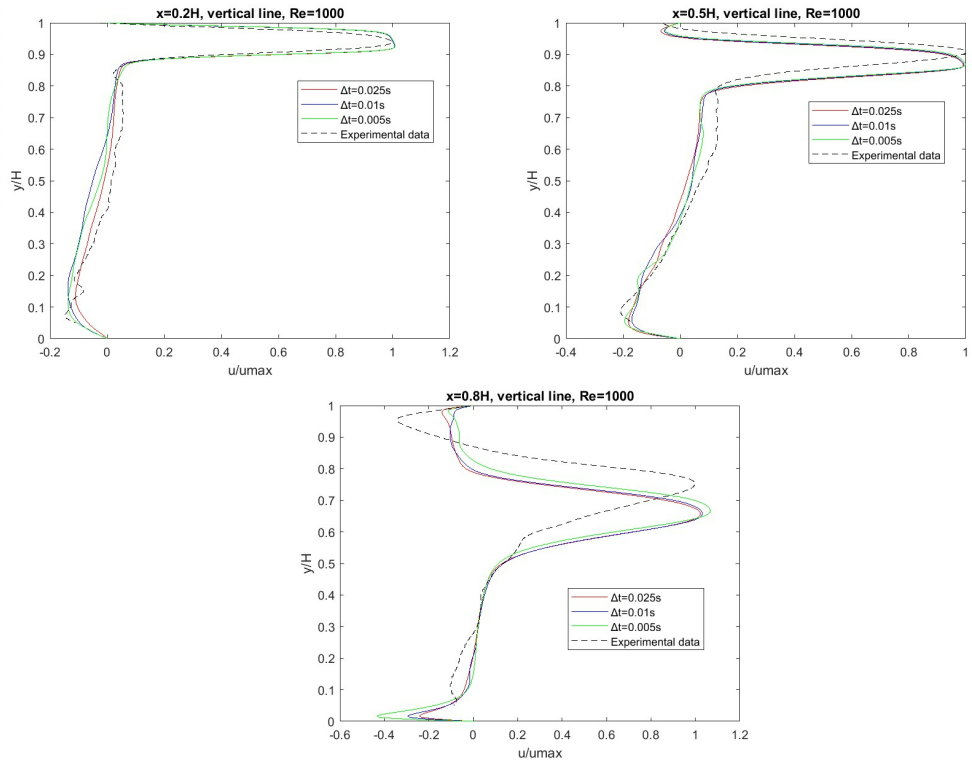

Figure 75: Time sensitivity analysis of the default DES SST $k-\omega$ model on the transitional benchmark with a Reynolds number of 2500.

The transition between RANS and LES in the DES SST $k-\omega$ model depends on the local mesh refinement and the turbulence quantities. The areas where RANS and LES are utilized for the case with a Reynolds number of 2500 are shown through the quantity DES TKE Dissipation Multiplier in figure 76. When the DES TKE Dissipation Multiplier has a value of around one, RANS is utilized; otherwise, LES mode is switched on. As expected, RANS is mostly used close to the walls, while LES is utilized in the far-wall region. Furthermore, RANS is mostly used in the entire inlet duct. The same trend can also be observed for the case with a Reynolds number of 1000. This can lead to grey-zone effects, where the RANS dampen the perturbations that LES would have created. This dampening effect of the turbulent structures in the flow could be a reason why the wall jet predicted by the DES SST $k-\omega$ model detaches too early. Because of this, the DES Spalart-Allmaras model was investigated, where the transition only depends on the local mesh size.

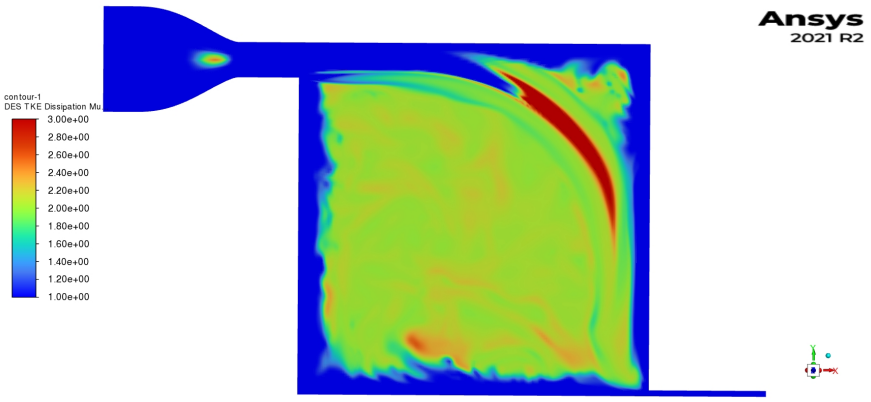

Figure 76: Contour plot showing the DES TKE Multiplier quantity for the xy-midplane of the transitional case with a Reynolds number of 2500. This value determines where RANS and LES are utilized. When this quantity is around 1 RANS is utilized, otherwise LES is utilized.

The DES Spalart-Allmaras model with the vorticity/strain-based production was also investigated for the transitional benchmark. Figure 77 displays the velocity profiles generated by the DES Spalart-Allmaras model and the DES SST $k-\omega$ model. The DES Spalart-Allmaras model detaches earlier than the DES SST $k-\omega$, resulting in poorer performance predicting velocity profiles. This is backed up by table 35, which shows the RMSE values of the models. However, in the case of a Reynolds number of 1000, the DES Spalart-Allmaras model detaches later, as shown in figure 78. This leads to a better prediction of the velocity profile, as confirmed by table 36, which displays the RMSE values of the various models for a Reynolds number of 1000.

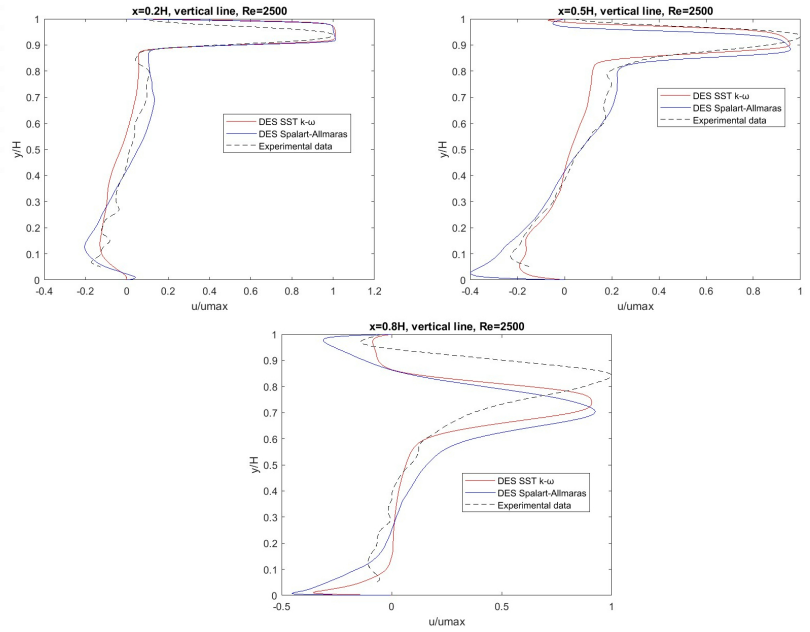

Figure 77: Velocity profiles for different DES models on the transitional benchmark with a Reynolds number of 2500.

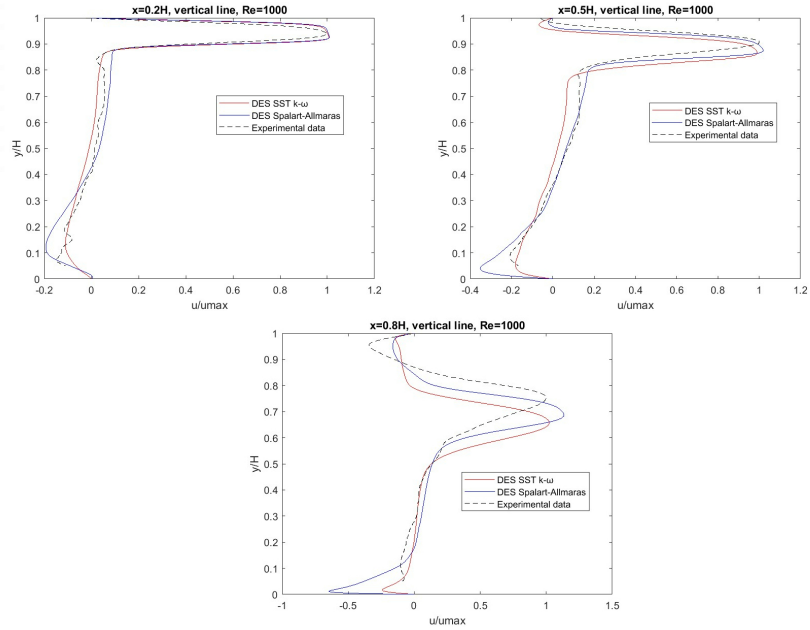

Figure 78: Velocity profiles for different DES models on the transitional benchmark with a Reynolds number of 1000.

As synthetic turbulence inlet conditions had a big effect on the result of the LES and DES on the fully turbulent benchmark, these inlet conditions were also investigated for the transitional case. Here the vortex method, synthetic turbulence generator and spectral synthesizer were investigated at the CFD inlet. Unfortunately, these approaches resulted in the DES diverging for the cases with Reynolds numbers of 1000 and 2500. This is consistent with the fully turbulent case, where high levels of synthetic turbulence at the inlet caused the DES to diverge. Therefore, it appears that DES is prone to divergence when synthetic turbulence at the inlet is excessive, which is a weakness of DES.

5.2.7 LES

Since DES performed poorly in predicting the velocity profiles, LES was utilized on the transitional benchmark. The following LES SGS models were investigated for the transitional benchmark: WMLES and WMLES $S-\Omega$. The velocity profiles obtained using these SGS models for a Reynolds number of 2500 are given in figure 79 along with the velocity profiles from Van Hooff et al. [4]. It is noticeable that both WMLES and WMLES $S-\Omega$ predicted the detachment point too close to the inlet, leading to the max jet velocity being too close to the floor. Additionally, WMLES $S-\Omega$ did not accurately predict the maximum velocity magnitude, but WMLES did a good job of predicting it. The results from Van Hooff et al. gave a much better prediction of the velocity profiles.

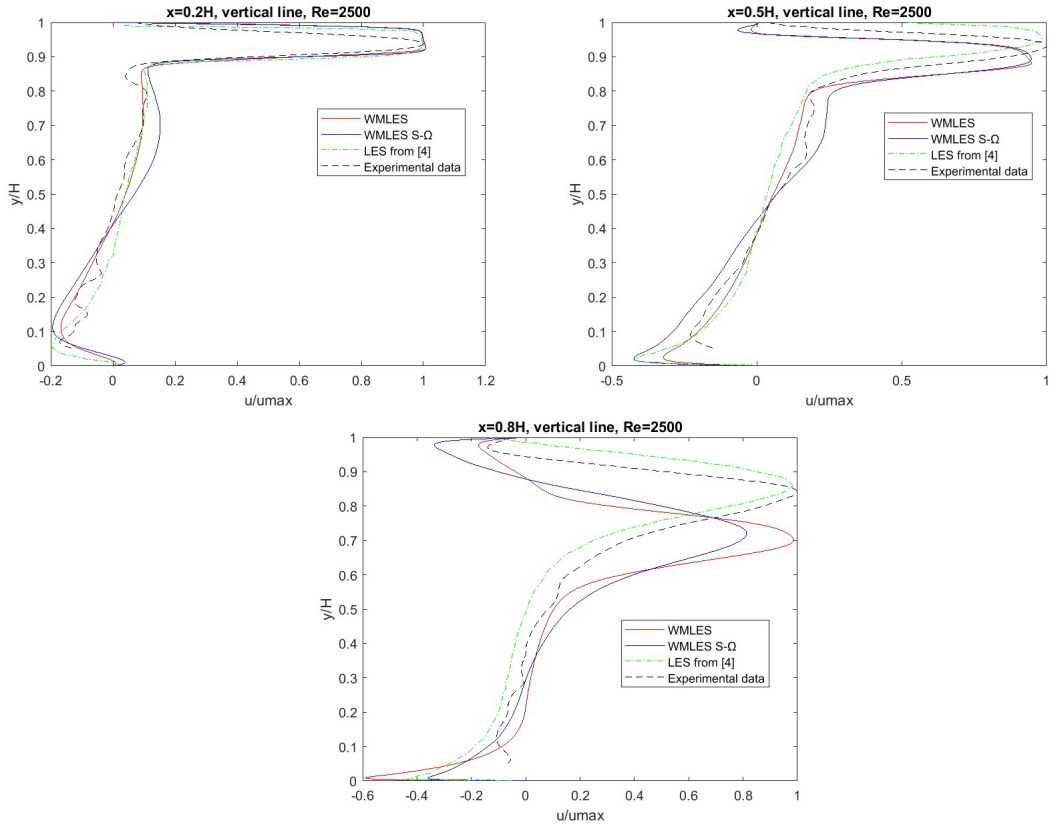

Figure 79: Velocity profiles of different LES SGS models for the transitional case with a Reynolds number of 2500. Compared with the experimental data and the results of Van Hooff et al. [4].

In figure 80, the velocity profile of the LES SGS models for the transitional case with a Reynolds number of 1000 is provided. It is observed that for this case, both WMLES and WMLES $S-\Omega$ predict detachment prematurely. However, the position of the velocity peak is predicted more accurately in this case than in the case with a Reynolds number of 2500. Although the WMLES $S-\Omega$ provides better predictions for the position of the peak, it slightly overestimates the velocity

magnitude at the peak.

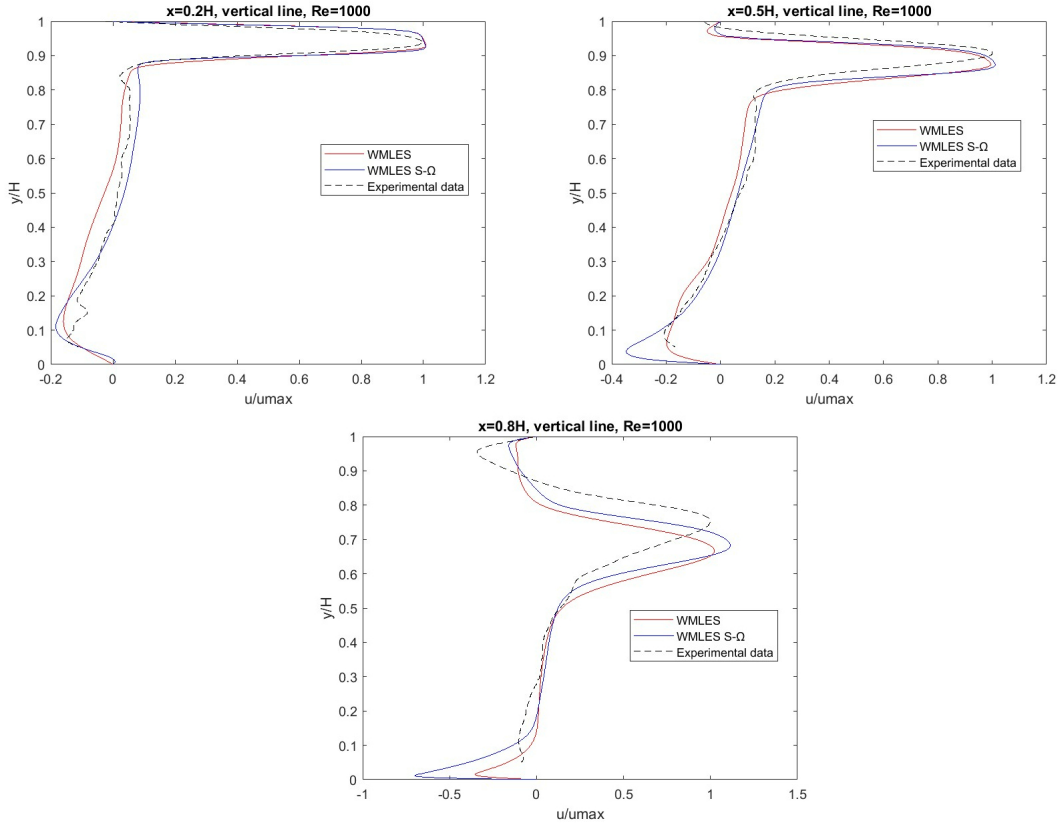

Figure 80: Velocity profiles of different LES SGS models for the transitional case with a Reynolds number of 1000.

To achieve a better prediction of the velocity profiles, different LES approaches were investigated. Firstly the central differencing scheme was employed for the momentum discretization, as the central differencing scheme has a lower numerical diffusion compared to the bounded central differencing scheme, and can therefore represent more of the eddies in the flow [21]. In addition, a synthetic turbulence method was investigated at the inlet, as this was the most important parameter for LES of the fully turbulent case. The vortex method was used at the inlet, with 180 vortices. Finally, the LES setup of Van Hooff et al. [4] was replicated to determine if comparable results could be achieved. The dynamic Smagorinsky-lilly SGS method was utilized for this setup, with the vortex method at the inlet with 180 vortices. The PISO method was used for the velocity-pressure coupling, and the momentum discretization employed the bounded central differencing scheme.

Figure 81 shows the LES approaches described in the paragraph above used on the WMLES SGS model for the transitional case with a Reynolds number of 2500 together with the results obtained by Van Hooff et al. [4]. The results indicate that central differencing yields a similar velocity profile as the default WMLES, without any significant improvements. On the other hand, using synthetic turbulence at the inlet and replicating the setup of Van Hooff et al. LES setup accurately predicts the velocity peak location, but underestimates the velocity magnitude. This suggests that the recreation of Van Hooff et al. setup performs worse and underpredicts the peak magnitude, indicating a possible influence of the mesh on the simulation performance. Notably, both cases that apply a synthetic turbulence method at the inlet demonstrate the best performance, as shown in Table 40, which presents the RMSE values of the different LES approaches for the case with a Reynolds number of 2500.

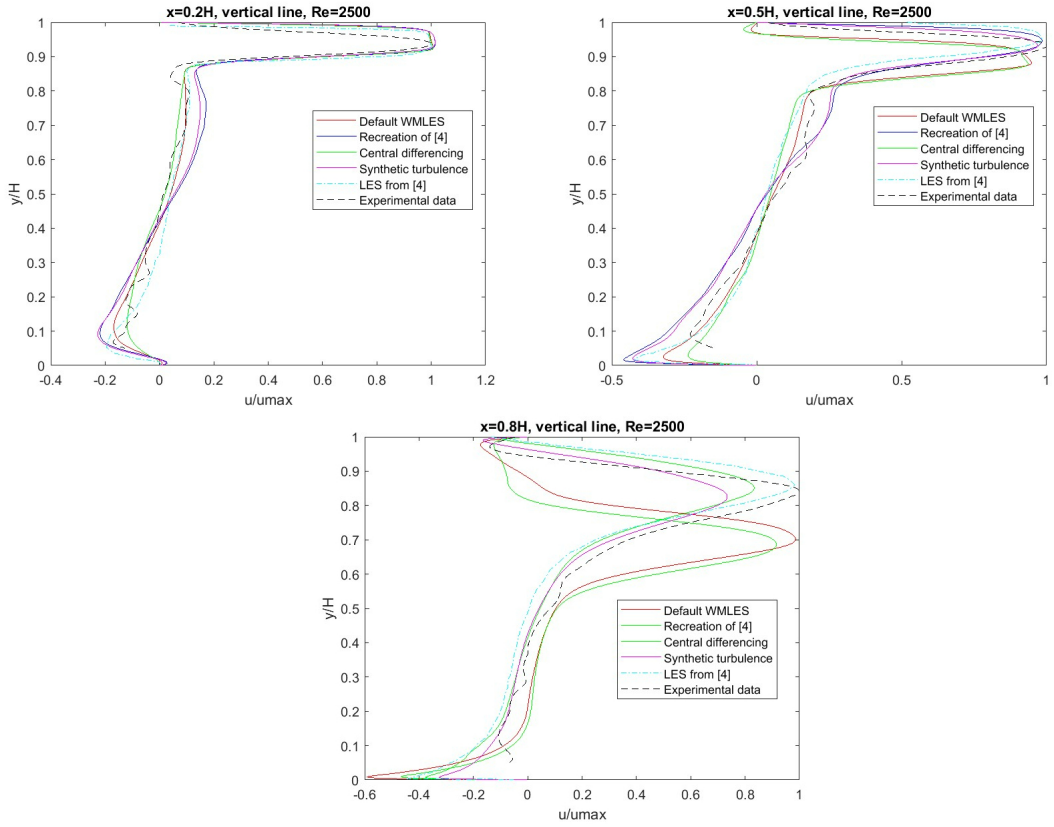

Figure 81: Velocity profiles from various LES approaches on the transitional benchmark with a Reynolds number of 2500. The profiles are compared with experimental data and the results from Van Hooff et al. [4].

Figure 82 shows the turbulent kinetic energy plots achieved from these LES approaches on the transitional case with a Reynolds number of 2500 together with the results from Van Hooff et al. [4]. The findings suggest that the recreation of Van Hooff et al. setup and using synthetic turbulence at the inlet produces excessive levels of turbulent kinetic energy, while central differencing and WMLES underpredict it. This is reasonable, since adding synthetic turbulence at the inlet should increase the turbulent kinetic energy inside the cavity. None of the approaches are able to model the turbulent kinetic energy with good accuracy, but neither was Van Hoof et al. able to achieve this [4]. The profile obtained using the same setup as Van Hooff et al. gives a higher turbulent kinetic energy than the results from Van Hooff et al. [4].

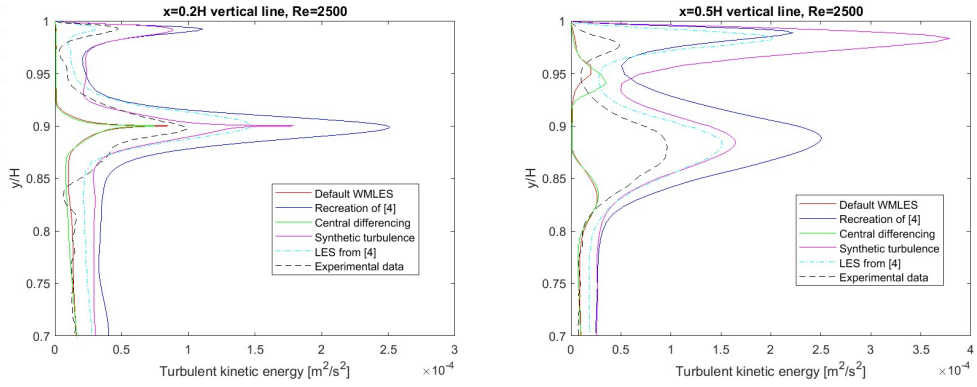

Figure 82: Turbulent kinetic energy profiles from various LES approaches on the transitional benchmark with a Reynolds number of 2500. The profiles are compared with experimental data and the results from Van Hooff et al. [4].

The same LES approaches were investigated on the transitional case with a Reynolds number of 1000 as shown in figure 83. Also, for this case, the approach using central differencing gives similar profiles to the default WMLES. Hence, using this discretization scheme has little impact on the performance of the LES. Furthermore, the synthetic turbulence approach at the inlet produces highly accurate results when compared to experimental data, as evidenced by the RMSE values in table 41. Therefore, it is crucial to have the correct amount of synthetic turbulence at the CFD inlet for optimal LES performance in the transitional case.

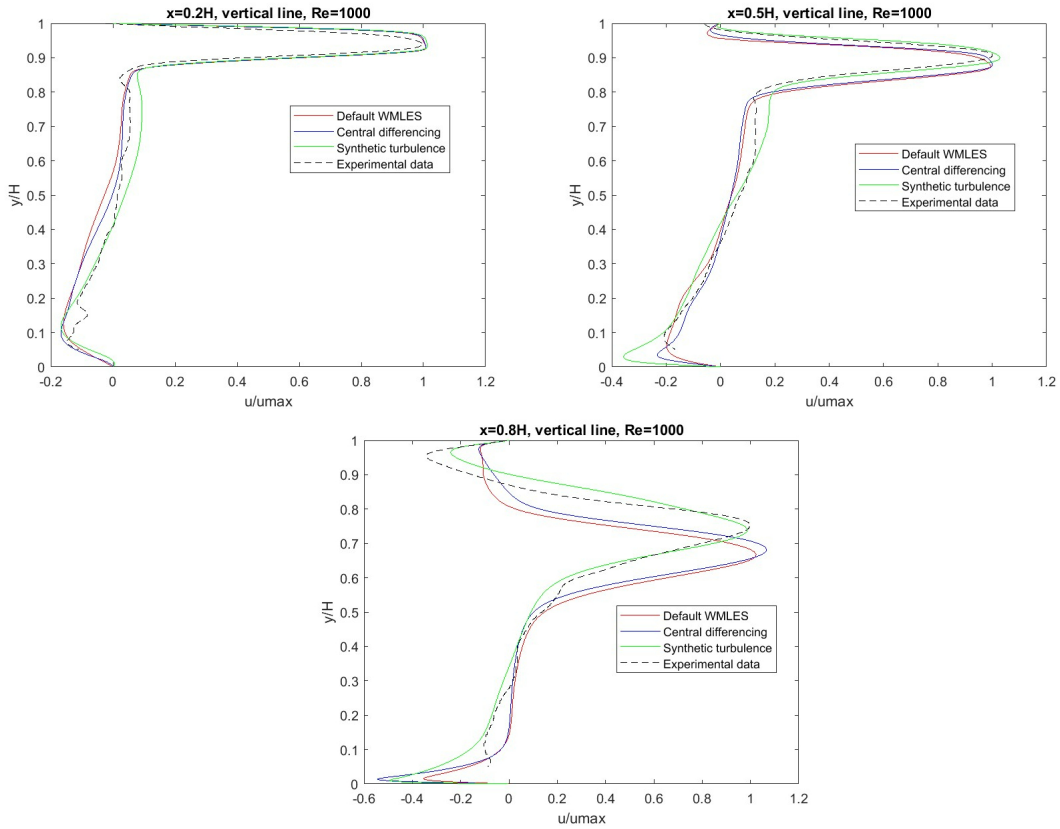

Figure 83: Velocity profiles from various LES approaches on the transitional benchmark with a Reynolds number of 1000.

The turbulent kinetic energy profiles of the different LES approaches of the transitional case with a Reynolds number of 1000 are shown in figure 84. It can be observed that also for the case with a Reynolds number of 1000, using the synthetic turbulence approach at the inlet results in a higher turbulent kinetic energy as expected. Despite the synthetic turbulence method providing accurate velocity profile predictions, it fails to predict turbulent kinetic energy accurately. Consequently, it can be reasoned that accurately predicting the turbulent kinetic energy profiles for the transitional benchmark is a challenging task.

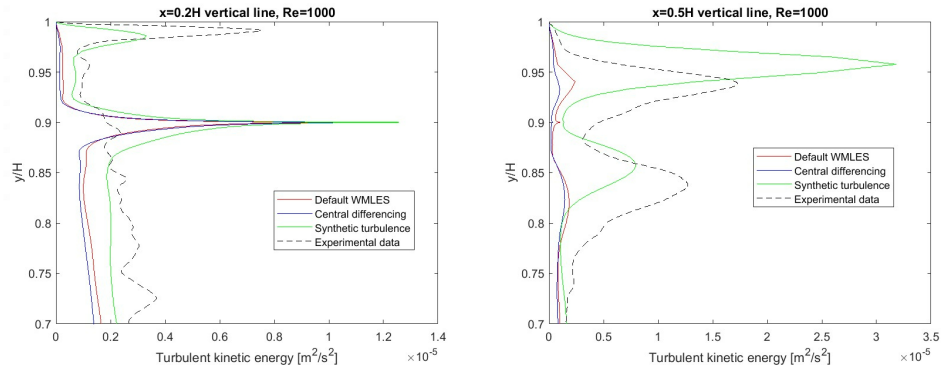

Figure 84: Turbulent kinetic energy profiles from various LES approaches on the transitional benchmark with a Reynolds number of 1000.

As the LES with synthetic turbulence at the inlet gave the best result, a sensitivity analysis was conducted on how the number of vortices at the inlet for the vortex method affected the resulting velocity profiles. For the fully turbulent case, it was concluded that the turbulence intensity defined at the CFD inlet significantly affected the result. Good inlet conditions at the cavity were possible by tuning this turbulence intensity. Figure 85 shows the velocity profiles of such an analysis for the transitional benchmark with a Reynolds number of 2500. For this LES the dynamic Smagorinsky-Lilly SGS model is utilized, and the number of vortices at the inlet investigated was: 180, 300 and 600. It can be observed that the number of vortices used does not have a big effect on the velocity profile. All of the velocity profiles predict the velocity peak at the same location. However, for the LES using 300 vortices, the magnitude of the peak is predicted better. Also, for the turbulent kinetic energy profiles, there is no big difference when adjusting the number of vortices used at the CFD inlet, as shown in figure 97. This suggests that the number of vortices used for the vortex method does not have as big of an impact compared to the turbulence intensity specified at the CFD inlet.

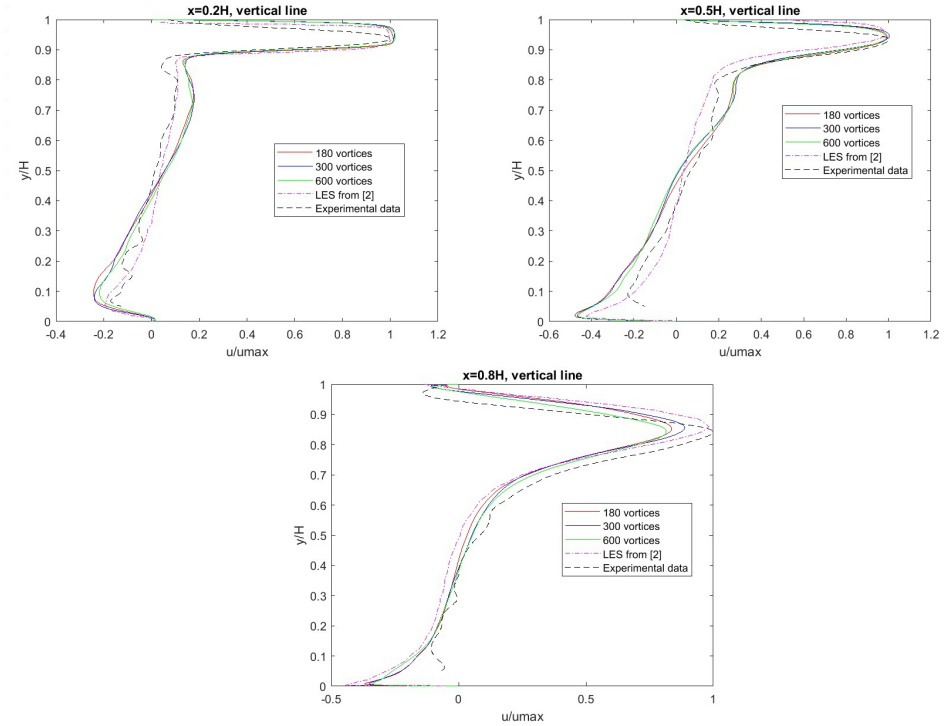

Figure 85: Velocity profiles when adjusting the number of vortices used for the vortex method at the inlet for the dynamic Smagorinsky-Lilly SGS model on the transitional benchmark with a Reynolds number of 2500.

5.2.8 Comparing the turbulence models

In this section, the different optimized turbulence approaches: RANS, DES and LES, will be compared for the transitional case. After analysis, the SST $k-\omega$ model with the low-Re corrector option enabled was found to be the best-performing RANS model for the transitional case with a Reynolds number of 2500. Among the DES approaches, the DES SST $k-\omega$ model gave the overall best performance. The WMLES SGS model with synthetic turbulence at the CFD inlet produced the least error for the LES. The velocity profiles obtained from the optimized RANS, DES, and LES are shown in figure 86. As observed, RANS outperformed the other approaches, as confirmed by the RMSE values in table 22. However, for the LES, the position of the maximum velocity peak was predicted correctly, but the velocity magnitude was underpredicted, which could be due to the turbulence at the CFD inlet being not optimally tuned. The DES approach predicted detachment too early, leading to a velocity peak too close to the floor. It is worth noting that the DES diverged when using synthetic turbulence at the inlet, which was critical for the good performance of the LES.

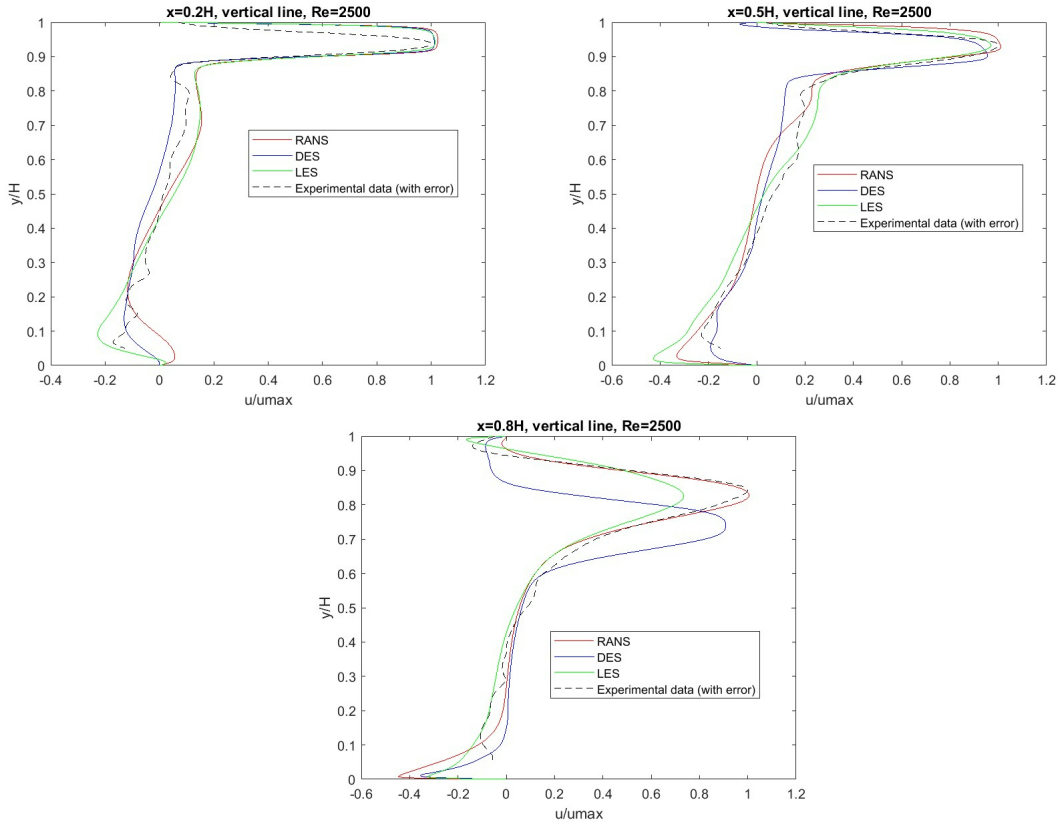

Figure 86: Velocity profiles of the optimized RANS, DES and LES approaches for the transitional benchmark with a Reynolds number of 2500.

Table 22: RMSE values of the optimized RANS, DES and LES approaches for the transitional case with a Reynolds number of 2500.

	Vertical line x=0.2H	Vertical line x=0.5H	vertical line x=0.8H	Average
RANS	0.1240	0.0996	0.0538	0.0925
DES	0.1113	0.0656	0.2869	0.1546
LES	0.1147	0.0704	0.0933	0.0928

Figure 87 illustrates the estimated turbulent kinetic energy for the RANS, DES, and LES approaches for the case with a Reynolds number of 2500. While none of the models was able to

predict the turbulent kinetic energy accurately, they were all able to approximate the general shape of the profile. Of the three models, RANS provided the most accurate prediction, as DES and LES overestimated the turbulent kinetic energy at the peaks. It should be noted that predicting turbulent kinetic energy accurately is a difficult task, as even with the use of LES, Van Hooff et al. [4] were unable to achieve good accuracy in predicting the turbulent kinetic energy for the transitional case with a Reynolds number of 2500 [4].

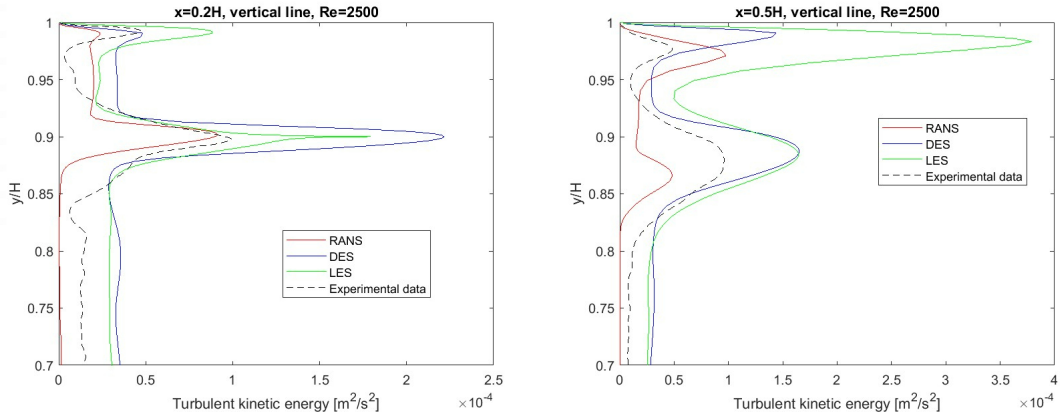

Figure 87: Turbulent kinetic energy profiles of the optimized RANS, DES and LES approaches for the transitional benchmark with a Reynolds number of 2500.

For the transitional case with a Reynolds number of 1000 the velocity profiles from the optimized RANS, DES and LES approaches are given in figure 88. The standard $k-\omega$ model with default options was the best performing RANS model. The Spalart-Allmaras model with vorticity/strain-based production showed the best performance for DES. Meanwhile, the WMLES with synthetic turbulence utilized at the CFD inlet performed best for LES. Upon analysis of figure 88, it can be observed that DES performed the worst while LES and RANS had similar profiles with good coherence with the experimental data. This is confirmed in table 23, which displays the RMSE values of the different turbulence approaches. The reason for DES underperforming was due to divergence when using synthetic turbulence at the inlet, which prevented it from recreating the good inlet conditions that LES could provide.

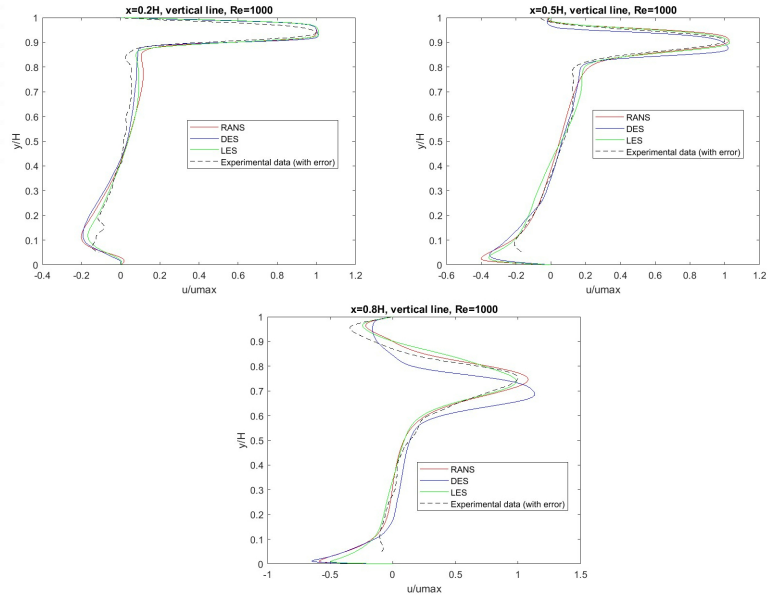

Figure 88: Velocity profiles of the optimized RANS, DES and LES approaches for the transitional benchmark with a Reynolds number of 1000.

Table 23: RMSE values of the optimized RANS, DES and LES approaches for the transitional case with a Reynolds number of 1000.

	Vertical line x=0.2H	Vertical line x=0.5H	vertical line x=0.8H	Average
RANS	0.0667	0.0497	0.0810	0.0658
DES	0.0611	0.0884	0.1934	0.1143
LES	0.0605	0.0477	0.0907	0.0663

In figure 89, one can see the turbulent kinetic energy plots for the RANS, DES, and LES approaches that have been optimized for the case with a Reynolds number of 1000. Unfortunately, these approaches are unable to accurately predict the turbulent kinetic energy profile and perform worse than they did when dealing with a Reynolds number of 2500. Therefore, it is challenging to determine which approach gives the best prediction of the turbulent kinetic energy.

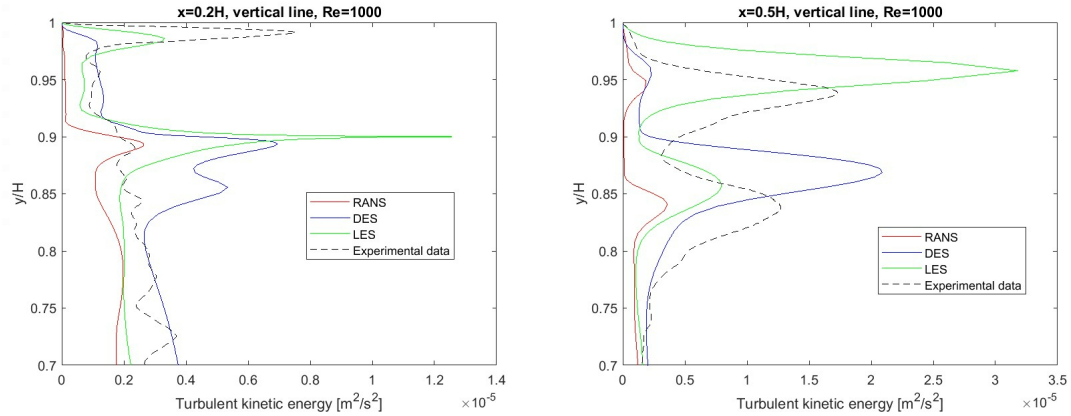

Figure 89: Turbulent kinetic energy profiles of the optimized RANS, DES and LES approaches for the transitional benchmark with a Reynolds number of 1000.

5.3 Comparision of turbulence modelling approaches

This section compares the performance of the different turbulence modelling approaches for the different benchmarks. This is done by looking at the RMSE values for the different turbulence modelling approaches. However, it is important to note that the RMSE values obtained from different benchmarks may not be directly comparable due to scale dependency. Nevertheless, dividing the velocity by the mean inlet bulk velocity means that values are scaled within the same range. Therefore the RMSE from the different benchmarks can give an approximate comparison. This can indicate the effect of the different turbulence modelling approaches, and can help determine which turbulence modelling approaches perform well for modelling a cavity flow.

5.3.1 RANS modelling

The results of the different default RANS models on the given benchmarks are presented in Table 24, showing the average RMSE values. Generally, the default RANS models perform better for the fully turbulent case compared to the transitional case. This is particularly evident for the $k-\epsilon$ models on the transitional case with a Reynolds number of 1000. The default Spalart-Allmaras model and the BSL $k-\omega$ model give good results for all benchmarks.

Table 24: Comparison of the RMSE values of the default RANS models for the benchmarks investigated in this thesis.

	Fully turbulent	Transitional (Re=2500)	Transitional (Re=1000)	Average
BSL $k-\omega$	0.0863	0.1032	0.1243	0.1046
SST $k-\omega$	0.0970	0.1378	0.1579	0.1309
Standard $k-\omega$	0.1069	0.1466	0.0658	0.1064
RNG $k-\epsilon$	0.0904	0.1696	0.2326	0.1642
Realizable $k-\epsilon$	0.0866	0.1702	0.2309	0.1626
Standard $k-\epsilon$	0.0668	0.1680	0.2235	0.1528
Spalart-Allmaras	0.0806	0.1306	0.1187	0.1100

Table 25 shows the average RMSE values of the different wall treatment approaches applied to the $k-\epsilon$ models for RANS. The meshes are adjusted accordingly to meet the y^+ criteria given in table 1. It can be observed that the standard wall function gives the least amount of error, and gives a better performance compared to using enhanced wall treatment. In addition, using the standard wall function leads to needing fewer computational nodes, which means that the simulation gets less computationally expensive. However, the RMSE error obtained using wall functions is larger than that of the $k-\omega$ and Spalart-Allmaras models. Therefore, the standard wall function should only be used when the need to reduce computational expensiveness exceeds the desire for good accuracy when modelling cavity flows.

Table 25: Comparison of the average RMSE values of various wall treatment approaches on the RANS models for the benchmarks investigated in this thesis.

	Fully turbulent	Transitional (Re=2500)	Transitional (Re=1000)	Average
Enhanced wall treatment	0.0809	0.1693	0.2317	0.1606
Standard	0.0769	0.1220	0.2018	0.13336
Scalable	0.0779	0.1958	0.2917	0.1885
Non-equilibrium	0.0908	0.1935	0.2292	0.1712

Several correctors and options from Fluent were tested for the RANS models, but only a few showed improvements in the resulting velocity profiles. One of the only correctors which gave less error was the low-Re corrector. Table 26 displays the average RMSE values of this corrector on the SST $k-\omega$ model, which reveals that the low-Re corrector enhances the velocity profiles for all the investigated benchmarks. However, the low-Re corrector does not improve all benchmarks for the BSL $k-\omega$ and standard $k-\omega$ models, as shown in table 37 and 38, respectively. Therefore, it is recommended to use the low-Re corrector with precaution for the BSL $k-\omega$ model and the standard $k-\omega$ model, while it should be used for the SST $k-\omega$ model.

Table 26: Average RMSE values of the different correctors of the SST $k-\omega$ model on the various benchmark investigated in this thesis.

	Fully turbulent	Transitional (Re=2500)	Transitional (Re=1000)	Average
Regular	0.097	0.1378	0.1579	0.1309
Corner	0.1052	0.1485	0.1213	0.1250
Low-Re	0.0897	0.0925	0.0966	0.0929

The different Fluent options for the Spalart-Allmaras model are shown in table 27. It can be observed that using the vorticity/strain-based production term gives the best results for the transitional case with a Reynolds number of 1000. While using the vorticity-based production term gives the best result for the other cases. Thus, employing the vorticity/strain-based production term is recommended solely for transitional low Reynolds number flows. The RMSE values are given in table 28 for the optimised RANS models using wall treatment approaches and correctors. It can be observed that the SST $k-\omega$ model with the low-Re corrector applied gives the best overall performance. In contrast, the $k-\epsilon$ models with the standard wall function give the most errors.

Table 27: Average RMSE values of the different Fluent options of the Spalart-Allmaras model on the various benchmark investigated in this thesis.

	Fully turbulent	Transitional (Re=2500)	Transitional (Re=1000)	Average
S-A V-P	0.0806	0.1187	0.1306	0.1100
S-A V-S-P	0.0887	0.1556	0.0788	0.1077
S-A V-S-P corner	0.0870	0.1546	0.0900	0.1105
S-A V-P corner	0.0806	0.1328	0.1489	0.1208

Table 28: Average RMSE values of the optimized RANS models using different correctors, wall treatment approaches and other options in Fluent for the various benchmarks investigated in this thesis.

	Fully turbulent	Transitional (Re=2500)	Transitional (Re=1000)	Average
BSL $k-\omega$	0.0863	0.1032	0.1243	0.1046
SST $k-\omega$	0.0897	0.0925	0.0966	0.0929
Standard $k-\omega$	0.1187	0.1205	0.0771	0.1054
RNG $k-\epsilon$	0.0690	0.1027	0.2049	0.1255
Realizable $k-\epsilon$	0.0890	0.1185	0.1961	0.1345
Standard $k-\epsilon$	0.0727	0.1448	0.2044	0.1406
Spalart-Allmaras	0.1187	0.1205	0.0771	0.1054

5.3.2 Comparision of RANS, DES and LES

In this section, the RANS model which performed the best, which was the SST $k-\omega$ model with the low-Re corrector enabled will be compared with the optimized DES and LES approaches. Table 29 presents the RMSE values of the three approaches on the analyzed benchmarks in this thesis. It is evident that LES produces the smallest error, while DES has the largest. Nevertheless, the error between the RANS and LES approaches is rather small. Hence, RANS on the SST $k-\omega$ model with the low-Re corrector applied give relatively good results. However, it is important to note that adjusting the amount of synthetic turbulence at the CFD inlet can optimize the LES of the transitional case with a Reynolds number of 2500 even further. DES gives the biggest error because the simulations diverge when a lot of synthetic turbulence is used at the CFD inlet. This results in the DES being unable to reproduce the same turbulence intensity as a well-tuned LES.

Table 29: Comparing the RMSE values of the optimized turbulence modelling approaches on the various benchmarks investigated in this thesis.

	Fully turbulent	Transitional (Re=1000)	Transitional (Re=2500)	Average
RANS	0.0897	0.0966	0.0925	0.0929
DES	0.0774	0.1143	0.1546	0.1154
LES	0.0882	0.0663	0.0928	0.0824

6 Conclusion

For this thesis, three cavity flow benchmarks were investigated using CFD approaches. Two benchmarks had transitional flow with a Reynolds number of 1000 and 2500, while the third benchmark had fully turbulent flow with a Reynolds number of 5000. Firstly different RANS models and options were investigated on these benchmarks. The default $k-\epsilon$ models gave good results for the fully turbulent case, but gave poorer results for the transitional cases. The default $k-\omega$ and Spalart-Allmaras models performed accurately for both the transitional and fully turbulent cases. Furthermore, different wall treatment approaches were investigated for the $k-\epsilon$ models, and it was found that the standard wall function performed the best. It not only reduced computational cells resulting in less needed computational effort, but also provided better overall performance for cavity flow simulations. Hence, utilising wall functions is recommended when using the $k-\epsilon$ models. Nevertheless, the performance of a $k-\epsilon$ model with the standard wall function was still generally lower than utilizing the $k-\omega$ models or the Spalart-Allmaras model. Other different correctors and Fluent options were also investigated for the different RANS models. The only corrector option giving generally greater performance for all of the benchmarks was the low-Re corrector option for both the SST $k-\omega$ model and the standard $k-\omega$ model. However, for the BSL $k-\omega$ model this option did not generally improve the prediction of the velocity field. Using the strain/vorticity-based production term for the Spalart-Allmaras model only improved performance for the transitional case with a Reynolds number of 1000, but did not give any improvements for the other cases. Hence, this option is only recommended for really low Reynolds number flows. When all of these options are used to optimize the RANS model, it was concluded that the SST $k-\omega$ model with the low-Re corrector option enabled gave the least error compared to the experimental data. The other $k-\omega$ models and the Spalart-Allamaras model also performed well for all benchmarks. URANS simulations of the optimized RANS models did not result in any improvement, so it is not recommended for cavity flow simulations.

Several LES approaches were tested on the benchmarks, and the most significant improvement was achieved by adding synthetic turbulence at the inlet. This synthetic turbulence required some adjustments to ensure the correct amount of turbulence entered the cavity. For the fully turbulent case, a sensitivity analysis was conducted on the turbulence intensity specified at the CFD inlet, and it was concluded that adding 50% turbulence intensity gave good results for the LES. The inlet flow from the inlet duct also produced similar results as a DNS of rectangular channel flow with the similar Reynolds number [5]. This is a significant finding, as in the LES by Taghinia [2] and Zasimova [3], the inlet conditions were created by running an LES of a periodic rectangular channel flow. This means it is possible to recreate the same inlet condition without running a costly LES prior to the cavity flow simulation by adjusting the turbulence intensity at the CFD inlet. For the transitional case with a Reynolds number of 2500, the LES performed relatively well. However, if the synthetic turbulence at the inlet was further optimized better LES results could be obtained. For this case a sensitivity analysis was conducted on the number of vortices used for the vortex method when creating synthetic turbulence at the CFD inlet. The number of vortices used had little effect on the velocity profiles, and had a much smaller effect compared to the turbulence intensity at the CFD inlet. For the case with a Reynolds number of 1000, using synthetic turbulence at the inlet gave excellent results. For the transitional case, none of the modelling approaches was able to predict the turbulent kinetic energy with good accuracy. Different SGS models were also investigated, but they did not have as significant of an impact, as the synthetic turbulence at the CFD inlet. However, further research is needed in this area. When comparing the results obtained by LES with the RANS predictions, the velocity profile provided by LES is more accurate.

The main question to be answered in this thesis was whether DES could produce results as accurate as LES for both the fully turbulent and the transitional regime of cavity flow. However, DES encountered a significant challenge during cavity flow simulations, where the use of synthetic turbulence at the CFD inlet often led to divergence. For the fully turbulent case, using synthetic turbulence of 10% or higher at the CFD inlet resulted in the DES diverging. This meant that it was impossible to recreate the good results of LES with a turbulence intensity of 50% at the CFD inlet with DES. Similarly, the use of synthetic turbulence for DES on the transitional case resulted in the simulations diverging. Consequently, DES could not replicate LES's favourable results in this scenario either. To answer the question, indications show that DES can not produce results

as accurately as LES for cavity flows, due to the DES diverging when adding sufficient synthetic turbulence.

7 Further work

The conclusion of this thesis indicates that DES is not suitable for replicating the accuracy of LES because of the instability problems faced when utilizing excessive synthetic turbulence at the CFD inlet. However, further research needs to be conducted on this issue. It is important to determine the cause of these instability issues. Is it due to poor mesh quality or is the method itself unstable when adding synthetic turbulence at the inlet? Is there a way to create the same amount of turbulence at the cavity inlet without the DES diverging? These questions are worth exploring further. Moreover, it would be interesting to study other DES approaches, like IDDES or other hybrid RANS-LES methods, to see if they face the same challenges as DES. If this is not the case, then it could be possible to reproduce the accuracy of LES by using hybrid RANS-LES approaches. This could then result in the simulations being less computationally expensive while maintaining the same accuracy.

It would be of interest to conduct further investigations on LES approaches, particularly to determine the effect of SGS models on the performance of LES for cavity flows. Multiple LES using different SGS models must be conducted to examine this. For the fully turbulent case, the dynamic Smagorisnky-Lilly SGS model was found to be more effective compared to the WMLES and WMLES $S-\Omega$ for the case with no perturbation at the CFD inlet. However, the dynamic Smagorinsky-Lilly SGS model was not utilized for the transitional case. Hence, it would be interesting to see how the dynamic Smagorinsky-Lilly model performs for the transitional case. Moreover, LES of the different SGS models should be conducted on the benchmarks with synthetic turbulence applied at the CFD inlet, to conclude what effect the SGS models have on the accuracy of the simulation. The turbulence intensity specified at the CFD inlet of the fully turbulent case had a significant impact on the performance. Therefore, it would be interesting to conduct a similar sensitivity analysis of the turbulence intensity specified at the CFD inlet for the transitional case. By doing this, it would also be possible to optimize the LES of the transitional case with a Reynolds number of 2500.

In this thesis, the benchmarks that have been studied only account for non-isothermal conditions, which do not consider the effects of temperature gradients. However, in actual cavity flow, temperature gradients may significantly impact the resulting velocity profile. Therefore, exploring isothermal cases and determining if similar conclusions can be drawn would be worthwhile. Additionally, it would be beneficial to investigate other flow configurations. In this thesis, the benchmarks all involve the flow entering the cavity at the upper left corner and exiting at the lower right corner. For example, it would be interesting to analyze a scenario where the flow impinges the floor by flowing straight down from the ceiling, as this is a practical ventilation case for buildings. Furthermore, in real ventilation applications, multiple inlets and outlets often interact. Hence, it would be of interest to conduct a similar analysis on these cases to verify the results obtained from RANS, DES, and LES. However, experimental data or DNS are necessary to verify these cases properly.

References

[1] V. M. Bjerkeli. 'Computational Fluid Dynamics of airflows inside buildings: a comprehensive review of the cavity flow benchmark'. MA thesis. Trondheim, Norway: Norwegian University of Science and Technology, 2020.

[2] J. Taghinia, Md Rahman and T.K.T. Tse. 'Assessment of zero-equation SGS models for simulating indoor environment'. In: *Heat Mass Transfer* 52 (Feb. 2016), pp. 2781–2794. DOI: DOI10.1007/s00231-016-1776-7.

[3] Marina Zasimova, Nikolay Ivanov and Detelin Markov. 'Numerical modeling of air distribution in a test room with 2D sidewall jet. II. LES-computations for the room with finite width'. In: *St Petersburg State Polytechnical University Journal Physics and Mathematics* 13 (Sept. 2020), pp. 65–79.

[4] T. Van Hooff et al. 'Counter-gradient diffusion in a slot-ventilated enclosure assessed by LES and RANS'. In: *Computers Fluids* 96 (2014).

[5] R.D. Moser, J. Kim and N.N. Mansour. 'Direct numerical simulation of turbulent channel flow up to $Re_\tau = 590$'. In: *Physics of Fluids* 11 (1999).

[6] 'Report to Congress on indoor air quality. Volume 2. Assessment and control of indoor air pollution. Final report'. In: (Aug. 1989). URL: https://www.osti.gov/biblio/6958939.

[7] *Ventilation and Coronavirus (COVID-19)*. URL: https://www.epa.gov/coronavirus/ventilation-and-coronavirus-covid-19 (visited on 17/12/2022).

[8] *Operation Room Laboratory*. URL: https://www.ntnu.edu/ept/laboratories/or-lab (visited on 11/04/2023).

[9] Luis Pérez-Lombard, José Ortiz and Christine Pout. 'A review on buildings energy consumption information'. In: *Energy and Buildings* 40.3 (2008), pp. 394–398. ISSN: 0378-7788. DOI: https://doi.org/10.1016/j.enbuild.2007.03.007. URL: https://www.sciencedirect.com/science/article/pii/S0378778807001016.

[10] Malcolm Orme and Nurul Leksmono. 'Ventilation Modelling data Guide'. In: *AIVC Guide 5* 5 (2002). DOI: https://doi.org/10.1016/j.enbuild.2007.03.007.

[11] Simon Bjuri. *Computational Fluid Dynamics of airflows inside buildings: RANS-LES of the cavity flow benchmark*. Norwegian University of Science, Technology, Faculty of Engineering, Department of Energy and Process Engineering, 2022.

[12] W. Malalasekera H. K. Versteeg. *Introduction to computational fluid dynamics. 2nd ed.* Pearson Educational Limited, 2007.

[13] J. Anderson. *Fundamentals of Aerodynamics, sixth edition*. Mc Graw Hill Education, 2017.

[14] M. V. Dyke. *An Album, of Fluid Motion*. The parabolic press, 1982.

[15] L. Davidson. *Fluid mechanichs, turbulent flow and turbulence modelling*. 2022.

[16] P.V. Nielsen. 'Specification of a Two-Dimensional Test Case'. In: *International Energy Agency, Energy Conservation in Buildings and Community Systems, Annex 20: Air Flow Pattern Within Buildings* 20 (1990).

[17] P.V. Nielsen. 'Flow in air conditioned rooms: Model experiments and numerical solution of the flow equations'. PhD thesis. Aalborg University, 1974.

[18] T. Van Hoof et al. 'PIV measurements of a plane wall jet in a confined space at transitional slot Reynolds numbers'. In: *Experiments in Fluids* 53 (2012), pp. 499–517. DOI: 10.1007/s00348-012-1305-5.

[19] ideal simualtions. *Turbulence Models In CFD*. URL: https://www.idealsimulations.com/resources/turbulence-models-in-cfd/ (visited on 06/12/2022).

[20] Steve Rawlings. *Lecture 10: Einstein Summation Convention*. Accessed: 2022–11-21. URL: https://web.archive.org/web/20170106185911/http://www-astro.physics.ox.ac.uk/~sr/lectures/vectors/lecture10final.pdfc.

[21] ANSYS Fluent. *Ansys Fluent Therory Guide*. Accessed: 2022–12-06. URL: http://www.pmt.usp.br/academic/martoran/notasmodelosgrad/ANSYS%5C%20Fluent%5C%20Theory%5C%20Guide%5C%2015.pdf.

[22] P.R Spalart and S.R. Allmaras. 'A One-Equation Turbulence Model for Aerodynamic Flows'. In: *AIAA Paper* 92-0439 (1992).

[23] R.F. Menter. 'Improved two-equation k-omega turbulence models for aerodynamic flows'. In: *NASA Technical Memorandum* 103975 (1992).

[24] C. Rumsey. *The Menter Baseline Turbulence Model*. URL: https://turbmodels.larc.nasa.gov/bsl.html (visited on 06/12/2022).

[25] F.R. Menter, R. Lechner and A. Matyushenko. *Best Practice: Generalized k-ω Two-Equation Turbulence Model in ANSYS CFD (GEKO)*. Accessed: 2022–12-06. URL: https://fluidcodes.com/wp-content/uploads/2020/06/geko-tp.pdf.

[26] Massimo Germano et al. 'A dynamic subgrid-scale eddy viscosity model'. In: *Physics of Fluids A: Fluid Dynamics* 3.7 (1991), pp. 1760–1765.

[27] R.F. Pope. 'Ten questions concerning the large-eddy simulation of turbulent flows'. In: *New journal of Physics* 6 (2004), p. 35.

[28] M. Shur et al. 'Detached-eddy simulation of an airfoil at high angle of attack'. In: *Engineering Turbulence Modelling and Experiments 4*. Ed. by W. Rodi and D. Laurence. Oxford: Elsevier Science Ltd, 1999, pp. 669–678. ISBN: 978-0-08-043328-8. DOI: https://doi.org/10.1016/B978-008043328-8/50064-3. URL: https://www.sciencedirect.com/science/article/pii/B9780080433288500643.

[29] Florian Menter, M. Kuntz and RB Langtry. 'Ten years of industrial experience with the SST turbulence model'. In: *Heat and Mass Transfer* 4 (Jan. 2003).

[30] T. Avraham. *Understanding The Detached Eddy Simulation From DES to IDDES*. URL: https://cfdisraelblog.wordpress.com/2020/06/23/understanding-the-detached-eddy-simulation-from-des-to-iddes/ (visited on 07/06/2022).

[31] Aleksey Gerasimov. *Quick Guide to Setting Up LES-type Simulations*. Accessed: 2023–04-18.

[32] Joel Guerrero. *A crash introduction to turbulence modeling in OpenFOAM*. Accessed: 2022–11-18.

[33] C. Rumsey. *The Spalart-Allmaras Turbulence Model*. URL: https://turbmodels.larc.nasa.gov/spalart.html (visited on 08/12/2022).

[34] R. Kraichnan. 'Diffusion by a Random Velocity Field'. In: *Physics of Fluids* 11 (1970).

[35] R Smirnov, S. Shi and I. Celik. 'Random Flow Generation Technique for Large Eddy Simulations and Particle-Dynamics Modeling'. In: *Journal of Fluids Engineering* 123 (2001).

[36] Michael L. Shur et al. 'Synthetic Turbulence Generators for RANS-LES Interfaces in Zonal Simulations of Aerodynamic and Aeroacoustic Problems'. In: *Flow Turbulence Combust* 93 (2014).

[37] Aleksey Gerasimov. *Quick Guide to Setting Up LES-type Simulations*. Accessed: 2023–06-05. URL: https://www.tfd.chalmers.se/~lada/comp_turb_model/postscript_files/Quick_Guide_to_Setting_Up_LES_version_1.4_for_Lars.pdf.

[38] Tobias Holzmann. *Mathematics, numerics, derivations and OpenFoam*. 2019.

[39] Hanif Montazeri. 'Direct and Large Eddy Simulations Using the SIMPLE Algorithm'. In: *Numerical Heat Transfer, Part A: Applications* 60.10 (2011), pp. 827–847. DOI: 10.1080/10407782.2011.627799. eprint: https://doi.org/10.1080/10407782.2011.627799. URL: https://doi.org/10.1080/10407782.2011.627799.

[40] S.V. Patankar and D.B. Spalding. 'A Calculation Procedure for Heat, Mass and Momentum Transfer in Three-Dimensional Parabolic Flows'. In: *International Journal of Heat and Mass Transfer* (1972).

[41] J. L. Dréau, P. Heiselberg and P. V. Nielsen. 'Simulation with different turbulence models in an Annex 20 benchmark test using Star-CCM+'. In: *DCE Technical Report* N0.xxx (2013).

[42] L. Rong and P.V. Nielsen. 'Simulation with Different Turbulence Models in an Annex 20 Room Benchmark Test Using Ansys CFX 11.0'. In: *DCE Technical reports* N0.46 (2008).

[43] I. Olmedo and P.V. Nielsen. 'Analysis of the IEA 2D test. 2D, 3D, steady or unsteady airflow?' In: *DCE Technical reports* N0.106 (2010).

[44] J. Taghinia, Md Rahman and Timo Siikonen. 'Simulation of indoor airflow with RAST and SST–SAS models: A comparative study'. In: *Building Simulation* 8 (Jan. 2015), pp. 297–306. DOI: 10.1007/s12273-015-0213-z.

[45] J. Taghinia et al. 'One–equation sub–grid scale model with variable eddy–viscosity coefficient'. In: *Computers Fluids* 107 (Nov. 2014). DOI: 10.1016/j.compfluid.2014.10.014.

[46] T. Van Hooff, B Blocken and G.J.F. van Heijst. *Mixing ventilation flow in an enclosure driven by a transitional wall jet*. URL: https://kbwiki.ercoftac.org/w/index.php/Abstr:UFR_4-20 (visited on 14/12/2022).

[47] Byggteknisk forskrift. *Veiledning om tekniske krav til byggverk*. URL: https://dibk.no/regelverk/byggteknisk-forskrift-tek17 (visited on 08/06/2023).

[48] T.H. Dokka et al. 'Kriterier for passivhus- og lavenergi bygg – Yrkesbygg'. In: *Prosjekt raport* 42 (2009).

[49] *Idun*. URL: https://www.hpc.ntnu.no/idun/.

[50] *Fram*. URL: https://documentation.sigma2.no/hpc_machines/fram.html.

Appendix

A Additional figures

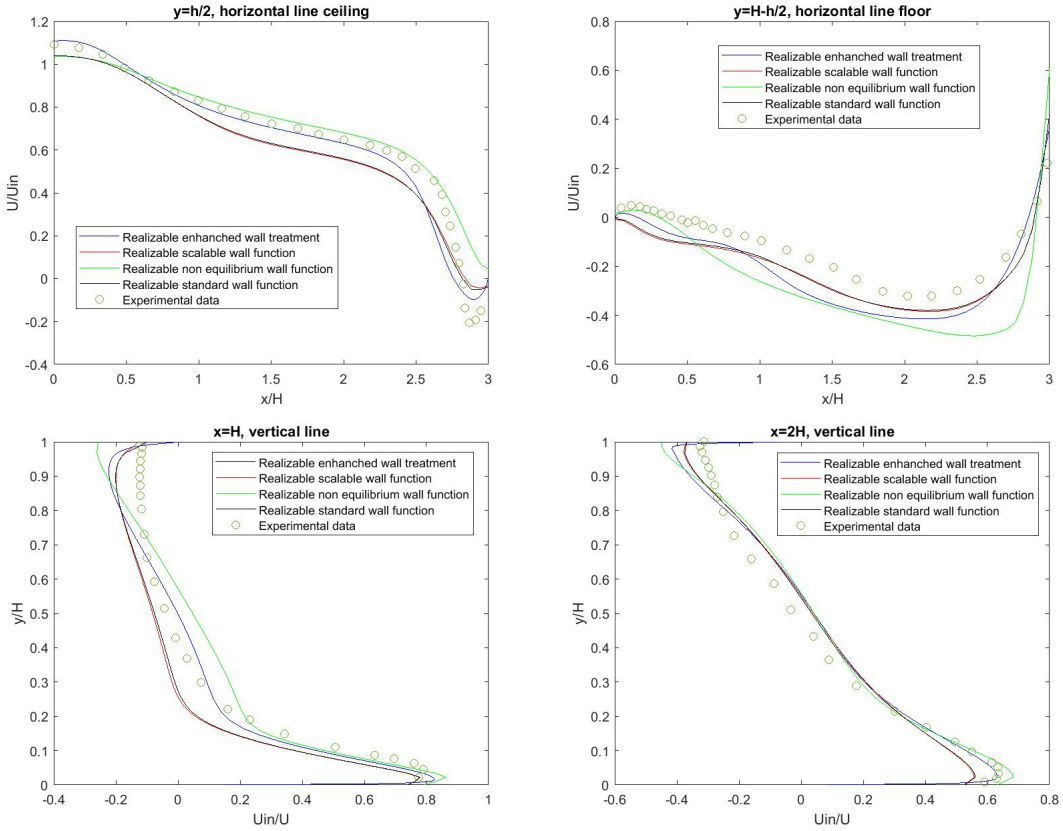

Figure 90: Velocity profiles of different wall treatment approaches when using the realizable $k-\epsilon$ model on the fully turbulent case.

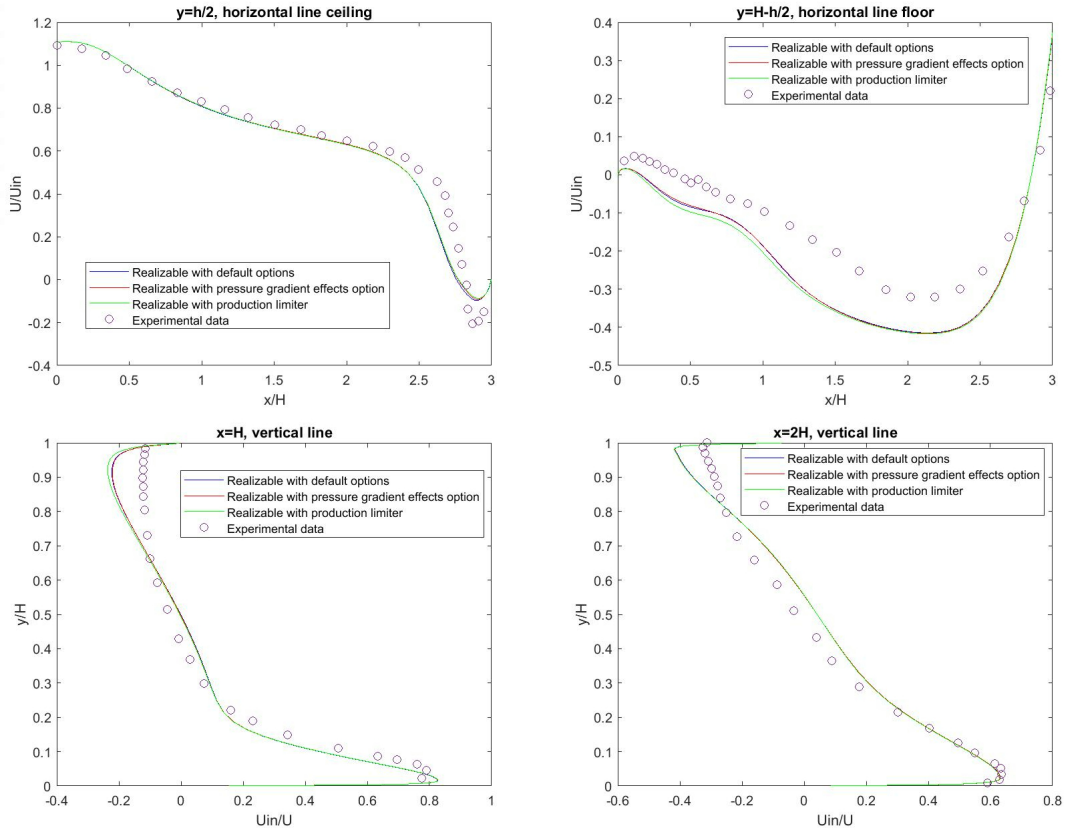

Figure 91: Various corrector options used on the realizable $k-\epsilon$ model on the fully turbulent case.

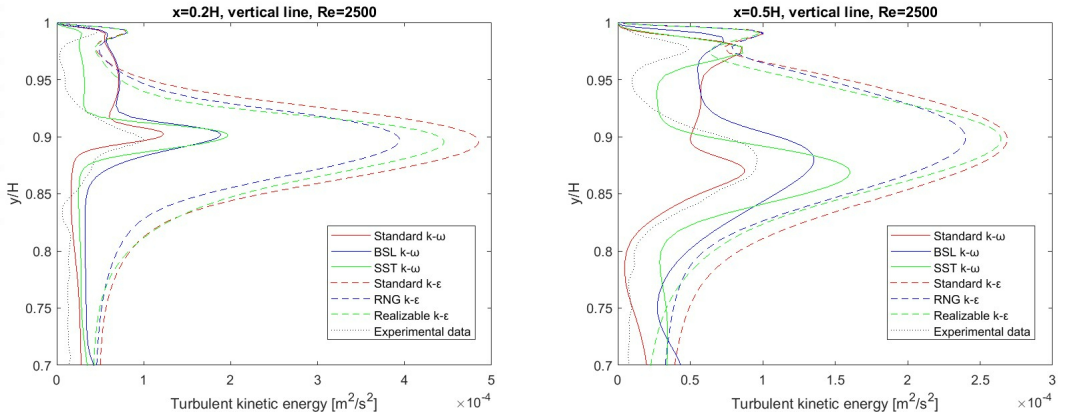

Figure 92: Turbulent kinetic energy plots of the transitional benchmark with a Reynolds number of 2500.

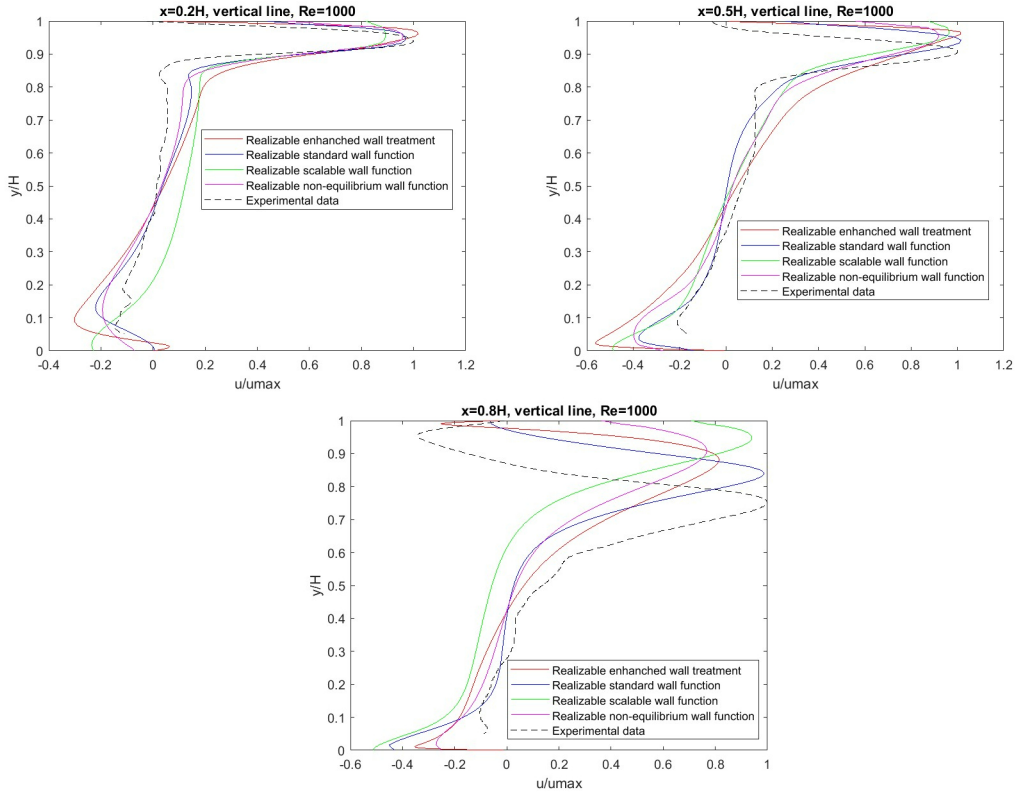

Figure 93: Velocity profiles when using different wall treatment approaches on the Realizable $k-\epsilon$ model, on the transitional case with a Reynolds number of 1000.

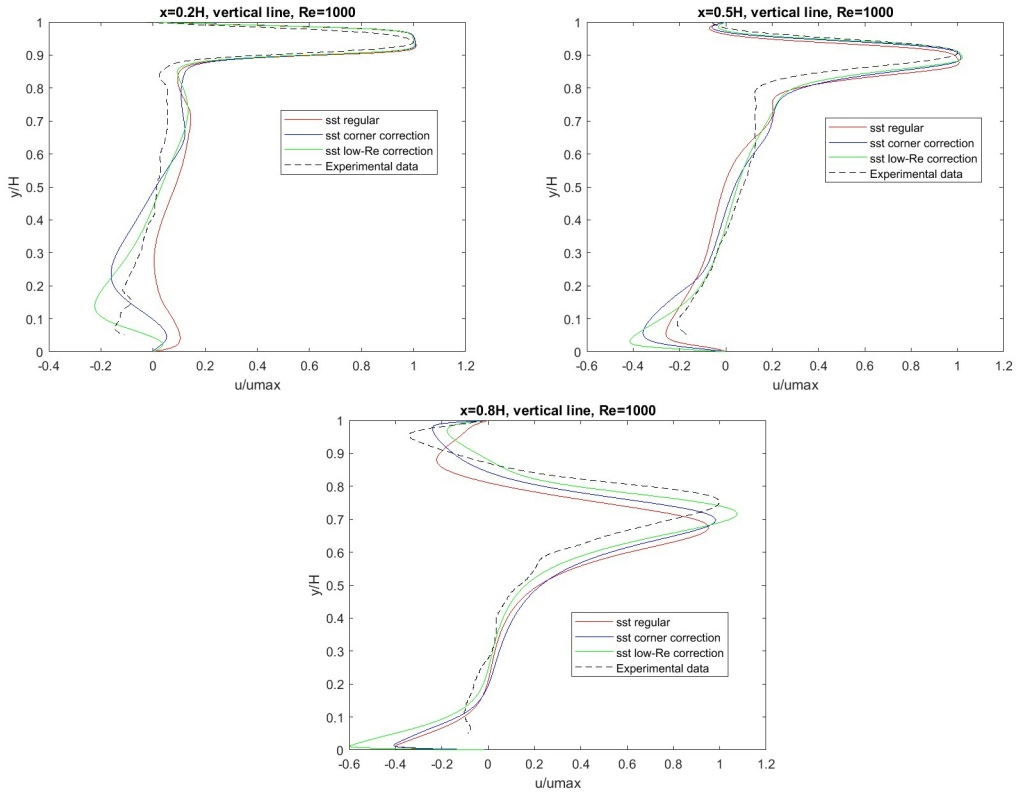

Figure 94: Velocity profile when using different correctors in Fluent of the SST $k-\omega$ model on the transitional case with a Reynolds number of 1000.

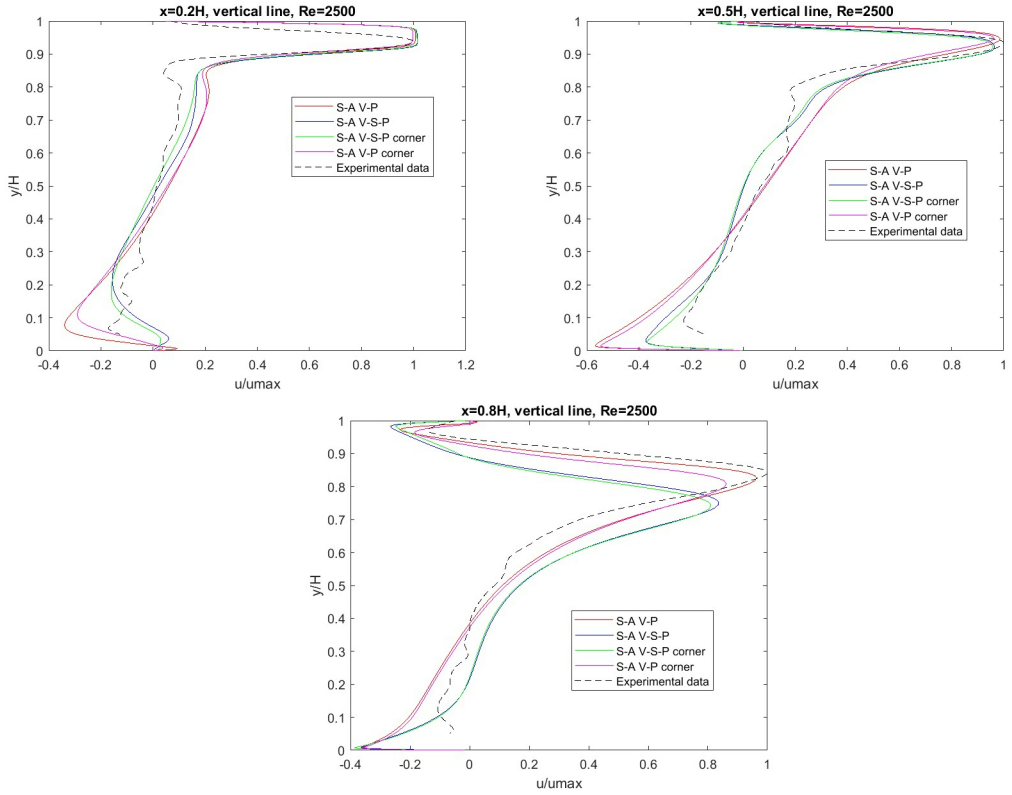

Figure 95: Velocity profile when using different correctors and other options in Fluent of the Spalart-Allmaras model on the transitional case with a Reynolds number of 2500.

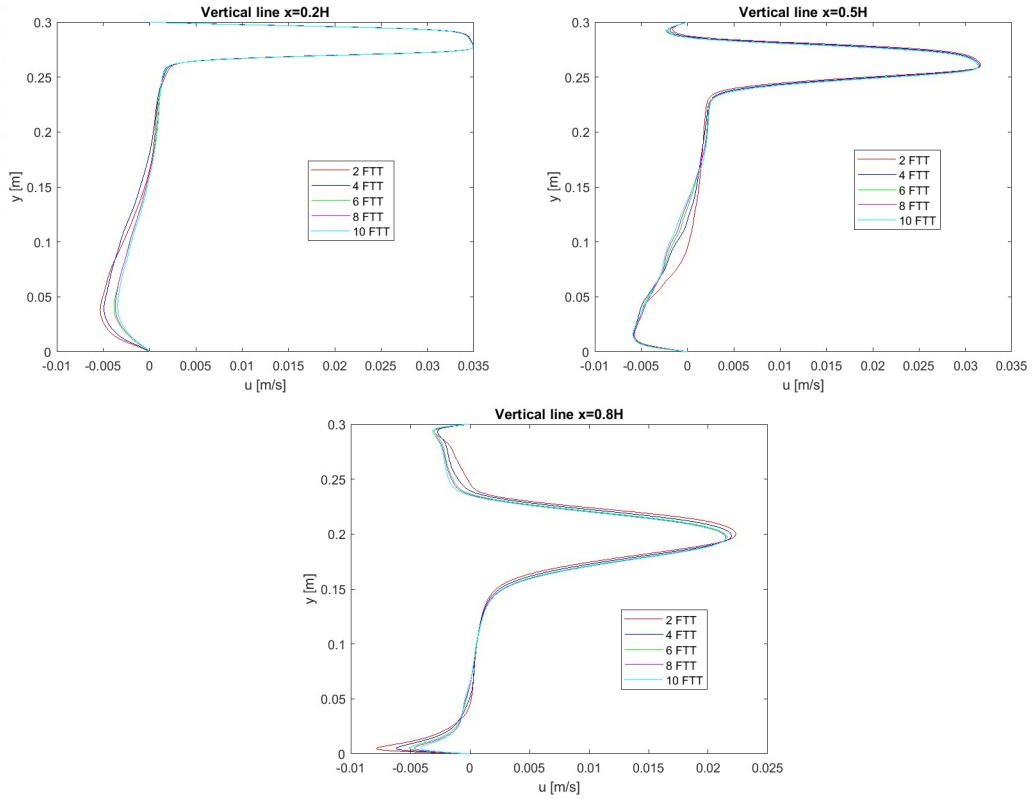

Figure 96: Averaging sensitivity analysis of transitional case with a Reynolds number of 1000. The DES SST $k-\omega$ is utilized with a time step of 0.025 seconds.

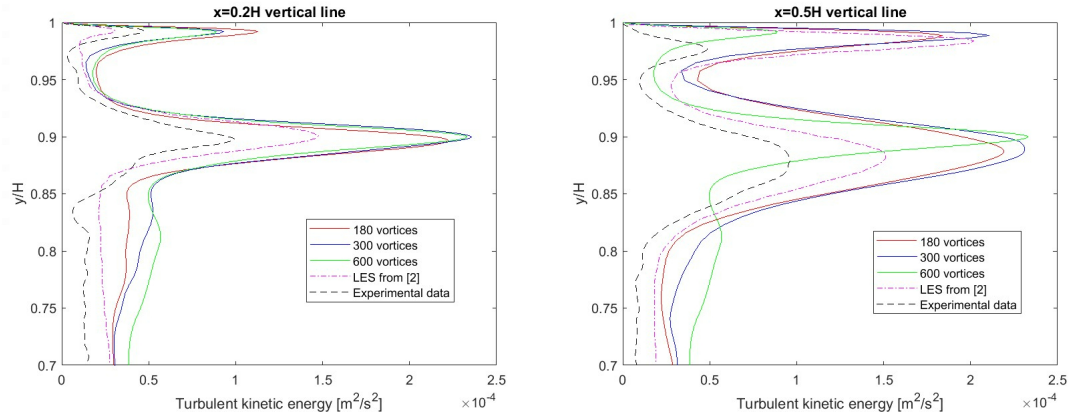

Figure 97: Turbulent kinetic energy profiles when adjusting the number of vortices used for the vortex method at the inlet for the dynamic Smagorinsky model on the transitional benchmark with a Reynolds number of 2500.

B Additional tables showing RMSE values

Table 30: RMSE values when using the RNG $k-\epsilon$ model with different wall treatments of the fully turbulent case.

	Ceil line (y=h/2)	Floor line (y=H-h/2)	Vertical line x=H	Vertical line x=2H	Average
Enhanced wall treatment	0.1117	0.0926	0.0916	0.0658	0.0904
Standard wall function	0.0986	0.0439	0.0951	0.0383	0.0690
Scalable wall function	0.1009	0.0468	0.0970	0.0365	0.0703
Non-equilibrium wall function	0.1313	0.0863	0.0690	0.0703	0.0892

Table 31: RMSE values using different synthetic turbulence approaches for the DES realizable $k-\epsilon$ for the fully turbulent case.

	Horizontal line ceiling (y=h/2)	Horizontal line floor (y=H-h/2)	Vertical line x=H	Vertical line x=2H	Average
DES: NP	0.1320	0.0252	0.1655	0.0698	0.0981
DES: SS	0.1121	0.0235	0.1393	0.0653	0.0851
DES: STG	0.1139	0.0321	0.1263	0.0671	0.0849
DES: VM	0.1043	0.0254	0.1092	0.0707	0.0774

Table 32: RMSE values of velocity for different DES models for the fully turbulent case.

	Horizontal line ceiling (y=h/2)	Horizontal line floor (y=H-h/2)	Vertical line x=H	Vertical line x=2H	Average
DES: k-e	0.1121	0.0235	0.1393	0.0653	0.0851
DES: S-A V-P	0.1787	0.0457	0.1771	0.1294	0.1327
DES: S-A V-S-P	0.1364	0.0583	0.1508	0.0727	0.1046

Table 33: RMSE values of different LES SGS models on the fully turbulent case.

	Horizontal line ceiling (y=h/2)	Horizontal line floor (y=H-h/2)	Vertical line x=H	Vertical line x=2H	Average
WMLES	0.1157	0.0623	0.1413	0.0712	0.0976
WMLES-S-O	0.1767	0.0651	0.0642	0.0984	0.1011
D-S	0.141	0.0583	0.0619	0.0879	0.0873

Table 34: RMSE values of the dynamic Smagorinsky model with double inlet duct length and different turbulence intensities at the CFD inlet for the fully turbulent case.

	Horizontal line ceiling (y=h/2)	Horizontal line floor (y=H-h/2)	Vertical line x=3H	Vertical line x=6H	Average
TI=4%	0.1396	0.0658	0.1622	0.0694	0.1093
TI=10%	0.1196	0.0660	0.0661	0.0924	0.08603
TI=20%	0.1266	0.0712	0.0694	0.0896	0.0892
TI=50%	0.1063	0.0337	0.0508	0.0714	0.0656

Table 35: RMSE values of the different DES models on the transitional benchmark with a Reynolds number of 2500.

	Vertical line x=0.2H	Vertical line x=0.5H	Vertical line x=0.8H	Average
DES SST	0.1113	0.0656	0.2869	0.1546
DES Spalart-Allmaras	0.1089	0.1263	0.3368	0.1907

Table 36: RMSE values of the different DES models on the transitional benchmark with a Reynolds number of 1000.

	Vertical line x=0.2H	Vertical line x=0.5H	Vertical line x=0.8H	Average
DES SST	0.0546	0.1432	0.2868	0.1615
DES Spalart-Allmaras	0.0611	0.0884	0.1934	0.1143

Table 37: RMSE values of the different correctors of the BSL $k-\omega$ model on the various benchmark investigated in this thesis.

	Fully turbulent	Transitional (Re=2500)	Transitional (Re=1000)	Average
Regular	0.0863	0.1032	0.1243	0.1046
Corner	0.1021	0.1000	0.1185	0.1068
Low-Re	0.1004	0.1832	0.1101	0.1312

Table 38: RMSE values of the different correctors of the standard $k-\omega$ model on the various benchmark investigated in this thesis.

	Fully turbulent	Transitional (Re=2500)	Transitional (Re=1000)	Average
Regular	0.1069	0.1466	0.0658	0.1064
Corner	0.1169	0.0790	0.1485	0.1148
Low-Re	0.1187	0.0771	0.1205	0.1054

Table 39: RMSE values of the optimized RANS and URANS of the RNG $k-\epsilon$ model on the transitional case with a Reynolds number of 2500.

	Vertical line x=0.2H	Vertical line x=0.5H	vertical line x=0.8H	Average
RANS: RNG	0.1185	0.1257	0.0643	0.1028
URANS: RNG	0.1179	0.1275	0.0561	0.1005

Table 40: RMSE values from various LES approaches of the transitional benchmark with a Reynolds number of 2500.

	Vertical line x=0.2H	Vertical line x=0.5H	vertical line x=0.8H	Average
WMLES	0.0629	0.1182	0.2566	0.1459
Recreation of [9]	0.1183	0.0954	0.1186	0.1108
Central differencing	0.1000	0.1571	0.3862	0.2144
Synthetic turbulence	0.1147	0.0704	0.0933	0.0928

Table 41: RMSE values from various LES approaches of the transitional benchmark with a Reynolds number of 1000.

	Vertical line x=0.2H	Vertical line x=0.5H	vertical line x=0.8H	Average
WMLES	0.0629	0.1182	0.2566	0.1459
Central differencing	0.0585	0.1019	0.2182	0.1262
Synthetic turbulence	0.0605	0.0477	0.0907	0.0663

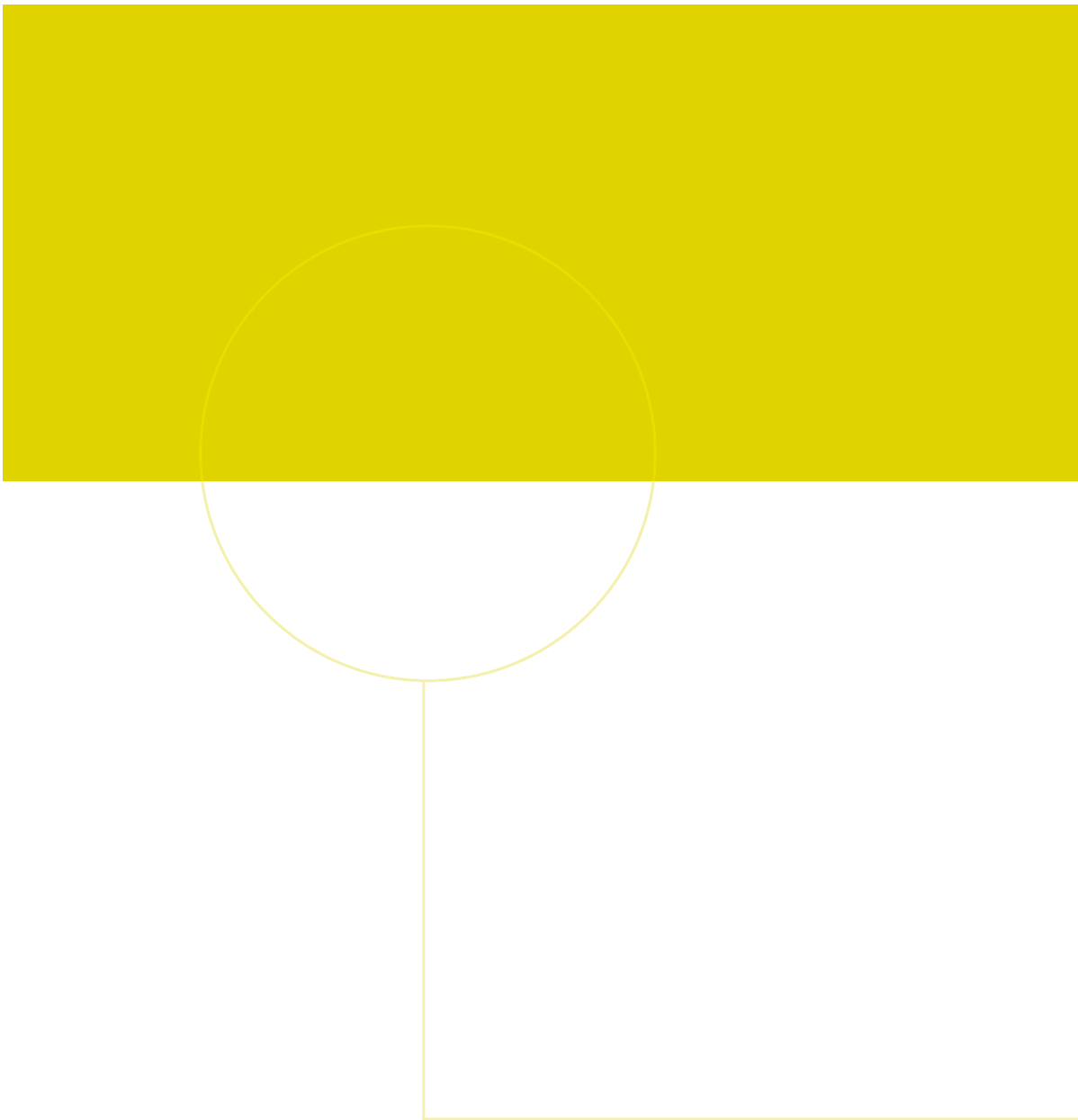

NTNU

Norwegian University of
Science and Technology